2006

CONTROLLED EVAPORATION DRIVEN SYNTHESIS AND APPLICATIONS OF ORDERED NANOPOROUS CERAMIC FILMS

Venkat Rao Koganti
University of Kentucky, venkat_rao357@yahoo.com

ABSTRACT OF DISSERTATION

Venkat Rao Koganti

The Graduate School
University of Kentucky
2006

CONTROLLED EVAPORATION DRIVEN SYNTHESIS AND APPLICATIONS OF
ORDERED NANOPOROUS CERAMIC FILMS

ABSTRACT OF DISSERTATION

A dissertation submitted in partial fulfillment of the
requirements for the degree of Doctor of Philosophy in the
College of Engineering at the University of Kentucky

By Venkat Rao Koganti
Director: Dr. Stephen E. Rankin, Professor of Chemical Engineering

Lexington, Kentucky
2006

ABSTRACT OF DISSERTATION

This dissertation addresses the synthesis of oriented mesoporous ceramic films by evaporation induced self-assembly of surfactants and ceramic precursors in films dip coated from ethanol-rich sols. First, the kinetics of silica polycondensation in surfactant templated sol-gel films is studied both before and after deposition using infrared spectroscopy. These observations reveal an induction time (with minimal condensation rate) before curing begins in certain surfactant-templated silica films, which can be utilized to perform post-synthesis modification. This induction time is maximized at high humidity, and by long nonionic surfactant headgroups (rather than, for instance, a trimethylammonium headgroup). The second part of the dissertation addresses lattice Monte Carlo (MC) simulation of the effects of confinement on the 2D hexagonally close packed (HCP) phase formed by 60 vol% surfactant in a polar solvent. The effects of size and type of confining geometry (slit, cylindrical and spherical cavities) and of surface chemistry are simulated. The HCP mesophase orients orthogonal to chemically neutral surfaces which attract both head and tail of the surfactant equally. Novel mesophase geometries are simulated including radially oriented micelles, concentric helices, and concentric porous shells. Utilizing fundamental insights from the kinetics and MC studies, the third part of the dissertation describes the synthesis of silica films with orthogonally tilted HCP mesophase on chemically neutral surfaces. Crosslinking a random copolymer of polyethylene oxide (PEO)-polyproplyene oxide (PPO) on glass slides results in chemically neutral surfaces for the PEO-PPO-PEO triblock copolymer template (P123) used here. The orthogonal orientation of the HCP channels is confirmed using advanced x-ray scattering techniques and electron microscopy. The final part of the dissertation discusses applications of ceramic films with orthogonally tilted (ortho-) HCP mesophase. Silica membranes with ortho-HCP pores are prepared on porous alumina supports, and show permeability of ethanol orders of magnitude greater than films with parallel-oriented HCP channels. Size-selective filtration of gold nanoparticles confirms the absence of any nanoscale cracks in the membranes. For a second application, we prepare titania films with ortho-HCP mesopores. Careful crystallization of the films followed by spinning on an organic hole conducting polymer (P3HT) leads to active bulk heterojunction solar cells.

Key words: Mesoporous, Orthogonal, HCP, Kinetics, Simulations

Venkat Rao Koganti

10/25/2006

CONTROLLED EVAPORATION DRIVEN SYNTHESIS AND APPLICATIONS OF
ORDERED NANOPOROUS CERAMIC FILMS

By

Venkat Rao Koganti

Dr. Stephen E. Rankin

Director of Dissertation

Dr. Barbara L. Knutson

Director of Graduate Studies

Date 10/25/2006

RULES FOR THE USE OF DISSERTATIONS

Unpublished dissertations submitted for the Doctor's degree and deposited in the University of Kentucky Library are as a rule open for inspection, but are to be used only with due regard to the rights of the authors. Bibliographical references may be noted, but quotations or summaries of parts may be published only with the permission of the author, and with the usual scholarly acknowledgments.

Extensive copying or publication of the dissertation in whole or in part also requires the consent of the Dean of the Graduate School of the University of Kentucky.

A library that borrows this dissertation for use by its patrons is expected to secure the signature of each user.

Name   Date

DISSERTATION

Venkat Rao Koganti

CONTROLLED EVAPORATION DRIVEN SYNTHESIS AND APPLICATIONS OF
ORDERED NANOPOROUS CERAMIC FILMS

DISSERTATION

A dissertation submitted in partial fulfillment of the
requirements for the degree of Doctor of Philosophy in the
College of Engineering at the University of Kentucky

By Venkat Rao Koganti
Director: Dr. Stephen E. Rankin, Professor of Chemical Engineering

Lexington, Kentucky
2006

Acknowledgements

Dr. Stephen Rankin, is the one of the very few inspiring people that I have come across till now. He always had the patience to listen to me and guide me whenever I approached him. I have definitely enjoyed the liberty that I had working under him during these years. This has helped me a lot to develop my analytical capabilities, which I think is the primary out put of a PhD degree. He has definitely influenced me a lot in deciding a problem solving approach. Above all he is very nice person to work with.

I would like to thank National Science Foundation, Department of Energy and University of Kentucky's Chemical and Materials Engineering Department for providing me financial assistance during this period. I would also like Alan Dozier, Larry Rice and Mary Gail Engle of the Electron Microscopy Facility for their valuable time to make me proficient in using the facilities by myself. With them it would not have been possible for me gather the data that appears in this dissertation in this amount of time. I would like thank Henry Francis and Jason Backus of Kentucky Geological Survey for making their X-Ray Diffraction instrument available to me which has always been the starting point for characterizing my materials.

A special thanks to Dr. Barbara Knutson for her valuable suggestions. She is a wonderful person to collaborate with. Dr. Hans-Joachim Lehmler's suggestions through out this period when ever needed are very much appreciated. My committee members, Dr. Bruce Hinds, Dr. Arthur Cammers, and Dr. Steve Holmes have been very helpful to me in completing this dissertation. A special thanks to Bing Tan who helped me a lot to start my research and was also helpful through out his stay in our lab. Rong Xing is a wonderful colleague and his suggestions with the use of Fourier Transformed Infrared Spectroscopy are very much helpful. I would also like to thank my fellow lab mates for the wonderful time we had working on our experiments together. Collaboration with April Anderson for two summer sessions has been informative and enjoyable.

I would like to thank my parents Koteswara Rao Koganti and Varalakshmi Koganti, my brother Sivaramakrishna Koganti for their support not only during this period of my PhD study but through my entire life till today. They are always there for support and advice. I sincerely dedicate this dissertation to them. I would like to thank my friends who made my stay in Lexington a memorable one. Those Friday evening parties, badminton games, long conversations/arguments we had can never be forgotten. I loved the time I spent with Ellen at church, her family and at the places we visited. In short this work would not have possible without the support of many individuals who have helped me in different ways to grow up as an individual, a student and as a researcher. Thank You All.

TABLE OF CONTENTS

List of Tables

List of Figures

List of Files

Chapter 1 Overview of Surfactant Templated Mesoporous Thin Films: Evaporation Induced Self Assembly (EISA)

Porous materials have been an attractive and important area of research for several years because of their applications in a variety of fields including separations, adsorbents, sensors, catalysis, electronic materials, etc. Based on their pore dimensions, porous materials are broadly classified into three categories: macroporous materials with pore sizes greater than 50 nm, mesoporous materials with pore sizes ranging between 2 nm and 50 nm, and microporous materials with pore sizes less than 2 nm. Zeolites are commonly used porous materials because their crystalline structure gives a very narrow, well defined pore size distribution. However, the pore sizes of zeolites are in the microporous range and hence they are not appropriate materials to process large molecules.[1] The search for synthesis methods for materials with similarly well-defined mesopores passed a major milestone in 1992 when researchers at Mobil Research Corporation discovered the surfactant templation mechanism to synthesize mesoporous materials with tunable pore sizes between 2 nm and 100 nm.[2, 3] They used surfactants to template the pores of the materials by condensing dissolved inorganic precursors in the presence of surfactant micelles (or, it was hypothesized, lyotropic liquid crystals). Calcination of the surfactant after condensation of the inorganic network was found to create pores whose size, shape and morphology are almost exact replicas of the surfactant mesophases present before calcination. Simple processing, tunable pores sizes, and ease of obtaining functional pores have made surfactant templation a major area of research since its initial discovery.

Although mesoporous materials have been synthesized as particles by many researchers,[4, 5] random orientation of pores in particles limits their applications to those that do not rely on precisely controlled orientation, such as adsorption, catalysis, drug delivery and so on. Pore orientation control in ordered mesoporous thin films makes them ideal candidates for a variety of applications like membranes separations, masks for nano-architectures, substrates for growing nano wires, rods, semiconductor applications, etc. Surfactant templated mesoporous thin films were first synthesized by Ogawa[6] and Lu et. al.[7, 8] individually around the same time by a process called Evaporation Induced Self Assembly (EISA). In this process, the evaporation of volatile solvents drives the self assembly of surfactant molecules, resulting in mesostructured thin films. Ordered structures develop within seconds to minutes after the film deposition rather than the timescale of days typical of particle synthesis methods. In addition, the confined geometry of films provides opportunities for manipulating the structure and orientation of the mesophase prior to solidification. Because of these advantages we sought to synthesize surfactant templated mesoporous thin films using the EISA process in this present work. After allowing sufficient

1

time for condensation of inorganic precursors, the surfactant template can be removed by calcination or solvent extraction.[9] Similar to powder products, we can achieve desired pore morphology by varying several synthesis parameters like surfactant to inorganic precursor ratio, temperature, coating environment, etc.

As explained above, different pore morphologies can be achieved depending on the mesophase present prior to surfactant removal. Several one, two and three dimensional pore structures have been synthesized in both mesoporous films and particles.[7, 8, 10-12] Among these pore morphologies, the 2-D Hexagonally Close Packed (HCP) mesophase is of special interest because of several reasons. Its pore structure (hexagonal packing of cylindrical pores) is ideal for modeling the processes occurring in these pores for direct testing of hypotheses about transport in porous films, unlike 3-D interconnected pores. Also, HCP pores in films do not offer alternate paths for the diffusion and mixing of species, unlike their 3-D counterparts. In spite of these advantages for HCP pore morphology, cylindrical channels orient themselves parallel to the substrate when deposited onto both hydrophilic[7] or hydrophobic[13] surfaces. In order to utilize this pore morphology for separations, photovoltaics, sensing, and nanomaterials templating, accessibility of cylindrical pores is a "must have". Thus, forming ceramic films with orthogonally oriented nanoscale pore arrays has been an ongoing quest in the surfactant templating community since EISA was introduced. The main objective of this dissertation is develop a simple substrate modification approach to fulfill this quest. We will conclusively demonstrate the existence of oriented cylindrical channels on chemically neutral surfaces both by extensive characterization of the films and by utilizing these films for applications in the areas of membrane separations and semiconductors. The objective of this chapter is to introduce the area of research by reviewing the current literature. This will include a review of surfactant templated films, followed by a detailed description of various characterization techniques that are heavily used in this work.

1.1. Porous thin films

Sol-gel thin films and monoliths are two morphologies of sol-gel based materials that find interesting applications in a variety of fields. Although monolithic gels prepared via the sol-gel route are potentially of interest because of the complex shapes that these gels can take, they also face a major technical challenge: obtaining crack free gels with reproducible shrinkage.[14] Thin films on the other hand are easy to synthesize, can be coated on any kind of surface and are microscopically crack-free. These advantages make thin films more attractive and useful for applications where only a small amount of porous material is required.

The sol-gel technique of synthesizing thin oxide films by hydrolysis and condensation of alkoxide precursors is of technological and scientific importance because of advantages including low synthesis cost and low operational temperatures compared to other evaporation-based techniques. As mentioned earlier, the blending of surfactant chemistry with the sol-gel technique by scientists at Mobil Research Corporation has revolutionized the sol-gel technique of obtaining metal oxide materials.[2, 3] A few years later Lu et. al. discovered the EISA process of obtaining surfactant templated sol-gel thin films, thus opening the gates to this new area of research.[7]

Several mechanisms were proposed for the formation of MCM 41, one of the original ordered mesoporous aluminosilica powders synthesized by Kresge, Beck and coworkers. [2, 3] MCM-41 is a powder synthesized under alkaline conditions and has hexagonally close packed cylindrical channels. The original hypothesis was that pre-existing liquid crystal nuclei in solution served as templates for the silicates.[3] A lack of evidence for the nuclei led to the more widely accepted idea that co-assembly of silicates with surfactants drives the formation of the ordered composite mesostructure.[15, 16] For synthesizing mesoporous films, we work in acidic conditions to delay the condensation of inorganic precursors in the solution phase.[17] In this dissertation, the precursors used are tetraethoxysilane (TEOS) and tetraethylorthotitaniate (TiOEt) for silica and titania, respectively. The reactions mechanisms discussed below are for silica precursors. Mechanisms of formation of other mesoporous oxides like titania using surfactant templation are similar, although variable coordination number and oxidation state complicate the reaction pathways. The following reaction scheme shows the hydrolysis and condensation reactions of a single reactive functional alkoxide group starting from TEOS and yielding silica.

$$\equiv Si\text{-}OC_2H_5 + H_2O \rightleftharpoons \equiv Si\text{-}OH + C_2H_5OH$$

$$\equiv Si(OH) + \equiv Si(OH) \rightleftharpoons \equiv Si\text{—}O\text{—}Si\equiv + H_2O$$
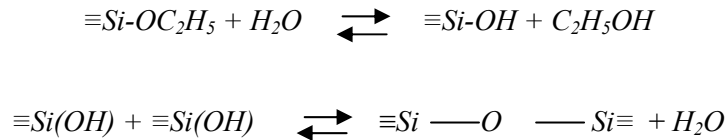
Typical coating sols contain prehydrolyzed inorganic precursors, and the pH is adjusted so that it is at the isoelectric point of the oxide, where the condensation reaction is slowest. For silica the isoelectric pH is 2. In acidic conditions, a portion of the hydrolyzed TEOS is protonated and is present as $SiOH_2^+$, denoted as I^+. When the surfactant is cationic (S^+), like cetyltrimethylammonium (CTA^+), the interaction between the precursor and the surfactant is mediated by the counter ion (such as Br^-) present in the system (indicated by $S^+ X^- I^+$).[18] If the surfactant used is anionic (S^-) like sodium dodecyl sulfate (SDS) the interaction between the precursor and the surfactant is a direct interaction, $S^- I^+$ without a mediating counter ion. Non-

ionic surfactants do not have any charged head groups, so the interaction between the surfactant and silica occurs through hydrogen bonding.[19] Similar interactions between inorganics and surfactants exist in titania precursors also. Many studies have concentrated on the formation mechanisms of the mesoporous materials. These formation mechanisms include charge matching cooperative assembly,[2, 3, 18, 20, 21] neutral templating mechanism by hydrogen bonding[19, 22, 23] and ligand assisted assembly where covalent bonds are formed between inorganic species and surfactants.[24, 25]

There have been several detailed studies in the area of surfactant templated thin films - not only in the area of synthesizing and characterizing materials with various pore geometries, but also in the area of developing applications for these films. Several studies have focused on obtaining films with different pore geometries. Presently, the counterparts of many of the known lyotropic liquid crystalline mesophases have been synthesized in mesoporous inorganic films.[7-9] Several in situ studies of the thin film formation have helped us to understand the structural evolution in surfactant templated thin films. Brinker et. al.[26-28] and Babonneau et. al[29-35] are the two major contributing groups towards these in situ studies. Using in situ Grazing Incidence X-Ray Scattering (GISAXS) technique to obtain information about the kind of mesophase present in the system, the size of the unit cell making up the structure, and the orientation of the phase; and interferometry to measure thickness profiles, Brinker and coworkers have established composition and structure relationships to understand the EISA process. In acidic systems (conditions for EISA process) where silica oligomers are weakly charged resulting in weak electrostatic interactions (as opposed to basic conditions where we have anionic silicate species), self assembly is mainly governed by interfacial (evaporation happening at the interface) and kinetic effects (rate of evaporation of volatile components).[28] Using FTIR spectra of the coated films they also have investigated the interactions between the surfactant and silicates.[28] Using Monte Carlo simulations they highlight the subtle effects of solvent on surfactant aggregates.[26] Also by controlling the ethanol/H_2O evaporation rates, they obtained thicker films with different mesophases.[27] This study highlights the importance of the solvent evaporation on the final outcome of the EISA process.[27]

Babonneau and coworkers have also contributed important fundamental understanding of the EISA process through their in situ studies on the surfactant templated thin film evolution process. Grosso et. al. have examined the influence of condensation rate of silica network on the orientational order of the cylindrical channels in the silica films.[29] Using in situ Small Angle X-Ray Scattering (SAXS), they have observed evidence for cylindrical channel domains being aligned parallel to the interfaces (air/film and film/substrate). The alignment proceeds towards the center and the propagation of this alignment is dictated by the condensation rate of silica,

which depends on parameters like the dilution of the sol, substrate withdrawal rate and so on.[29] This powerful in situ SAXS technique was used by the same group to understand the effect of several parameters including the humidity of the curing environment, pH of the coating sol, ethanol vapor pressure in the system, etc. The results demonstrate that water content in the film (directly related to the humidity of the environment) is a critical parameter in determining the final mesophase obtained (poorly organized, 2-D hexagonal or 3-D cubic mesophases).[30] Also the effects of parameters like pH of the sol and ethanol vapor pressure were explored using in situ x-ray scattering experiments.[33] Phase transformations during cubic mesostructured silica formation (showing lamellar and hexagonal intermediated structures) have also been understood using in situ time resolved SAXS.[34] By combining in situ SAXS and interferometry measurements, Grosso et. al proposed a model for film formation which included different stages in structural evolution.[31] They observed formation of micelles and liquid crystalline mesophases during the final stages of drying. Organization at the mesoscale takes place in the final stages of liquid evaporaration. This entire process depends on the condensation degree of inorganic intermediates.[31] Although titania precursors have different chemical reactivity compared to silica precursors, titania films also undergo similar stages during the mesostructure formation.[35] Despite the differences in chemistry of titania and silica films, mesostructure in these films is governed by similar factors like evaporation of solvents, self assembly of the surfactants and the hydrolysis and condensation of the inorganic precursors.[35] Effects of micelle swelling agents like benzene (which preferentially enter the micelle cores) on the mesophase formation have also been studied using in situ SAXS experiments.[32] Tiemann et. al have observed a decrease in the micelle curvatures upon increasing the benzene concentration, which drives a transformation from cylindrical micelles to lamellar mesophase.[32] Other groups have also used these in situ techniques to understand different aspects of the film formation. Brennan et. al have used in situ grazing incidence x-ray diffraction and x-ray reflectivity to study the structure of surfactant templated silica films grown at air/water interface. They have also observed alignment of the cylindrical domains parallel to the air/film interface and randomly oriented domains deeper into the film.[36]

All of the above studies have mainly focused on characterizing the EISA process only at the mesoscale (which here is defined as the length scale associated with the ordered micelle arrays). The main objective has been to understand the time scales involved in mesostructural ordering (which are typically in the order of a few seconds during and after the film deposition), effects of various parameters on the mesostructure, the sequence of events during phase transformations, etc. The other most important part of the EISA process is the structural evolution of the inorganic framework. The conditions used in EISA are different from traditional sol-gel

chemistry in terms of the pH of the sol, and also the presence of surfactants which alter the hydrolysis and condensation of the inorganics. A better tool to characterize the microstructural changes during the EISA process is FTIR. There are some studies in the literature aimed at comprehending the silica structure evolution in surfactant templated thin films.[37, 38] Two articles from Innocenzi et. al. explain the utility of FTIR for in situ monitoring of the structure evolution during the thin film formation. They aim at understanding the various order-disorder transitions occurring during the thermal annealing of the silica films.[37] In a more recent study Innocenzi and coworkers identify the presence of various stages during the thin film formation using time resolved FTIR spectroscopy.[38] These in situ studies of the EISA process primarily have dealt with time scales that are in the order of seconds after film coating. To our knowledge there are no reported studies trying to characterize the EISA process over longer time periods (minutes to hours after film coating). This is one of the objectives of this dissertation. In chapter 2 we present IR studies on silica films in which we characterize the microstructural changes in the silica network for hours after the film deposition, during which the film environment can be changed to modulate the film mesophase structure.

   Just as many research groups have focused on various aspects of forming surfactant templated films, there are also many prior efforts to control the orientation of HCP mesophase to achieve accessible cylindrical channels in films. One of the many advantages of the HCP phase is its simple structure. Modeling processes happening in cylindrical pores is easier than modeling the processes happening in 3-D interconnected pores. Also, cylindrical pores provide straight paths for convection and diffusion of species, thus increasing the transport efficiencies. HCP channels aligned normal to a film are also potentially useful for nanolithography, for templating of nanoparticles or nanowires arrays, or as components of nanoscale electronic and optical materials. These advantages cause HCP channels to hold a special place in applications like membrane separations, sensors, semiconductrs, etc. – as long as the pores channels are accessible. The majority of the efforts to obtain accessible pore channels in surfactant templated thin films have either focused on creating 3-D interconnected mesophases,[39, 40] or on growing the cylindrical channels in the pore channels of inorganic matrices like anodized alumina with larger pores. The former (forming 3-D interconnected pores) is an important approach when alternate paths for diffusing species are desirable (for instance, in gas phase separations where alternate paths reduce pore blocking). The latter approach aims to align the pores parallel to the alumina walls and thus perpendicular to the substrate surface.[41, 42] This still necessitates forming or using an anodized alumina matrix, and often the resulting pores are not completely accessible.[43] Also, formation of other orientations such as concentric rings, helices, and concentric tubes is difficult

to prevent, and shrinkage of the mesoporous silica often introduces gaps much larger than the size of the silica pores[44].

An alternative path to orthogonally oriented HCP pores can be developed by making an analogy to the approaches to obtain orthogonally oriented cylindrical mesophase in block copolymer films.[45-48] Selective removal of the minority block results in orthogonally oriented cylindrical pores in these films. However, the films obtained from oriented block copolymers are organic and cannot withstand high temperatures or pressure drops. The most important objective of this dissertation is to address this aspect of EISA process. The dissertation describes the synthesis of ceramic (silica and titania) films with orthogonally oriented cylindrical mesochannels on non-porous substrates by using a simple surface neutralization technique analogous to the method used for block copolymer films. The dissertation discusses extending the same idea to porous substrates to synthesize mesoporous silica membranes with cylindrical channels. Also, if we chose inorganic precursors for ceramics more active than silica, these films can be utilized in catalytic, optical, and electronic applications. An important example is titania, which is both photoactive and a semiconductor. This dissertation will address all of these aspects of the EISA process of oriented HCP films from synthesis to applications.

1.2.   Characterization

Characterization of mesoporous thin films is an important aspect of understanding the effects of synthesis parameters in these films for various applications. In this section, the characterization tools heavily used in this dissertation are introduced. First, characterization of films on non-porous substrates (glass slides or silicon wafers) will be discussed, and then the characterization of the films on porous substrates (anodized alumina membranes) will be discussed.

1.2.1.   Films on non-porous substrates

As mentioned earlier, this dissertation discusses the synthesis of mesoporous silica and titania films on glass slides. Also, the evolution of silica films dip coated onto Si wafers will be used to study the evolution of the silica network using FTIR spectroscopy. Films on non-porous substrates were characterized to determine the structure and uniformity using several techniques. Thickness of the films on silicon wafers was determined using a Gaertner 7109-C-338G ellipsometer and also (for films on glass or silicon) by using a Dektak 6M Stylus profilometer with a diamond stylus.

1.2.1.1. Scanning Electron Microscopy

Scanning Electron Micrscopy (SEM) is used to image the films on glass slides. The sample is placed on the SEM sample stage and then is scanned with an electron beam. The scattered electrons are used to obtain the surface image. Unlike TEM, this technique does not require transferring the sample onto grids, for electron transparency which makes this and ideal technique to obtain orientation information because we are not removing the films from the substrates (TEM sample preparation will be dealt in the next subsection). For ease of sample preparation we use cover slips instead of glass slides, which are much thinner than glass slides. Thinner sample makes focusing easier, resulting in better images. However, in some cases the images are collected from samples on thicker glass slides. SEM images are recorded on a Hitachi S-900 field emission microscope. Samples are cut into 2.5 mm × 10 mm size pieces and are mounted on a copper stub coated with colloidal graphite. The sample is then coated with a thin layer of Au/Pd to improve the charge transport on the sample surface, to avoid accumulation of charge. The sample is mounted on a stage and is enclosed and this closed area is kept in vacuum. Using Argon as carrier gas Au/Pd is deposited on the top of the sample surface. Using SEM we could characterize the uniformity of the films down to a size scale of approximately 10 - 20 nm. We presently think that the Au/Pd layer used in the sample preparation is making it difficult to see features that are smaller than 100 nm. As shown in chapter 6 we use SEM to image the anodized alumina membranes coated with silica film. Although we can see that the silica film covers the top of the alumina substrate and there are no defects in this alumina-silica composite membrane, we are not able to see the 5 nm pores in the silica film. In chapter 7 we show SEM images of titania films showing the pore structure. These samples are not coated with Au/Pd. Conductivity of titania helps to obtain SEM images without coating the sample with Au/Pd. Titania films coated with Au/Pd do not show the pore structure. However, because silica is a poor conductor, a coating of Au/Pd is essential to obtain good images without the sample surface becoming charged. Even with these limitations in the SEM imaging of silica films, were were able to image the alumina substrates coated with silica films. These images helped us to confirm that the silica films are microscopically crack free, thus adding more evidence in addition the to the UV/vis data collected by filtering gold nano particles through these films (chapter 6).

1.2.1.2. Transmission Electron Microscopy (TEM)

TEM is a powerful imaging technique to image features down to the nanometer range. In this work we use JEOL 2000 FX and JEOF 2010 (field emission) microscopes. Unlike in SEM, TEM the imaging is done using the electrons transmitted through the sample. Therefore, this requires the sample to be electron transparent and also for the sample to hang in space in the path of the

electrons. To achieve this, Cu grids are typically used to suspend an electron transparent sample. The sample is then transported onto the grids and this grid is placed in the path of the electrons. Since glass slides or even thinner cover slips are electron opaque, typical sample preparation requires scraping off the film from the glass slides and suspending the scraped powder onto the Cu grid, which is then observed in the microscope. This sample preparation technique obliterates the orientation information of the mesochannels because the pieces of film removed by scraping are randomly oriented on the grid. With this sample preparation procedure, we only learn about the long-range order of the sample by observing projections of the 2D HCP structure.

To preserve the orientation information, conventional TEM sample preparation would require thinning the substrate from the back side by polishing, dimpling, and ion milling. Instrumental difficulties made this not possible, so we developed a method to lift the film off the substrate and to transport it onto a TEM grid. To do this, we evaporated a thin layer of CaF_2 on the glass slide, followed by a layer of SiO_2 using an e-beam evaporator. The first layer was initially deposited with the intention of using amine complexation to etch away the CaF_2. The second layer was deposited to make a surface which is similar to a glass slide. These modified slides were subjected to the same coating and processing procedures as the other samples. As will be described in Chapter 5, differences in thermal expansion coefficient caused delamination of the silica from the surface during calcination, thus making it unnecessary to etch away the CaF_2 layer. After delamination, whole pieces of film could be picked up and munted onto a TEM grid. This technique preserves the orientation of the mesochannels in plan-view images.

1.2.1.3.   Diffraction

Diffraction from materials is routinely used to determine the crystal structure. The same diffraction technique is used to determine the pore geometry in mesoporous materials. However, because the pore spacings are on the order of a few nanometers, the diffracted angles appear at low angles. Diffraction of both X-Rays (XRD) and electrons can be utilized to determine pore geometry. XRD generally requires a large amount of sample because the instrument samples a macroscopic area of a film. Electron diffraction is carried out in a TEM instrument, and requires only a small amount of material.

XRD is the technique in which in coming X-rays are scattered by the sample present in the path of the X-Rays. A sample with ordered arrays of atoms or pores will give rise to coherent scattering in certain directions of the X-Rays leaving the sample. A detector captures these diffracted x-rays to obtain crystallographic information. Broadly, the detectors are classified as 1-D and 2-D detectors. In a 1-D detection technique, the incoming x-rays are spread out over a planar area to hit the sample, and the leaving x-rays are detected by a detector that moves in a

circular path which does not lie in the plane of the sample. Peaks are detected as a function of angle between the direct beam and diffracted beam (2θ). If the incoming beam is diffracted by planes of atoms/pores that are separated by a spacing of d (d-spacing), diffraction peaks are observed when the following Bragg's law is satisfied:

$$n\lambda = 2d\sin(\theta)$$

where λ is the wavelength of the x-rays and n is an integer. 1-D XRD is also called powder x-ray diffraction (PXRD) and the geometry of the diffraction system is called Bragg-Brentano geometry. As the d-spacing increases the angle where we observe the peaks in PXRD pattern decreases for a monochromatic beam of incident x-rays. Depending on the pore geometry we will observe peaks from different planes. Based on the relationship between the d-spacings of these peaks the pore structure can be determined. For a 2-D HCP material we would expect to see peaks from (100) and (110) planes and their higher order reflections in powder materials. D-Spacings of these planes are related as $d_{110} = \sqrt{\left(\frac{3}{2}\right)}d_{100}$. Preferential orientation of HCP cylinders parallel to the substrate surface in thin film morphology aligns the (100) plane along the substrate surface. Therefore we do not see reflections from the (110) planes, which are usually seen in powder products. Therefore, we will see only (100) peak and its higher order reflections ((200), (300), etc.) for 2-D HCP mesophase in thin films. This pattern is similar for a lamellar mesophase in which we have layers of surfactant and silica stacked next to each other. However, the lamellar mesophase is not stable upon removal of surfactant, and the material loses its mesoscopic order upon calcination if it is lamellar. The 2-D HCP mesophase is stable upon calcination, and in fact the intensity of the XRD peaks increases upon calcination due to increased contrast between inorganic materials and the empty pores.

The other important information that we obtain from PXRD patterns of mesoporous thin films is about the orientation of the 2-D HCP cylinders. Orthogonally oriented cylindrical channels do not diffract the x-rays in the plane of the detector in conventional Bragg-Brentano geometry.[49] Fig. 1.1. shows the schematic of the PXRD detector and the sample with orthogonally oriented HCP channels. It also shows two diffraction spots coming from X-rays incident on the sample in a direction orthogonal to the plane of this paper. We can see that the diffracted beam lies in the plane of the sample, where as the detector in PXRD does not move in the plane of the substrate and hence does not show any reflections from the cylindrical channels even though they are ordered in a HCP structure. Absence of PXRD peaks along with TEM images of the sample showing HCP ordering implies orthogonal orientation of the 2D HCP pores in thin films.[50]

Unlike silica, titania can have crystalline walls. Using PXRD we should be able to characterize the kind of crystalline phase present in the titania walls by observing high-angle reflections.

10

However, detection of the peaks is difficult for materials with small crystallite size. The following equation (Scherrer's formula) gives the relationship between crystallite size (t) and the full width at half maximum (B):

$$B = \frac{0.9\lambda}{t\cos\theta}$$

where λ is the wavelength of the x-ray and θ is the Bragg angle. Titania walls are approximately 2 nm thick, resulting in smaller crystallites. The above equation suggests that these smaller crystallites would give rise to a high value of B, i.e. a very broad peak. The peak can become so wide that it is nearly impossible to detect relative to the noise in the data. However, because electrons have a much smaller wavelength, they give smaller B. Therefore, electron diffraction is best used to determine the crystallinity in samples with very small crystallites.

Another detection scheme commonly used in XRD utilizes a 2-D CCD detector. X-rays diffracted from the sample and observe with a 2-D detector give rise to spots or rings depending on whether the material is single crystalline or polycrystalline. All of the in situ studies discussed above use 2-D XRD to monitor the evolution of mesophase. Detailed explanation of various spot patterns and the corresponding mesophases can be found in those references.[26-28]

All of the PXRD patterns in this dissertation are collected with a Siemens D 5000 diffractometer and Bruker D8 diffractometer. The wavelength of the x-rays is 1.54 A°. We have also used the Grazing Incidence X-Ray Scattering (GISAXS) technique to determine the orientation of the HCP mesophase. The mechanism of operation of GISAXS is similar to the 2-D XRD but the angle of incidence is very small thus providing information from a thin beam passing through a thin film. GISAXS data ae obtained at the Advanced Photon Source at Argonne National Labs on beamline 8-ID using a wavelength of 1.675 Å and a sample-detector distance of 2010 mm. Data are collected with a 2048 x 2048 MarCCD with a pixel size of 79 µm.

Electron Diffraction (ED) is very similar to XRD with a 2D detector. Use of electrons in this case allows one to obtain crystalinity information for smaller regions and smaller crystallites compared to x-rays. ED patterns are collected with a TEM instrument using a 2-D detector, and their indexing is similar to 2-D XRD. Obtaining data from a smaller region allowed us to prove the presence of crystalline titania walls even though the crystallite size is too small for XRD (Chapter 7).

1.2.2. Films on porous substrates

Oriented mesoporous silica films are also dip coated onto anodized alumina supports as a part of this dissertation. The resulting silica membranes are expected to have orthogonally oriented cylindrical pores with pore size ~ 5 nm. SEM is used in this case to confirm that defect-free silica membranes are deposited. SEM would characterize the cracks whose dimensions are of the order of 100 nm. To characterize the cracks that are much smaller in dimension, we pass gold nano-particle suspensions through the membranes and use UV/Vis spectroscopy to detect their presence. Since the pore sizes are around 5 nm, we would expect that the silica membrane will completely block particles that have sizes greater than 5 nm and will allow particles with sizes less than or equal to 5 nm. Therefore, we filter 20 nm and 5 nm gold colloids and detect their presence in the filterate product using UV/vis. Also, flow rates through the membranes are measured by passing ethanol through the membrane. Using a filter-holder assembly (purchased from Fisher Scientific) we measure the flow rates through the membranes at varying pressure drops. Using the following Hagen-Poisseuille equation the diameter of the pores is estimated.

$$ J = \frac{\varepsilon r^2 \Delta p}{8\mu L} $$

where J is the flux observed, ε is the porosity of the silica membrane (calculated by assuming that refractive index of the porous silica film measured by ellipsometry is a linear combination of refractive indices of silica and air with porosity as coefficient), Δp is the pressure drop, μ is the viscosity of ethanol and L is the length of the flow. It is assumed that the resistance to flow comes only from the silica film, and that the alumina membrane offers no resistance. This is reasonable because of the pore size of alumina pores is described by the manufacturer to be 200 nm, which is approximately 50 times that expected in the silica pores. Also, flux through the uncoated Anodisc membranes is much faster than it is through the coated membranes – so fast that it is difficult to measure accurately. The length of the flow (L) is approximated to be twice the thickness of the silica film because silica film is present on both the sides of alumina membrane.

1.3. Scope of the dissertation

Surfactant templated thin film materials find applications in numerous fields: catalysis[51], adsorption[52], sensors[53], membrane separations[40], drug delivery[54], photovoltaics[55], electronic materials[12, 56], fuel cells[57], etc. The list is almost endless. In all of these applications, aligned HCP

pores either improve the properties for the application or serve as a well-defined model of the porous material.

Silica has been the most studied and utilized material in this field. As a prelude to describing the synthesis of silica films, Chapter 2 addresses the chemistry of the sol-gel precursors reacting in presence of surfactants. In this chapter, we discuss the Fourier Transformed Infrared Spectroscopy (FTIR) experiments on mesoporous silica films to understand the kinetics of the silica polycondensation in surfactant templated thin films as a function of parameters like charge on the surfactant head group, humidity of the curing environment. Chapter 3 details a series of Monte Carlo simulations of the 2-D HCP surfactant mesophase behavior in confined spaces. This chapter also explains the underlying theory for the alignment of anisotropic mesophases orthogonal to a chemically neutral surface.

The description of the synthesis of orthogonally tilted HCP silica films is described in Chapter 4. Parameters used to induce orientation include modification of the substrate surface and film thickness. Effect of film thickness on the orientation of HCP mesophase is described in chapter 5. Chapters 6 and 7 discuss two applications for these orthogonally tilted 2-D HCP films. First, synthesis of mesoporous silica membranes on porous alumina supports will be discussed in chapter 6. Other metal oxides, such as titania[51] and zirconia[57] are also finding increasing use because of their potential applications in the area of semiconductors and alternative energy sources. Chapter 7 discusses parameters influencing the synthesis and processing of oriented 2D HCP mesoporous, nanocrystalline titania films and the application of these films in the area of photovoltaics.

In this dissertation, we focus primarily on trying to understand a few limited aspects of sol-gel thin film formation using EISA process, with particular emphasis on orienting the channels. The process used to orient the films is novel, and has been fundamentally characterized by FTIR. The impact of this thesis is expected to be the many applications made possible by these ceramic films, and two (membranes and photovoltaics) are demonstrated. There are many more fundamental aspects of surfactant templated sol-gel thin films and also their applications that can be addressed in future studies.
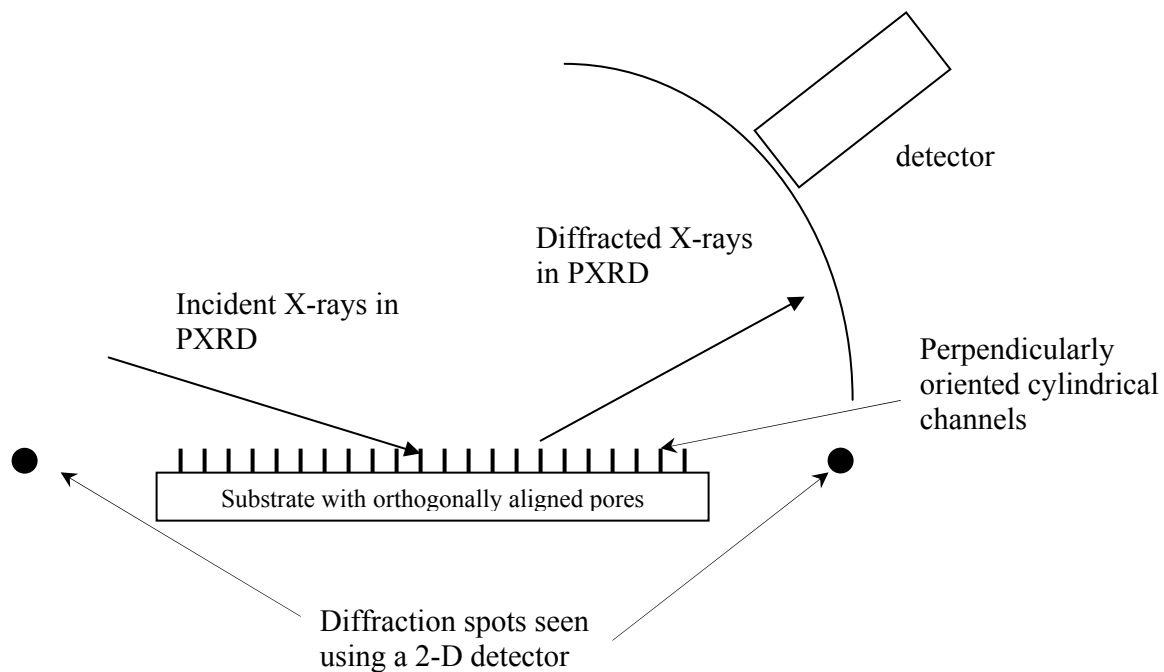
Figure 1.1. Schematic of PXRD set up. Sample has orthogonally alined cylindrical channels. Also included are 2D diffraction spots from X-rays hitting the sample in a direction perpendicular to the plane of paper.

Chapter 2 Investigation of the Kinetics of Silica Polycondensation in Surfactant Templated, Mesostructured Thin Films

2.1. Introduction

Surfactant templated mesoporous materials have been an active area of research since their discovery in 1992.[58, 59] Simple synthesis procedures, excellent control of pore size and shape and also ease of obtaining functional materials makes surfactant templation an ideal synthesis procedure for ceramics to be utilized in the areas of separations[60], adsorbents[61], optical materials[62], low K dielectrics[63], etc. These materials can be synthesized in the form of powders or films. Controllable pore orientation makes surfactant templated thin films find many more applications in the areas such as membranes, semiconductors and substrates for growing nano structures (wires, rods, etc.) compared to their powder counterparts. Evaporation Induced Self Assembly (EISA) procedure is a simple technique to synthesize these surfactant templated thin films.[64, 65] Ordered mesostructured thin films result within minutes in this EISA process.

Silica has been the most commonly synthesized inorganic material using surfactant templation. Other ceramic materials like titania and zirconia are finding increasing interests for their potential applications in semiconductors and also in the areas of alternative energy sources.[66, 67] While many studies have focused on obtaining materials with different pore geometries[68-70] and various functionalities[71-73], there have also been several reports of in situ and ex situ studies using 1-D and 2-D x-ray scattering and transmission electron microscopy (TEM) to understand the mesostructural changes occurring during the formation of templated mesostructured silica.[27, 28, 74-81] X-ray scattering and TEM aid characterization of these materials by giving a detailed picture of the evolution of the mesostructure and thus help to understand the effects of various parameters like pH, temperature, etc. on the mesostructure. These characterization techniques do not help our understanding of the chemical changes in the species present in the synthesis mixtures and their evolution during the entire process of meso- and micro- structure development. Understanding the microstructural changes in the silica network is essential to comprehend the synthesis mechanisms of these materials. Fourier Transformed Infrared (FTIR) spectroscopy and Nuclear Magnetic Resonance (NMR) spectroscopy have been the most widely used tools to characterize the chemical changes during the evolution of silica from sol-gel precursors.

Significant quantitative efforts to understand sol-gel reactions in the synthesis of silica began over three decades ago. Brinker gives an excellent review on the early work on the hydrolysis and condensation reactions of silicates and their influence on the final structure obtained.[82] He reviews both acid and base catalyzed reactions and explains the structural trends on the basis of

the pH and [H_2O] dependence of the hydrolysis, condensation and dissolution reactions. West et. al. report quantum calculations of rings and chains of sol-gel silica to understand the gelation process of sol-gel silica.[83] They try to address the structural energy differences between chains and rings and also the change in structure and molecular energy when a stable silica ring of four tetrahedra is subjected to H_2 adsorption and desorption.

Several studies on silica films and gels synthesized in the absence of surfactants aim at understanding the structural changes in the silica framework during the curing process starting from alkoxide precursors. Wood et. al. studied the alkoxide silica gels by IR spectroscopy.[84] They discuss various bands present in a typical IR spectrum of a silica gel obtained from alkoxide precursors, focusing on the band around 960 cm^{-1} arising from vibration of dangling Si-OH bonds present in the gels. They conclude that the intensity of this band scales in a general way with the surface area of the deposited films. Matos et. al. have used both IR and Raman spectroscopy to study the time evolution of the acid-catalyzed hydrolysis and condensation of tetraethoxysilane (TEOS) in ethanol, to form silica xerogel.[85] This study clearly identifies various bands arising from different bonds present in the system, which are used to quantify the extent of hydrolysis and condensation reactions occurring in the system. Yoshino et. al. have used IR spectroscopy to study the structural evolution of sol-gel derived SiO_2 gels in the early stage of conversion to glasses.[86] They synthesize silica gels under partial hydrolysis conditions and monitor the structural changes during early stages of gel to glass conversion as a function of behavior of IR band intensity at 550-600 nm^{-1} originating from the skeletal vibration of the 4-fold siloxane rings. NMR was also used to study the polymerization of SiO_2 in acid catalyzed sol-gel systems[87]. Assink and Kay review the influence the utility of reaction conditions on the pathways by which the sol-gel derived materials are prepared.[88] They also review the study of sol-gel kinetics by NMR spectroscopy.[89] Several works from the same group describe the utility of NMR to study the hydrolysis and condensation of sol-gel silica.[90-93] Pouxviel et. al. also use NMR to understand the hydrolysis and condensation of silica under acidic conditions starting from teraethoxysilane. The extent of reactions as a function of water composition and pH are studied.[94, 95] Devreux et. al. utilized NMR spectroscopy to follow the sol-gel kinetics of silica monoliths until gelation, and correlated their findings with simulations and small angle x-ray scattering studies. Rankin et. al have also used Si NMR to understand acid and base catalyzed hydrolysis and condensation of tetraethoxysilane and organically modified silanes.[96-98]

There have been several reports on using IR spectroscopy to understand the structural changes in surfactant templated silica powders. Calabro et. al. studied the hydrothermal mesoporous silicate synthesis process in situ using ATR-FTIR spectroscopy.[99] They monitored absorption peaks due to the growing silicate framework and surfactant micelles, illustrating the utility of

ATR-FTIR in probing the structural changes occurring during the formation of mesoporous silica. Holmes et. al. monitor the formation of MCM-41 in situ using FTIR spectroscopy.[100] By monitoring the Si-O bands in the IR spectra they conclude that silica oligomers react rapidly with the surfactant cations in a co-operative assembly process to give embryonic MCM-41 nuclei. Tejedor-Tejedor et. al. have monitored the hydrolysis and condensation of tetraethyl orthosilicate (TEOS) in HNO_3 solutions (pH 2-3) using in situ ATR-FTIR spectroscopy by measuring the concentrations of various reactants and products.[101] All of these studies mainly concentrate on understanding the synthesis mechanisms of mesoporous silica powders using surfactant templation.

Several papers report IR studies monitoring the hydrolysis and condensation of sol-gel silica thin films. Innocenzi gives an excellent overview of infrared spectroscopy of sol-gel derived silica films.[102] That article reviews the correlation between IR spectra and microstructure of sol-gel silica films, and explains the various bands occurring in the IR spectra of sol-gel silica thin films. There have also been some studies directed at understanding the effects of various parameters like the aging environment and temperature of curing on the microstructure of the silica films. Primeau et. al have discussed the effect of thermal annealing on aerosol-gel deposited SiO_2 films using FT-IR deconvolution.[103] They have isolated several overlapping bands in the IR spectra and could assign them to several vibrational modes of the different bonds present in the system. They have also discussed the origin and the temperature dependence of these peaks. Parrill studies the acid catalyzed sol-gel silica coatings using transmission IR,[104] and identifies bands occurring due to various bonds. Monitoring the changes in these bands from 1min after coating in various environments reveals evidence for the presence of 4-member rings in the silica films. Muroya correlates the formation of silica skeleton structure in silica films to FTIR spectra.[105] He found that the wave number and the band intensity of each band in the IR spectra depend on the viscosity of the sol used for film preparation. He also points to the formation of 3 or 4 membered rings during the initial stages of condensation. Innocenzi et. al. study the order-disorder transitions and evolution of silica structure in self-assembled mesostructured silica films using FTIR spectroscopy[106] using cetyltrimethylammonium bromide as the surfactant template. Mesoporous films with *Pm3n* cubic phase were thermally treated in air up to 1000 °C. They were able to successfully resolve the LO3-TO3 pair (Longitudinal optic – transverse optic splitting of the asymmetric Si-O-Si stretch), cyclic species absorption bands and also disorder-order transition bands (LO4-TO4). A recent study from Innocenzi et. al. has used time resolved FTIR spectroscopy as an in situ tool to study the kinetics of self-assembly in mesostructured films.[107] Although the study identifies various stages of drying during the initial

minute of drying of the films, there is no attempt to understand the effect of the surfactants on the kinetics of the polycondensation of silica.

Many of the above mentioned studies concentrate on the evolution of silica microstructure in silica gels, without surfactants. Detailed studies on structure evolution in surfactant templated silica have mainly concentrated on powder products. To our knowledge the two reports from Innocenzi et. al. are the only studies that attempt to understand the evolution of silica microstructure in surfactant templated silica films, though there has been no attempt to measure the kinetics of the condensation process under different curing environments and different sufactants.[106, 107] Also the time scales in the present study are on the order of several minutes after deposition unlike the previous studies which mainly focus on the changes occurring during the initial minute after deposition.

In this chapter we describe our efforts to gain insight into the silica polycondensation in surfactant templated thin films both before and after the deposition. Prior to deposition we monitor the changes in various bands at different times during the synthesis of the coating sol. We use ATR-FTIR as our characterization technique. The appearance and disappearance of various bands are qualitatively monitored. After depositing the silica films on Si wafers, transmission IR spectra of the deposited films are collected. After successful identification of several bands we monitored the changes in the band around 960 cm^{-1}. Changes in the intensity of this band signify the degree of condensation. We therefore use this IR band as a tool to monitor the effect of various parameters like the kind of surfactant and curing environment for the films on the condensation of the silica.

2.2.   Experimental Section

In this work we used three surfactants: P123, a triblock copolymer with average block composition $(EO)_{20}(PO)_{70}(EO)_{20}$; cetyltrimethylammonium bromide (CTAB); and Brij-56, a hexadecyl ether of polyethylene oxide with the primary component being decaethylene oxide hexadecyl ether. Tetraethoxysilane was used as silica precursor. A stock solution of pre-hydrolyzed silane was prepared using the procedure described else where.[108] First, TEOS, ethanol, water and HCl (mole ratio 1 : 3.8 : 1: $5*10^{-5}$) were refluxed at 70 ºC for 90 minutes. Then, the remaining water and HCl were added, increasing the concentration of HCl to 7.34mM. After stirring this mixture at 25 ºC for 15 min, the sols were aged at 50 ºC for 15 min. The required amount of surfactant was dissolved in ethanol and this solution was added to the above aged silica sol with constant stirring. The final mole ratios were 1 TEOS : 22 C_2H_5OH : 5 H_2O : 0.004 HCl : 0.01 P123 / 0.055 Brij-56 / 0.098 CTAB. Slides were dip coated with this sol at a withdrawal speed of 7.6 cm/min.

During the sol preparation a small amount of the coating solution was withdrawn at regular intervals and the IR spectrum of this solution was collected using a ZnSe ATR trough accessory from Pike Technologies. To obtain the IR spectra of the coated films, a 1 cm × 1 cm section of (100) Si wafer was first cleaned using deionized water, acetone and isopropanol in that sequence. This cleaned Si wafer was held between two magnets and this system (Si wafer between two washer-shaped magnets) was mounted inside of a 5 cm-pathlength gas cell accessory for the FTIR spectrometer to collect the background. The gas cell is a closed cylindrical cell capped at both ends with IR-transparent ZnSe windows through which the IR beam enters and then leaves. The cell has an inlet and an outlet to purge any gas, thus allowing us to keep the sample the in desired environment without contaminating the IR compartment. In this work we have passed vapor with different degrees of moisture (from completely dry N_2 to saturated water vapor). After collecting the background the Si wafer is coated with the silica sol synthesized as described above, and is transferred into the gas cell immediately to collect the spectra as a function of time. It typically takes 50 sec to transfer the wafer into the gas cell after coating. Therefore, the earliest spectra of the silica films that we present in this work were collected ~50 sec after coating.

The thickness of each film after complete curing was estimated by measuring the thickness of films coated from the same sols onto silicon wafers, using a Gaertner 7109-C-338G ellipsometer. FTIR spectra were collected on a ThermoNicolet Nexus 470 FTIR spectrometer.

P123 (BASF), CTAB (Aldrich), Brij 56 (Fluka), TEOS (>99%, Fluka), deionized ultra filtered water (Fisher), anhydrous ethanol (Aaper Alcohol & Chemical) were all used as received. (100) cut single-side polished silicon wafers were obtained from University Wafer.

2.3.　　Results and Discussion

For all three types of surfactants, uniform, defect free SiO_2 films were deposited on Si wafers using the procedure described above. Thickness of the films after curing was measured to be approximately 250 nm. Before discussing the kinetics of curing, the reactions occurring during sol aging are discussed. The IR history of the precursor sol was obtained before depositing the sol on Si wafers. This was done by withdrawing a small amount of sol at different time periods and obtaining the IR spectrum using a ZnSe ATR trough accessory.

Fig. 2.1 shows a typical IR spectrum of the sol after the addition of surfactant. Also included are FTIR spectra of pure TEOS and ethanol for comparison. In this case, the FTIR spectrum just before coating of a sol containing P123 is shown. Spectra of sols with other surfactants (CTAB and Brij-56) show similar bands, except for the bands coming from surfactant. The bands in the spectra are assigned based on literature assignments and comparison to the ATR-FTIR spectra of

pure TEOS and EtOH. Table 1 gives the details of various bands that are seen the spectrum. Fig. 2.2. shows the IR spectra of the sol at different stages from the point of adding the initial amounts of TEOS, H_2O, EtOH and HCl to the final stage after adding the surfactant. For clarity, the spectra are shown in the wave number range of 1800 cm^{-1} to 650 cm^{-1}. No significant changes were seen in the high-wavenumber portions of the spectra. As summarized in Table 1 we can identify several bands and their possible origins.

At the far left end of the spectrum in fig. 2.1 we see a very strong, broad band centered near 3330 cm^{-1}. This is the O-H stretching band, and is broad because the IR sol contains several O-H containing compounds in various states of hydrogen bonding that contribute to this band.[101, 109] Ethanol, H_2O and Si-OH all contribute to the appearance of this band. Also at high wavenumber, there are bands near 2980 – 2870 cm^{-1} caused by the C-H stretches from ethanol, ethoxide groups of TEOS or partially hydrolyzed silanes, and the surfactant.[101] Because of the large number of contributors to the high-wavelength bands, we could not learn a great deal about the evolution of the sol from these bands.

At lower wavenumbers, Fig. 2.2 reveals more information about the evolution of the sol. The band due to bending of molecular water occurring at a wave number of around 1640 cm^{-1} decreases over the initial 90 min aging period at 70 °C because of its consumption during the hydrolysis of TEOS.[109] Intensity of this band increases again after adding the remaining H_2O and HCl and remains high because the final amount of water is greater than the stoichiometric amount for TEOS hydrolysis. For the final spectrum (after adding surfactant), dilution causes the intensity of this band to drop significantly. These changes are depicted in fig. 2.3 which plots the height of the H_2O band near the wavenumber 1642 cm^{-1} vs. time. The gradual decrease of intensity of the water bending band over the first 90 minutes of aging is also accompanied by decreases in the intensities of the bands associated with CH_3 rocking motion[101, 110] and C-O symmetric stretch[111] in TEOS around wave numbers 1168 cm^{-1} and 790 cm^{-1} respectively.   The intensities of these bands drop to almost zero after the addition of the remaining HCl and H_2O by the end of the second aging step, due to further ethoxide hydrolysis. In fig 2.3 we also plot the height of the band around 790 cm^{-1}. We can see the decrease in the band intensity during the initial 90 min period and this band completely dissapears after adding the surfactant.

The IR bands between wave numbers 1350 cm^{-1} and 1500 cm^{-1} occur due to various deformations in the CH_2 and CH_3 that are explained at greater detail elsewhere.[101, 110] Another important feature of the spectra is a band near 960 cm^{-1} coming from the stretching of the Si-OH bond.[109] Unfortunately, this region (~ 960 cm^{-1}) also contains bands from C-C stretching and CH_3 bending deformations of ethanol.[101, 110] Because of this overlap, it is difficult to deconvolute the contributions of Si-OH from the ethanol bands in the sol; this problem will be alleviated after

the films are deposited and the ethanol has evaporated. Still, the appearance of this band signifies the presence of silanols after hydrolysis of the ethoxysilanes. The region between 1120 cm^{-1} and 1020 cm^{-1} contains bands originating from the anti-symmetric stretching of the Si-O-Si[102] and also from the C-O and C-C stretches of TEOS[85] and ethanol[101] At this point when the sol contains hydrolyzing TEOS species the bands are probably due to TEOS and ethanol (ethanol is the solvent). This region also has bands originating from the bending of CH_3 and CH_2 bonds of the organic species present in the solution. The overlapping bands in this region are difficult to interpret clearly due to the high concentration of ethanol, although Tejedor-Tejedor et. al.[101] and Mondragon et. al.[111] discuss the interpretation of this region of the spectrum. We will find that when the ethanol is removed, the siloxane bands can be clearly resolved. Also in Fig. 2.1 we can see a small peak at 802 cm^{-1}. This can be caused by Si-O-Si symmetric stretches,[102] but it appears close to bands due to CH_2 and CH_3 rocking motions.[110, 112, 113] Another band of significant intensity appears around 879 cm^{-1}, and is due to the stretching of C-C/C-O bonds in the ethanol present in the system.[101] The set of spectra if Fig. 2.2 suggest that the silica sol is completely hydrolyzed before coating, and that there is no significant concentration of hydrolysable ethoxy groups present in the system after adding the surfactant (no peaks at 1168 cm^{-1} and 785 cm^{-1} present in the sol after adding the entire H_2O and HCl).

In the procedure described above we add H_2O and HCl in two stages. After prehydrolyzing the sol for some time we add the the surfactant dissolved in ethanol. To see the if adding the entire H_2O and HCl amounts at once will make any difference to the condensation of the sol, we did the same experiments by adding the entire amount of HCl and H_2O at the beginning. Although this resulted in immediate hydrolysis of TEOS the final sol (after adding the surfactant) had IR spectrum that is similar to the IR spectra of the sol prepared by adding HCl and H_2O in two stages. However, the films coated from these two sols showed different degrees of condensation of silica in the IR spectra. Fig. 2.4 plots the IR spectra of the films coated on Si wafers obtained 1 min after deposition of the films from two different sols. One of the sol was made by adding the H_2O and HCl in two stages before adding the surfactant, P123 (case A) while the other sol was made by adding all of the HCl and H2O at the beginning and was prehydrolyzed for 90 min at 70 °C before mixing with P123 dissolved in ethanol (case B). Only the spectra in the range of 1350 cm^{-1} to 1000 cm^{-1} are shown to highlight the band originating from asymmetric stretching of Si-O-Si. The position of the band near 1100 cm-1 appears at slightly different locations for the two cases. In case A the band occurs at 1100 cm-1, whereas it appears at 1107 cm-1 for case B. Both these bands have shoulders on the high frequency side, although the shoulder is more pronounced in case B, signifying a higher degree of condensation.[102, 103] Also the shifting of the Si-O-Si asymmetric stretching band to higher wave numbers signifies the enhancement of the

TO3 mode of the Si-O-Si bond indicating the presence of more Si-O-Si bonds in case B than in case A. This signifies the importance of addition of HCl and H_2O in two different stages to obtain films with more hydrolysable silanols, which should correspond to a network which is more flexible immediately after coating. From the above discussion, we conclude that there are several IR bands whose origins can either be attributed to ethanol present in the system or to siloxane-containing species. There is no clearly resolved IR evidence for the onset of silica condensation in the diluted sol. However, we can clearly say that TEOS is completely hydrolyzed prior to coating. Some condensation of these hydrolyzed silica precursors is unavoidable. With this information about the bands observed in the IR spectra of the sol we will proceed to discuss the IR spectra after the sol is dip coated onto Si wafers. Tejedor-Tejedor et. al.[101] and Mondragon et. al.[111] give excellent review of various bands observed in systems of reacting TEOS dissolved in ethanol.

Fig. 2.5 shows a typical IR spectrum of a P123-containing silica films on a Si wafer, 20 hrs after depositing the film. Ethanol evaporates quickly during coating, and water evaporates until it reaches equilibrium with the film during the initial minutes of curing. The only components in the film 20 hr after deposition are condensed silica precursors and the surfactant. Starting from the left end of the spectrum we see the O-H stretching band at around 3350 cm^{-1} due to dangling Si-OH bonds and possibly adsorbed water. The strong bands between 3000 – 2800 cm^{-1} wavenumbers are caused by the C-H stretching vibrations of the surfactant. The peaks between wave numbers 1500 – 1330 cm^{-1} are caused by the CH_2 and CH_3 vibrations of the surfactant species. The strongest band in the spectrum occurs at a wave number 1079 cm^{-1} and also has a shoulder on the higher frequency end. This is caused by the antisymmetric stretching motion of the O atom in Si-O-Si bond parallel to the Si-Si line.[102] The intense shoulder on the high frequency end of this band is caused by the longitudinal optic – transverse optic (LO-TO) splitting of the vibrational modes. The band at wave number ~955 cm^{-1} is due to the Si-OH stretching of the silanols. The band at wave number ~798 cm^{-1} is due to the symmetric stretching of the O atom along a line bisecting the Si-O-Si angle.[36] A broad band around wave number 600 cm^{-1} can be attributed to the cyclic species.[102] There have been several reports in the literature proving the presence of 4-fold and 6-fold siloxane rings. vanBeek et. al report NMR evidence for the presence of cyclic species in the synthesis sol during the early stages of hydrolysis and condensation.[87] Several researchers have found evidence for ring structures in sol-gel silica films and have attributed the broad peak between wave numbers 550-640 cm^{-1} to their presence.[102, 103, 106] The band at ~ 450 cm^{-1} comes from the transverse-optical (TO) rocking motions perpendicular to the Si-O-Si plane of the oxygen atoms bridging two adjacent Si atoms.[102, 103]

As mentioned earlier, we studied the kinetics of the silica condensation in surfactant templated films after deposition by monitoring the changes in the intensity of the silanol stretching band around wave number 960 cm⁻¹. Fig. 2.6 shows the IR spectra as a function of time elapsed after coating of silica films with different surfactants cast onto silicon wafers. The spectra shown in Fig. 2.6 were collected in a highly humid environment (relative humidity ~ 95%) achieved by passing laboratory air saturated with water through the IR gas cell. For clarity we have shown the spectra only in the 600-1400 cm⁻¹ wave number range, which include the band originating from the stretching of silanols (~ 960 cm⁻¹) and also the band from Si-O-Si antisymmetric stretches (~1070 cm⁻¹). To obtain a clear view of the silanol band we present the data in the reverse of the usual spectrum orientation (with wavenumbers increasing from left to right). We can clearly see that the intensity of silanol band decreases as a function of time for all samples. This is consistent with the fact that the hydrolyzed silica precursors are condensing and thus decreasing the concentration of silanols.

An important observation that can be drawn from Fig. 2.6 is that this decrease in intensity of the silanols depends on the type of the surfactant present in the system. When the surfactant used is P123, the silanol intensity remains constant for almost 20-30 min after coating and then decreases to reach a steady state value (Fig. 2.6a). We define this induction period as the time T_i during which the silanol band intensity does not decrease appreciably, and therefore we can infer that condensation does not begin. When the surfactant is changed to Brij-56 (Fig. 2.6b) we still see the delayed condensation as was observed in Fig. 2.6a, but the induction period is reduced to T_i ~ 10-20 min. When the surfactant used is CTAB (Fig. 2.6c), condensation starts immediately after depositing the film, resulting in a continuous drop in the silanol band intensity immediately after film deposition (T_i ~ 0). To quantify these observations, Fig. 2.7 plots the peak height of the silanol band vs. time film deposition for each of the surfactants. The relative humidity of the environment is ~ 95% and base line corrections were applied to every point in this plot. This plot clearly depicts the changes occurring in the silanol band as a function of the surfactant. The induction time (T_i) before which condensation proceeds at a conspicuous rate, is maximum when P123 is used as a surfactant, followed by Brij-56. When CTAB is used as surfactant we do not see any induction time and the silanol band intensity drops immediately after coating.

These changes in the silanol band are also accompanied by corresponding changes in the band at wave number around 1070 cm⁻¹ attributed to antisymmetric stretching of Si-O-Si bonds. To show clearly the types of changes observed, Fig. 2.8 plots the IR spectra of the P123 templated silica films as a function of the time elapsed after deposition in a 95% relative humid environment from t = 1min to t = 75 min. Also included is the IR spectrum of the silica film after calcination at 500 °C for 4 hrs. Only the region between wave numbers 1300 cm⁻¹ to 850 cm⁻¹ is

shown to highlight the bands originating from asymmetric stretching of Si-O-Si and silanols. The broad intense peak ~ 1100 cm^{-1} shifts from high wave number to lower wave numbers. This peak shifting phenomena is also accompanied by the development of a shoulder on the high wave number side. This shoulder can be attributed to LO splitting of the TO3 stretching mode.[102] The observation of this shoulder has particular importance in sol-gel materials, especially in thin films, because it has been observed that the LO3 modes are not detected, or weakly detected in films where the structure is not crosslinked enough.[102, 103]

We can clearly see the enhancement of the TO3 and LO3mode intensities as the film evolves. This is also accompanied by the shift in the TO3 mode to lower wave numbers to ~1070 cm^{-1} and the LO3 mode to higher wavenumbers to a final value ~ 1250 cm^{-1} upon calcination. This is also accompanied by the complete disappearance of the peak around 960 cm^{-1} originating from the stretching of the Si-OH bond in the calcined sample. This also signifies the complete condensation of the silica network upon calcination of the film.

Perhaps the most important observation in Fig. 2.8 is that this increase in intensity and onset of drift of the TO3 peak to lower wave numbers coincides with the onset of decrease in Si-OH band intensity. Once the Si-OH band reaches a steady state value there is almost no change in the location of the TO3 and LO3 bands. Significant changes occur after this stage only upon calcination of the silica film which induces complete condensation of the silanols. This demonstrates that the induction period in the P123 and Brij-56 templated films is truly due to a delay in the onset of condensation. Brij 56 templated films also show the same features as P123 templated films with respect to the changes in the TO3 and LO3 band positions during the aging of the film. When CTAB is used as surfactant the splitting of the TO3 and LO3 was seen in the very first spectrum of the film. No changes were seen after that.

The other variable investigated in this work is the dependence of T_i on the humidity of the environment in which the coated silica film is cured. Fig. 2.9 plots the peak heights of the Si-OH stretching band near 960 cm^{-1} vs. time for P123 templated films as a function of the gas-phase humidity during curing. Spectra are obtained in conditions ranging from completely saturated with water vapor (~95% relative humidity) to dry N_2 environment (~ 0% relative humidity). We can see that the induction time increases as the humidity increases for P123-containing films. In the dry N_2 environment we are not even able to resolve changes in the silanol band intensity, but we attribute this to fast condensation of the silica network before we are able to start measuring spectra in this case. To confirm that the condensation of silica in a dry N_2 environment is rapid, we examine the changes in the FTIR spectra induced by first allowing humid air to pass through the gas cell in which the coated silica film is cured, and suddenly changing the environment to dry N_2. This change in environment induced a drastic drop in the silanol band intensity. Fig. 2.10

shows the height under the silanol band for a P123 templated film as a function of aging time after coating the film. The film was initially kept in an environment saturated with water vapor. 9 min after deposition, the environment was changed to N_2. We can clearly see that intensity of the silanol band drops instataneously at this point suggesting that the N_2 environment induces fast condensation of the silica network. The change in induction time can therefore be explained by the change in the gas phase water content. A small of water in the vapor phase allows condensation to proceed immediately, while increasing the amount of water increases the water content of the film, and therefore slows the condensation reaction. This effect is large for P123 surfactants because of the hydrophilicity of the poly(EO) headgroup.

Figs. 2.11 (a) & (b) plot the peak heights of the Si-OH stretching band near 960 cm^{-1} vs. time for brij-56 and CTAB templated films respectively as a function of the gas-phase humidity during curing. Brij-56 templated films respond to humidity in a way similar to P123 templated films except for shorter induction time periods. We see that as the humidity increases the induction time period for these films increases and when the film is cured in 0% relative humidity N_2 atmosphere, we do not see any changes in the curve. Similar to P123 templated films, this phenomena can be attributed to fast condensation of the silica network in N_2 atmosphere, before we were able to start measuring the spectra. CTAB templated films donot show any dependence of silanol band intensity as a function of the gas phase humidity except for the case when the gas phase is N_2. Similar to P123 and Brij 56 templated films, we were not able see any changes in the silanol band in N_2 atmosphere because of fast condensation of the silica network.

As we have seen, however, the induction period length also depends on the type of surfactant. Condensation is delayed for the longest time if the surfactant used is P123. With Brij-56 we still see the delayed condensation but T_i (Brij-56) < T_i (P123). If the surfactant used is CTAB the condensation starts immediately without any delay and T_i (CTAB) ~ 0 min. We attribute this to the structure of the surfactant. P123 ($(EO)_{20}$-$(PO)_{70}$-$(EO)_{20}$) has large polymeric head group. In sol-gel derived silica materials there is evidence in literature for head group penetration into the silica walls in P123-templated materials, resulting in microporosity in the silica network.[114-116] This penetration is more for P123 than for Brij-56 because of difference in the head group size. The terminal OH groups of the headgroups of the EO-based surfactants can also interact with the silica wall to esterify the silanols and generate Si-O-$(EO)_x$ bonds. Both penetration of headgroups into the silica walls and the presence of OH groups contribute to the induction period. When the surfactant used is Brij-56 ($CH_3(CH_2)_{15}(EO)_{10}$) which also has a polymeric head group we again see the delayed condensation of silica. However, because of the smaller head group in Brij-56, condensation is not slowed down as much as in case of P123 templated films.

CTAB ($CH_3(CH_2)_{15}N(Br)(CH_3)_3$) on the other hand has an small ionic head group, which is not expected to penetrate into the silica network.[114] We therefore think that the condensation is not slowed down, and therefore we do not see any induction time with CTAB.

There have also been prior studies on the effect of the relative humidity and the solvent vapor pressure of the environment on the mesostructure of the dip coated films. Sanchez et. al. discuss the effect of the relative humidity during the deposition on the final mesophase obtained.[76] They propose that there is a modulable steady state during which the mesostructure of the silica films can be changed depending on the relative humidity of the coating environment. They found a change in the mesophase by changing the relative humidity of the coating environment 10 min after film deposition, unlike many previous studies which assume that in the EISA process, all changes happen during the initial seconds after deposition. Though Sanchez et al. do not get into the details of the silica condensation during this time period, they attribute mesostructure changes to the transfer of water molecules between the film and the environment. The present study explains the reasons for such an observation in terms of the silica condensation process, which is influenced by both the relative humidity of the environment and the kind of surfactant present in the system. Babonneau et. al. have used in situ X-ray scattering experiments to understand the effect of pH of the coating sol and the ethanol vapor pressure of the coating environment on the mesophase finally obtained in surfactant templated silica films.[78] They observed that high ethanol concentrations in the vapor phase maintains high ethanol concentration in the films. This results in films with low viscosity and thus promotes phase transitions. Although they could not conclusively explain the role of the ethanol vapor and suggest further spectroscopic studies to explain the effects of these parameters in terms of the silica condensation, their work suggests that conditions of the vapor phase during the film curing will influence the mesoscale organization occurring with the films. Though we do not explain the effect of the relative humidity of the coating environment on the final mesophase formed (which is explained by Sanchez et. al[76]), we demonstrate the existence of an induction time after the deposition of the silica films, when the silica condensation is slowest. This induction time can be used to alter the environment of the deposited films to achieve specific goals. The coated films can be brought into contact with functional surfaces to alter the alignment of the mesophases[117], obtain different mesophases[76, 78] etc. In chapter 4 we will describe a process in which the cylindrical channels in P123 templated films are oriented in a direction orthogonal to the substrate by sandwiching the films between modified surfaces after the coating has already been deposited.[117] In this chapter we give a possible explanation for why this is even possible. The induction period that we observe is equivalent to the "modulable steady state" of Sanchez, and is longest for surfactants with large nonionic poly(EO) headgroups at high relative humidity.

This observation is important for two reasons. First, it shows that controlling the coating environment after curing is indeed quite important to obtaining reproducible results. The humidity (and by inference also the vapor pressure of the solvent) must be controlled to ensure that the mesostructure does not change (for instance due to swelling) while it is still in the induction period. Second, it provides the opportunity to utilize the induction time to engineer the film properties – for instance, to use sandwiching of films after coating to imprint functionality into the films or to manipulate the mesophase with physical or optical patterning, fields, or contact with surfaces.

2.4.   Conclusion

In this chapter, we have monitored the synthesisis of mesoporous silica films using CTAB, P123 and Brij-56 surfactants as templates. We used infrared spectroscopy to understand the kinetics of the sol-gel process both before and after depositing the silica films. Prior to film deposition, IR spectra of the sol were collected at regular intervals using ATR-FTIR. Monitoring various bands in the IR spectra of the sol, we could conclude that with the widely used sol preparation technique published by Lu et al., TEOS is completely hydrolyzed prior to deposition of the films.[64] This hydrolysis is accompanied with the growth of a Si-OH stretching band. After depositing the silica sol on Si wafers transmission IR spectra of the silica films were collected at regular intervals of time. Monitoring the bands from the silanols and the siloxane species we conclude that the condensation of the silanols in the film can proceed for a significant amount of time after coating deposition, and that the rate of condensation depends on the kind of surfactant used and also the relative humidity of the curing environment.

In some cases, we found evidence for the presence of an induction time after the film deposition (T_i) during which the condensation rate of the silica network was at its minimum and (presumably) the silica network is still flexible. Monitoring the silanol band intensity we conclude that if the surfactant used is P123, T_i is the maximum. In case of Brij-56, an induction period is still observed, but it is less than for P123. When the surfactant is CTAB, we do not see any induction time and the condensation starts immediately after depositing the film. We attribute these changes primarily to penetration of the poly(EO) chains of P123 and Brij-56 into the silica walls, perhaps also aided by interactions between the terminal OH groups of these surfactants with silica. The interaction of CTAB with silica is physical, and occurs only at the micelle-silica interface. Furthermore, we found with P123 that a humid environment enhances the delay in condensation. All of the changes in the silanol band intensity are accompanied by corresponding changes in the siloxane band intensity indicating greater solidifaction of the siloxane network. This is an important observation suggesting that the silica network in

surfactant templated mesoporous films is flexible for some time in the order of minutes, and can still be manipulated to do post-coating modifications.[117] Until today researchers in this area assume that changes in the mesostructure are complete within a few seconds or minutes after depositing the film. The current results suggest the existence of additional time frame in the order of several minutes for post synthesis modifications.

Table 2.1 IR bands observed and their band assignments

Frequency	Band assignment	Chemical species responsible
~ 3350	O-H stretch[101, 109]	Ethanol, water, Si-OH of silanols
~ 3000-2800	C-H stretch[101]	Ethanol, TEOS and surfactant
~ 1640	H-O-H bending[109]	Molecular water
~ 1440-1320	Various CH_2 and CH_3 vibrations	Ethanol, TEOS
~ 1168	CH_3 rock	TEOS[101, 110]
~ 1086	C-O asymmetric/C-C stretch[101]	TEOS[85], Ethanol[101]
~ 1043	C-O stretch, C-C	Ethanol[101]
~ 960	Si-OH[108, 109] stretch	Silanols
~ 879	C-C/C-O stretch[101, 112]	Ethanol
~ 802	Si-O symmetric stretch[102] / CH_2, CH_3 rock[110, 112, 113]	Siloxane bonds, Ethanol
~ 790	C-O symmetric strecth[111]	TEOS[111]
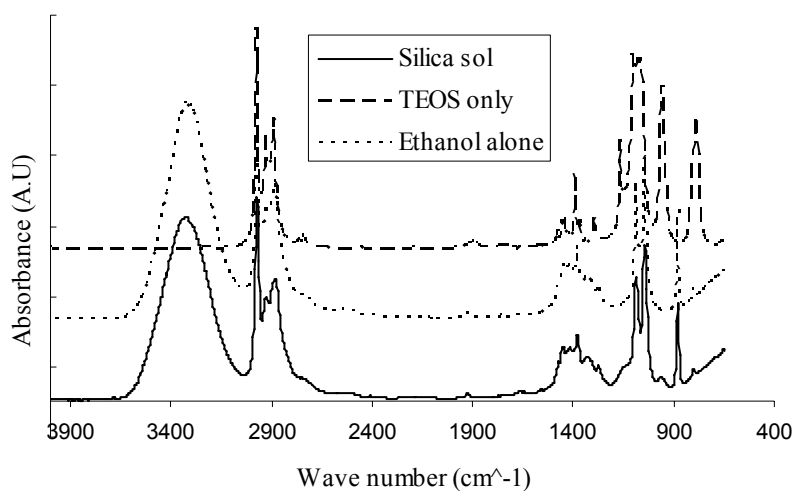
Figure 2.1. Typical IR spectrum of silica sol just before dip coating Si wafers for a P123-containig sol. Also included are FTIR spectra of pure TEOS and ethanol
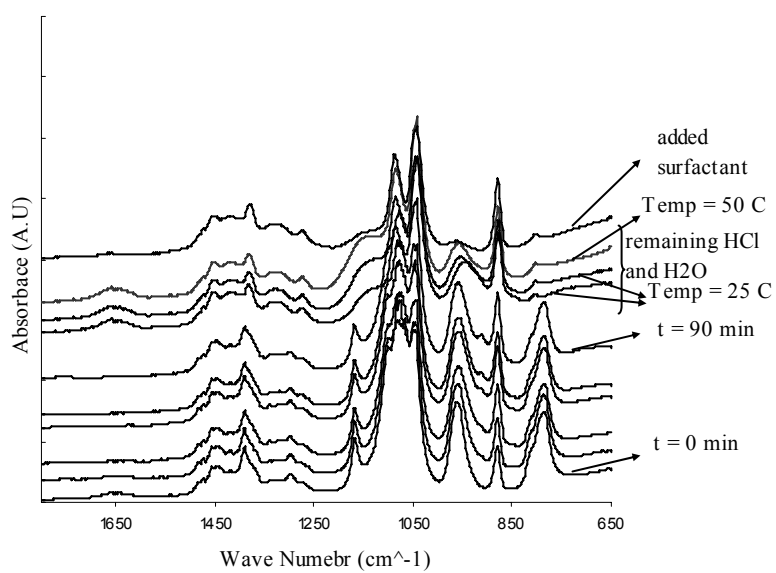
Figure 2.2. FTIR history of P123-based sol at different times during the synthesis. The age of the sol increases from bottom to top, and spectra are included during the first 90 minutes at 70 C, after adding additional HCl and H2O (25 C for 15 min and 50 C for 15 min), and after adding surfactant
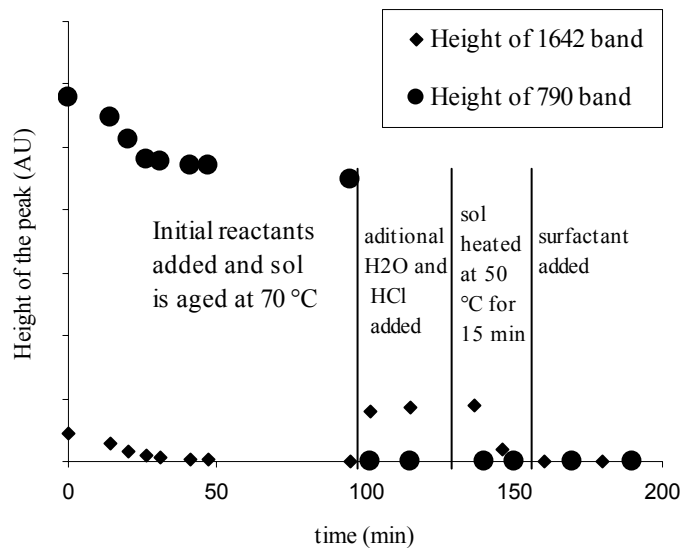
Figure 2.3. Height of the water band (1642 cm-1) and TEOS band (790 cm-1) at different stages during the sol aging time
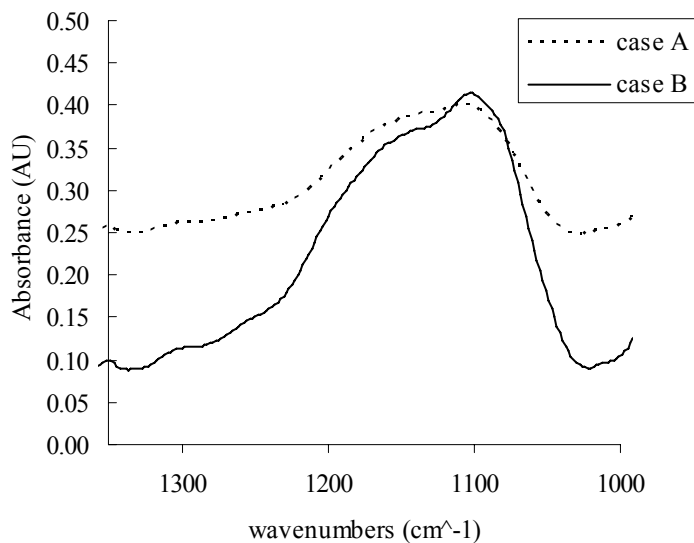
Figure 2.4. FT-IR spectra of silica films 1 min after deposition for two cases, one in which the sol is prepared by HCl and H_2O in two stages (case A) and a second in which the sol is prepared by adding all of the required H_2O and HCl in one stages (case B)
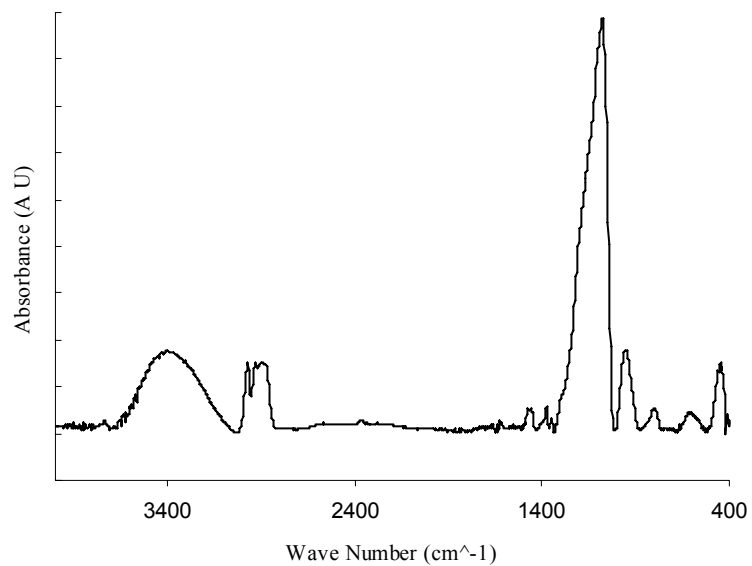
Figure 2.5. IR spectra of a calcined P123-templated silica film coated onto a Si wafer.
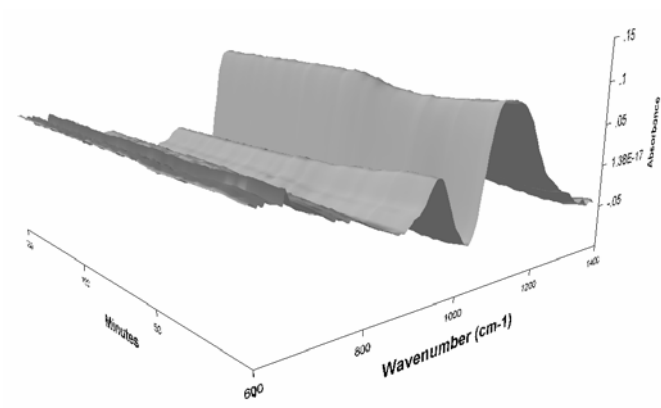
(a)
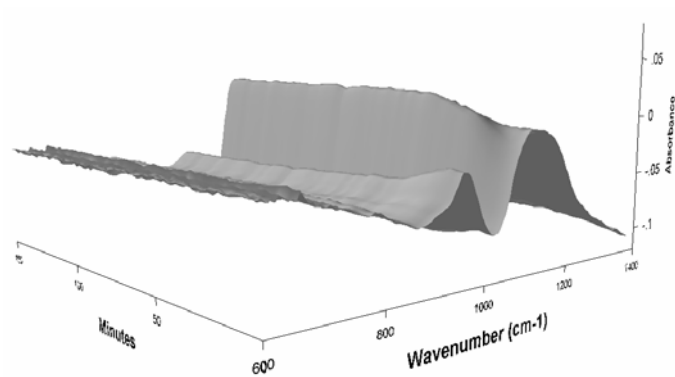
(b)
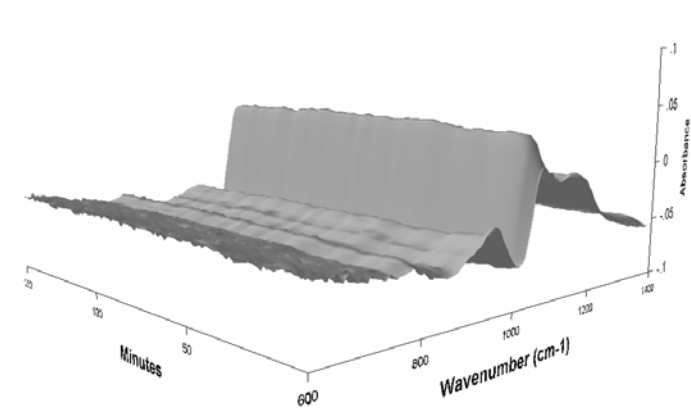
(c)

Figure 2.6. Time-dependent spectra of silica films collected between 1 min after coating and 150 min aged in a 95% RH environment and with (a) P123, (b) Brij-56, or (c) CTAB as the surfactant.
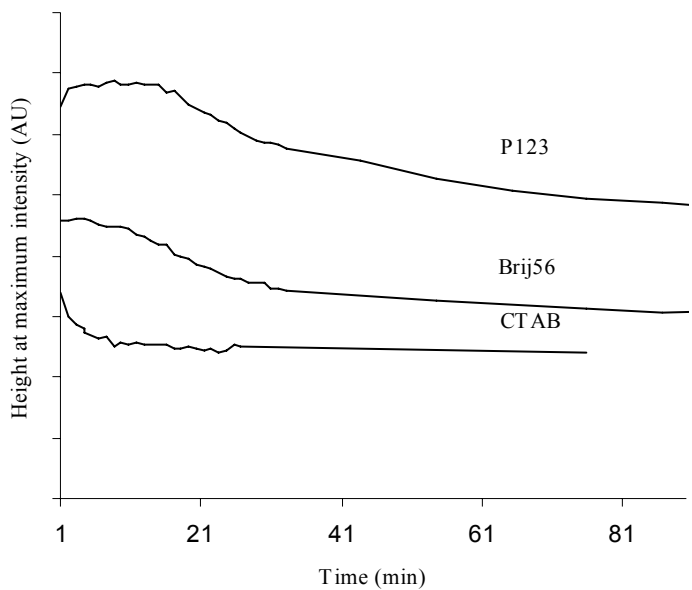
Figure 2.7. Height of the silanol band near ~960 cm-1 vs. time for films containing each of the three surfactants and aged at 95% RH.
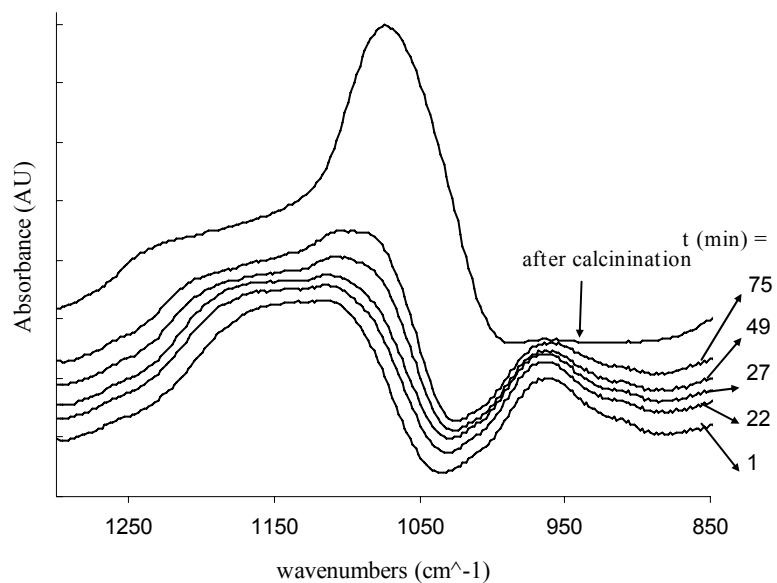
Figure 2.8. FTIR spectra of the P123-templated silica films aged at 95% RH as a function of time elapsed after deposition
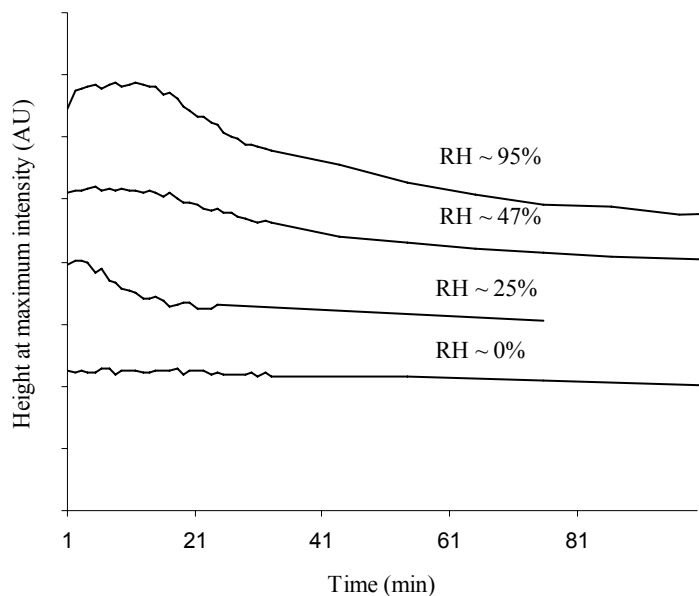
Figure 2.9. Height of the silanol band near ~960 cm-1 vs. time for P123 templated silca films cured in environments of different relative humidity
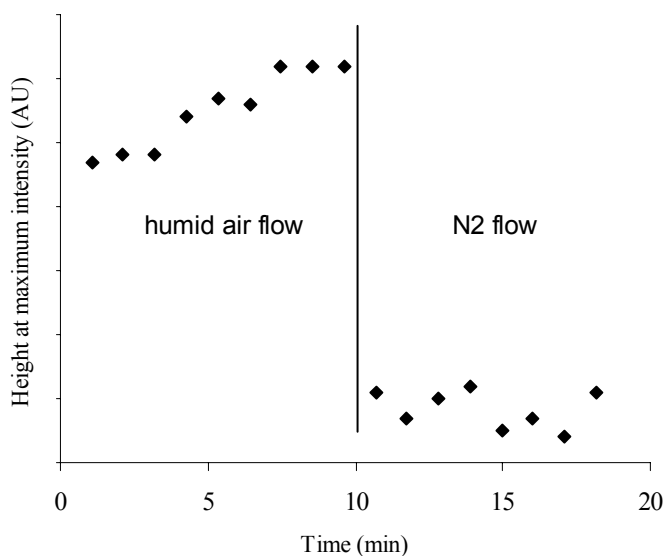
Figure 2.10. Height of the silanol band near ~960 cm-1 vs. time for P123 templated silca films cured in environments of different relative humidity. After 9 min the environment was changed from completely humid to completely dry by flowing N_2 through the gas cell.
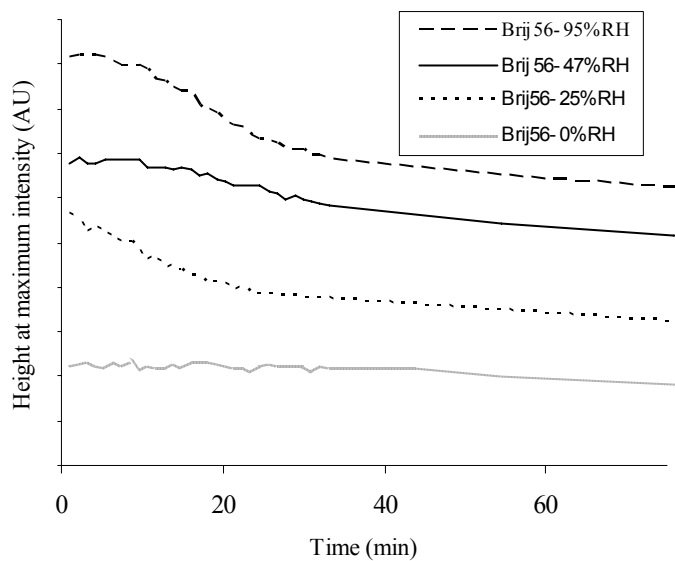
(a)
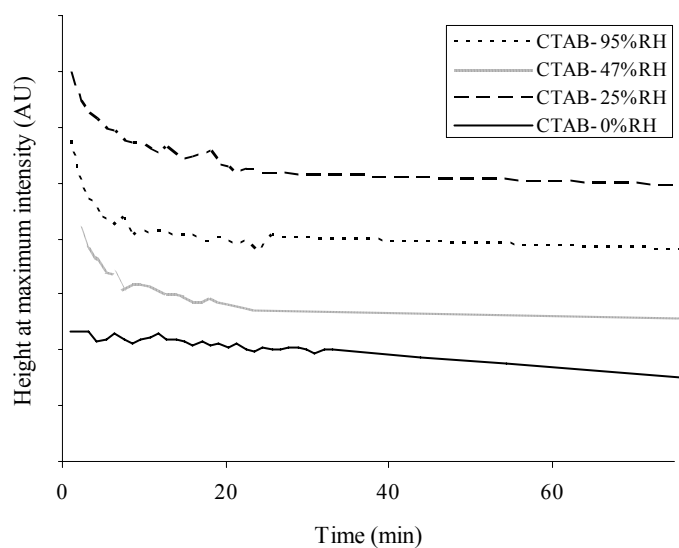
(b)

Figure 2.11. Height of the silanol band near ~960 cm-1 vs. time for brij 56 templated silca films (a) and CTAB templated films (b) cured in environments of different relative humidity.

Copyright © Venkat Rao Koganti 2006

Chapter 3 Lattice Monte Carlo Simulations of Confinement Effects on Lyotropic Surfactant Liquid Crystals

3.1.   Introduction

When present in solvents that show a strong preference for their head or tail, surfactants self assemble to avoid unfavorable solvent interactions. This results in a variety structures like spherical micelles, cylindrical micelles, vesicles etc. When the concentration of the surfactants exceeds a certail threshhold, these self assembled aggregates order themselves into liquid crystalline phases. Several 1, 2 and 3 dimensional liquid crystalline mesophases are known today.[118-121] In 1992, researchers at Mobil Corporation combined this idea of surfactant mesophases with sol-gel chemistry of inorganic precursors and synthesized mesoporous aluminosilicates (M41S materials) with pores sizes between 2 and 100 nm using the surfactant meosphases as templates.[59, 122] Ordered materials with various pores geometries (HCP cylindrical channels, lamellar layers, cubic interconnected channels, etc.) have been synthesized using the corresponding surfactant mesophase as a template.[123-125]

Several years after the initial discovery of surfactant-templated mesoporous silicates, Brinker and coworkers successfully synthesized surfactant-templated materials in thin film and particle morphologies using Evaporation Induced Self Assembly (EISA).[8, 64] In this process, a sol containing surfactant (concentration well below CMC), inorganic precursor, water, acid and solvent are spray-dried or dip coated on to a substrate. Evaporation of the volatile components drives the self assembly of the structure directing agents resulting in ordered structures on a time scale on the order of seconds. Since the initial reports from Brinker's group, this process has been used to synthesize novel materials for several applications. Rapid evaporation of the solvent (usually ethanol), water and acid present in the system leaves behind hydrolyzed inorganic precursors condensing around the surfactant mesophases. There have been several analogies between this system (hydrolyzed inorganic precursors and surfactant mesophases) and surfactant molecules in water which encourages researchers to use the surfactant phase diagrams as a basis to synthesize ordered materials.[126-129] In both these systems the surfactant is present in a polar environment and the mesophase it forms depends on the concentration of the surfactant in the polar environment (inorganic precursors or water) along with many other experimental conditions like temperature, humidity of the environment etc. Using this analogy several surfactant mesophases in water have been translated into corresponding pore geometries in inorganic materials. Hence simulation of surfactant phase behavior in solvents is directly related to the EISA process. In this chapter we study the effect of different kinds of surfaces (hydrophilic, hydrophobic and neutral) on the orientation of the HCP mesophase. We also

examine the effects of different confinement geometries (slit, cylindrical and spherical cavities) on the HCP phase. These geometries are relevant to EISA films, wires, and particles, respectively.

Many recent experimental reports in the area of mesoporous inorganic films have focused on synthesizing these materials inside the larger pores of aligned substrates.[41-43, 130] A major motivation for these works has been to synthesize new materials with controlled orientation of the anisotropic mesophases. Favorable interactions between the surfactant molecules and substrate surface align anisotropic mesophases parallel to the surface.[8, 64] Recently we have reported orthogonally aligned cylindrical mesophase when it is confined between two chemically neutral surfaces (to be discussed in Chapter 4).[50] Also there are several reports of synthesizing mesoporous silica wires inside the pores of anodized alumina substrates to obtain accessible cylindrical pores whose dimensions are less than 10 nm.[41-43, 130] However, a wide variety of novel structures can also be found, such as arrays of concentric ring-shaped pores, intertwined helices, and concentric tubes. In light of these experimental works, the present simulation results are designed to help us understand the effect of confinement on the orientation of the HCP mesophase, leading to the synthesis of novel materials.

Monte Carlo (MC) simulation of surfactant mesophases has been a subject of research for a long time. Rajagopalan[131] and Karaborni and Smit[132] give good reviews of simulations of self-assembling systems. Larson pioneered the simulations of amphiphile-oil-water systems and amphiphilic phases to develop phase diagrams for symmetric and asymmetric surfactants molecules.[133-141] Panagiotopoulos et. al have also contributed to this area through their simulations of surfactant mesophases. They have used lattice monte carlo simulations to understand self-assembly in surfactant and protein solutions,[142] micellization properties and phase behavior of surfactant-oil-water system,[143] and also self-assembly in supercritical solvents.[144] Using MC simulations they proposed a mechanism for shear-induced alignment of micelles.[145] More recently using grand canonical ensemble MC simulations they have studied the effect of chain stiffness on the micellization behavior of model H4T4 surfactant chains[146] and also micellization in model ionic surfactants.[147]

Several other research groups have been involved in this area of simulation of surfactant mesophases. MC simulations have lead to the understanding of thermodynamics of aggregation in amphiphile-solvent systems.[148, 149] They have also been used to understand the properties of surfactant-solvent-inorganic oxide systems simulating the synthesis of M41S type materials.[150, 151] Different silica structures were observed in these simulations depending on the overall concentration of the system[150] and also the inorganic oxide-surfactant interactions were found to be stronger than the solvent-surfactant interactions regardless of the inorganic oxide-solvent

miscibility.[151] MC simulations of model non-ionic surfactants led to finding the parameters at which sphere to rod transitions occur in surfactant micelles in both symmetric and assymmetric surfactants,[152] calculation of Gibbs free energies for the micellization process from the micelle size distribution,[153] and also self assembly at hydrophilic surface.[154] On a hydrophilic surface, surfactants tend to self assemble at a concentration below CMC, and increased interactions between surfactants and the hydrophilic surfaces lead to formation of prolate structures aligning themselves parallel to the hydrophilic surface.[154] MC studies of self assembly of surfactant aggregates have been used to comprehend the cluster size distributions and excess chemical potentials,[155] formation of stable curved membranes and metastable vesicles,[156] temperature-composition phase diagrams for a dilute surfactant model solutions,[157] and also coexistence of two lamellar liquid crystalline phases.[158]

Orienting anisotropic mesophases has been an active research area in both surfactant templated materials and block copolymers. There has been work reported in the block copolymer literature to see the effect of surface chemistry on the orientation of anisotropic mesophases. Simulations have shown that one can align anisotropic mesophases perpendicular to the substrates by eliminating preferential interactions between the blocks of the amphiphile and the substrate. Both self-consistent field theory and Monte Carlo simulations have suggested that AB block copolymer lamellar mesophases should align parallel to walls that interact with a strong preference for either block.[159-162] Neutral walls, which have no strong preference for either block, align the lamellae perpendicular to the walls.[160-162] A more recent density functional theory study confirms the same trend for asymmetric block copolymers which form HCP mesophases.[163]

Although many of these studies aim at understanding self assembling surfactant systems, only a few of these studies attempt to understand the effect of external forces on the orientation of mesophases. The study by Panagiotopoulos et al. discussed above discusses the effect of external shear forces in aligning the HCP mesophase in a direction parallel to the shear direction.[145] Other important studies that deal with surface effects on orientation of HCP mesophase are by Rankin et. al.[164] and Stucky et. al.[43] Using MC simulations Rankin et. al. understood the effect of the surface-surfactant interactions on the orientation of HCP mesophase. They observed that neutral walls which do not have any preferential interactions with head or tail of the surfactant molecules align the HCP mesophases perpendicular them.[164] Stucky et. al. have used Self Consistent Field Theory calculations to see the effect of cylindrical confinement of HCP mesophase. In the presence of hydrophilic cylindrical walls as the radius of the cylindrical cavity increases they observe a transition from spherical micelles to straight cylinders to helices.[43]

In this work we continue these efforts in the direction of understanding surface confinement using slit shaped, cylindrical and spherical confinement of the HCP mesophase. We will observe

the effect of the interactions between the wall and the surfactant molecules on the orientation of the HCP mesophase in each of these geometries for a specific model lyotropic liquid crystal phase.

3.2.   Simulation Method

We performed coarse grained lattice MC simulations of binary mixtures of surfactant chains and one solvent on a simple cubic lattice using the Metropolis algorithm.[165] We used a canonical ensemble with fixed N, V, and T. The lattice was fully occupied so that the sites unoccupied by the amphiphile beads are occupied by the solvent beads (which we will call "water" to signify a polar solvent) by swapping places with amphiphile beads. Contributions from each of the 26 neighbors to a lattice were taken into account by pair wise addition of nearest (along the edge), second nearest (along face diagonal) and third nearest (along body diagonal) neighbor interactions. In other words, a square well potential was used.   Dimensionless pairwise interactions (scaled by $|E_{ww}|$, the water-water interaction energy) were calculated as $E^* = -1$ for like components (water-water, water-head, and tail-tail pairs) and $E^* = +1$ for dissimilar components (water-oil, head-oil, head-tail, and water-tail pairs) for $\sigma \leq r \leq 3^{1/2}\sigma$, where r is the distance between two beads and σ is the lattice spacing. The total energy was assumed to be pairwise additive.

The surfactants were composed of four head and four tail beads (H_4T_4) organzied in linear chains of four consecutive head units attached to four conceccutive tail units. The bonds between beads were modeled with a square potential in which the energy was 0 for a bond length of $\sigma \leq l \leq 3^{1/2}\sigma$ and ∞ otherwise. The chains were moved by kink, reptation,[140] biased regrowth and biased translation trial moves.[166] The probabilities of the trial moves were chosen as 50% kink, 20% reptation, 20% biased regrowth and 10% biased translation to give reasonable acceptance ratios. The system consisted of 60 volume % surfactant and 40 volume % water. With this ratio, Larson obtained a HCP mesophase for the H_4T_4 surfactant system at a dimensionless temperature T^* $(=k_BT/|E_{ww}|$ where k_B is the Boltzmann constant) of 13.[138] We have used both Metropolis[165] (for kink and reptation moves) and Rosenbluth[166] (for regrowth moves) sampling techniques in this algorithm. To ensure a correct approach to equilibrium, we began each simulation with a solution of this concentration at a temperature well above the order-disorder transition (T^*=50) to randomize the distribution of species, and slowly lowered the temperature in a series of steps to the final temperature of $T^* = 13$. After reaching this temperature the systems were equilibrated for over 10^9 individual MC steps and the energies and bead densities densities were averaged over several million more.

Periodic periodic boundary conditions were employed in all simulations to mimic bulk phases. To simulate an unconfined phase, periodic boundaries were used in all 3 directions. For slit cavities, impenetrable walls were introduced in one direction (the x-direction in our case). For cylinder and spherical cavities, the simulation was filled with blocked wall sites as appropriate to form the desired geometry. The pairwise interactions between each wall site and each component were modeled with square-well potentials. For hydrophilic walls, interactions with polar (head or water) beads had an energy of E* = -10 for $\sigma \leq r \leq 3^{1/2}\sigma$ and 0 for $r > 3^{1/2}\sigma$ while interactions with non-polar (tail) beads had an energy of E* = +10 for $\sigma \leq r \leq 3^{1/2}\sigma$ and 0 for $r > 3^{1/2}\sigma$. For hydrophilic walls, the form of the potential was the same, but the signs of the interactions were reversed. For neutral walls, the energy was modeled as E* = 0 regardless of the bead identity or distance to the wall.

3.3.   Results and Discussion

Using the above mentioned algorithms we have performed MC simulations of surfactant mesophases when present in confined space. In this work we use water as solvent and the concentration of surfactant and the temperature was chosen based on the published phase diagram of Larson.[138] The results of our simulations of the bulk H_4T_4 surfactant-water system are similar to the observations of Larson.[138] Using 60 volume % of surfactant we obtained a 2D HCP mesophase. Fig. 3.1 shows a 3D contour plot of the tail densities of the surfactants in a 30 * 30 * 30 simulation box without any walls present. We can clearly see well ordered defect free HCP cylinders. The HCP lattice dimensions are calculated using the Radial Distribution Function (RDF) of the tail site densities and will be discussed in the next sub-section. Fig. 3.2 shows a representative plot of the decrease in the total energy of the system as a function of the MC steps for a particular simulation with walls present. We can see that as the simulation proceeds for each temperature change, the energy of the system decreases and attains an equilibrium value at a given temperature. Once equilibrium is reached the temperature is then decreased further until the final dimensionless temperature of 13 is reached. In the example shown in Fig. 3.2, additional jumps to higher T* (16) and back to T*=13 are used to help to anneal the system more quickly. After these annealing steps, the system is equilibrated over an additional 10^9 MC steps and then the thermodynamic properties and densities are averaged over another 10^9 steps. For the particular example in Fig. 3.2, the final dimensionless energy per lattice site is -11.4, but for the bulk HCP phase, the dimensionless bulk energy, E_{bulk} per lattice site is ~ -8.6. The dependence of energy on wall structure and chemistry will be discussed more below.

41

Annealing the system by heating it suddenly to a higher temperature and back down to the target temperature not only accelerates the approach to the equilibrium energy, but also avoids the systems getting trapped in an intermediate metastable defective state. Fig. 3.3 shows the simulated tail densities of 2D HCP mesophase in hydrophilic slit shaped walls. The walls are present in the x- direction of a $65 \times 30 \times 30$ simulation box. Fig. 3.3a shows the results when there are no annealing steps used after the temperature reaches T*=13, which results in a distorted HCP mesophase. Fig. 3.3b shows a defect free HCP mesophase when the temperature of the system is increased from T* = 13 to T* = 16 and then cooled to T* = 13 and then equilibrated. 10^6 MC equilibration and 10^6 MC averaging steps were used at each temperature (T* = 13 and T* = 16) Using a combination of gradual temperature decreases and annealing steps, we are able to simulate defect free HCP mesophase in the majority of cases – until the box size becomes so large that defects can not anneal out within a reasonable number of MC steps. This technique was employed as needed in all the simulations that will be discussed below.

3.3.1. Radial Distribution Function (RDF)

The Radial Distribution Function (RDF) of tail site densities was calculated to obtain an estimate for the HCP lattice spacing, *a*. An algorithm was written to obtain RDF, g(r/σ) by using the density values of tail beads obtained from the MC simulation. The average density at lattice site of each species, $<\rho>_i$, at each lattice site *i* is determined by the simulation. From these values, g(r/σ) is computed using the following equation:

$$g(r/\sigma) = \frac{\sum\limits_{i=1}^{N_{sites}} \sum\limits_{j=1}^{N_{sites}} \langle\rho\rangle_i \langle\rho\rangle_j \delta_{ij}}{\langle\rho\rangle^2 \sum\limits_{i=1}^{N_{sites}} \sum\limits_{j=1}^{N_{sites}} \delta_{ij}}$$

where δ_{ij} is a function that determines if the distance from site *i* to site *j* is within a certain distance (the sizes of bins used to plot the RDF) from a specific value of r/σ, and <ρ> is the overall average density of that species.

The same algorithm was used to obtain the RDF of tail site densities both in the presence and absence of walls. Fig. 3.4 plots the RDFs of tail site densities. Results for slit shaped, cylindrical and spherical walls are presented. For all the cases we see the first peak around the same value of r/σ = 13 ± 0.5. This is the nearest-neighbor distance for micelles, also known as the unit cell parameter of the HCP phase, a = 13 ± 0.5 σ. From the geometry of the HCP phase, the d-spacing is calculated to be d_{100} = 11.3 ± 0.4 σ. Although similar in terms of lattice spacing, there are some differences between these curves. The higher order reflections representing the second

42

nearest neighbor distance and higher, are pronounced when the simulation box has walls compared to the case when there are no walls. In the presence of the walls, surfactant molecules are better ordered resulting in sharper interfaces and higher order peaks in RDFs

RDFs of tail densities do not have a base line which has a zero slope when the simulation box has cylindrical or spherical walls. This is due to the superposition of a factor for the shape of the cavity on top of the RDF (which decays to zero in some cases because of the finite dimensions of the cavity). Using this RDF algorithm we were able to observe the temperature for the onset of ordered phase formation. At each temperature during the temperature progression, we have obtained RDF of tail densities and we find that the first peak in the RDF appears at a dimensionless temperature of around 18. These RDFs are plotted in fig. 3.5. This plot shows that at around $T^* = 18$ we start seeing the formation of ordered phases, consistent with the results of Larson.[135] From these studies of the overall structure of the HCP mesophase in various cavities, we infer that confinement has relatively little effect on the ordering of micelles in the mesophase. Below, we examine more closely how confinement affects the orientation and structure of the HCP mesophase.

3.3.2. Slit shaped cavities

Fig. 3.6 shows tail densities of simulated HCP mesophase in slit shaped cavities with different wall interactions. Fig 3.6a and 3.6b show the HCP phase confined between hydrophilic and hydrophobic walls, respectively. The walls are present in the 'x' direction on both the faces of the simulation box. We can see the HCP cylinders aligning in a direction parallel to these walls with their (100) plane aligning parallel to the wall. These observations are similar to the results obtained by Rankin et. al.[164] where they observe parallel alignment of the HCP mesophase on hydrophillic and hydrphobic surfaces. Hydrophobic walls have a monolayer of surfactant present on the walls with their tails pointing towards the walls. In the case of neutral walls the cylinders aligned perpendicular to the walls, as illustrated in Fig. 3.6c. The micelles are not perfectly orthogonal to the wall, but may be tilted at an angle with respect to 90° from the wall surface. As the size of the box increases, we begin to see mixed orientations at distances far away from the neutral walls. This is understandable because the effect of the wall propagates only a finite distance away from it. Studies on block copolymer films have shown that there exists a critical thickness above which block copolymer films on neutral surfaces have the cylindrical channels with mixed orientations.[48, 167]

Using MC simulation we also calculated the equilibrium energy of the system. The energy per lattice site of the system in the presence of walls deviated from the bulk energy due to the interfacial energy for contact between the mesophase and the wall. Interactions between the wall

sites and the molecular components were made 10 times stronger in magnitude compared to the interactions between the ordinary sites to show the influence of the walls clearly (for instance, for a hydrophilic wall, $E^*_{water,\ wall}$ = -10, $E^*_{head,\ wall}$ = -10, and $E^*_{tail,\ wall}$ = 10). For neutral walls interactions between the molecular components and wall sites were made equal to 0. The presence of a bead near a wall site means the absence of ordinary neighbor sites which were once occupied by the components of the system which had an interaction energy E of ±1 depending on the nature of the interactions. This change in interaction energy (in the presence of hydrophilic or hydrophobic walls) results in a different value for the energy of the system in presence of hydrophilic or hydrophobic walls compared to the bulk mesophase. Fig. 3.7 plots the energy per lattice site of the mesophase volume as a function of the distance between the walls for hydrophilic (fig. 3.7a), hydrophobic (fig. 3.7b) and neutral (fig. 3.7c) walls. Also plotted in the same figure are the expectation curves for the energies calculated from the following equation for a slit shaped pore:

$$E = 2\frac{\gamma}{\Delta x} + E_{bulk}$$

For hydrophilic or hydrophobic walls, we can assume that the wall will attract "like" beads, so the surface energy per bead is given by the cost of taking a bead surrounded with other "like" molecular beads to the wall surface. This means replacing nine molecular beads with wall sites to give an interfacial energy of γ = 9*(-10+1) = -81 for hydrophilic or hydrophobic walls. For neutral walls, we presume that any type of bead has 9 favorable interactions replaced with neutral interactions to give γ = 9*(0+1) = +9. In this expression, E_{bulk} is the dimensionless bulk energy of the system and Δx is the distance between the walls. The data obtained closely follow the expectation curve and as the distance between the walls increases, the energy increases (for hydrophilic / hydrophobic walls) or decreases (for neutral walls), approaching the bulk energy value (-8.6). As the distance between the walls increases, molecular components away from the wall have interactions closer in nature to interactions in the bulk phase and hence the total energy of the system approaches the bulk energy as Δx increases.

In the case of hydrophilic walls, there are jumps in the energy values at regular intervals of Δx. As the box size increases the number of amphiphilic molecules present in the box increases. These added surfactant molecules tend to fit into the existing cylindrical channels thus increasing the radius (or decreasing the curvature) of the channels. Although this is energetically favorable there is an entropic penalty as we are tending to form a phase with lesser curvature than is optimal at this concentration of the surfactant. As the box size increases beyond a certain value (~ integral multiple of d_{100}) there is a sudden increase in the number of cylindrical layers that fit into the box to compensate for the entropy of the system. For a small number of layers (3), the

energy deviation is negative, which is at first surprising, but for this small number of layers, the micelles grow and deformed as the layer expands, and this allows the internal energy of the system to decrease. At the transision to 4 layers, the energy jumps above the continuum curve because the mesophase is slightly compressed. More jumps are observed corresponding to increases in the number of layers to 5 and to 6. The number of layers of cylinders is marked in Fig. 3.7. For each fixed number of layers, the energy follows a linear trend, where the slope of the line decreases as the number of layers increases. This is because the compressibility of the cylinders decreases as the number of layers increases. There are alternative ways to compensate for compression or tension with a larger number of layers, such as the appearance of defects in which entire planes of micelles are twisted relative to their neighbors. One of these defects is illustrated in Fig. 3.6b. The occurrence of these defects increases towards the upper gap size within each region corresponding to a fixed number of layers.

In case of hydrophobic walls also there is an increase in the number of layers of cylindrical channels as the gap distance increases. However, this increase in the number of layers is not accompanied by jumps in the energy. Hydrophobic walls have a monolayer of surfactant molecules attached to them before the self assembly starts. This "soft" monolayer is always present, and allows the added surfactant molecules to expand the mesophase continuously as the box size increases, thus allowing the energy to increase smoothly even when there is a jump in the number of layers. When the walls are neutral, the deviation from the bulk energy of the system is less than the deviation for the hydrophilic and hydrophobic walls because the interaction between the wall and the surfactant molecules is small. The energy continuously approaches the bulk value as the gap size increases because no tension or compression of layers is experienced in orthogonally oriented channels.

We have also studied the effects of the box dimensions in the y or z direction of mesophases confined in slit-shaped cavities (keeping the distance between the walls in the x direction constant) on the orientation of the HCP mesophase. Fig. 3.8 shows the orientation of the cylinders in different sized boxes with hydrophilic walls present in the x direction. In all of these cases, the X and Y dimensions are kept constant at 30 lattice units. In the Z direction the box dimension is increased from 14 to 56. A few selected figures are shown in Fig. 3.8. As the Z dimension increases there is a change in the orientation of the cylindrical channels. Fig. 3.9 plots the acute angle of inclination between the cylindrical channels and the x-axis as a function of the box dimension in the Z direction. Also shown is the number of layers of cylinders packed into the box in the z direction. As the box size increases the increased surfactant chains tend to get incorporated into the existing cylinders and to accommodate these additional surfactants the cylinders tilt so as to increase their length in the box. After reaching a certain point there is an

increase in the number of layers of cylinders in the z direction. At this point the angle of inclination once again drops to a smaller value. Changes in the number of cylinders occur at box sizes that approximately multiples of twice the (100) d spacing (~ 23). This is because it is energetically favorable to have integral numbers of cylindrical layers, and hence the increase in the number of layers of cylinders occurs when the z dimension of box increases by at least one lattice unit. Also the number of cylindrical layers increases in multiples of 2 to satisfy the periodic boundary conditions.

3.3.3.   Cylindrical cavities

As discussed earlier we have simulated the HCP mesophase in cylindrical cavities. Simulations with cylindrical walls were performed with hydrophilic and neutral walls only. Hydrophobic walls in slit cavities are similar to hydrophilic walls except for a monolayer of surfactant present on the walls, so we presume that the behavior in cylindrical pores will be similar for hydrophobic and hydrophilic walls. In all these simulations that will be discussed, the axis of the cylindrical cavity is in the Z direction. Simulated HCP meosphase in a neutral cylindrical cavity is shown in Fig. 3.10. Similar to the slit walls the cylinders are oriented orthogonal to the neutral walls even in cylindrical cavities. The direction of the orientation is arbitrary and appears to be determined randomly based on how the micelles nucleate the HCP phase. The same type of orthogonal alignment is observed regardless of the cylindrical cavity diameter or length. More interesting results are observed when the walls are hydrophilic and we present here the results of hydrophilic cylindrical walls in greater detail.

Fig. 3.11 shows selected simulated tail density contour plots of HCP mesophase in cylindrical cavities of different sizes. A whole range of structures are seen as a function of box size. As the radius of the cylindrical cavity increases, the number of layers increase and cylindrical mesophase transforms from a uniform wire (Fig. 3.11a) to a tube with perforations (Fig. 3.11b, 3.11c) to a wire surrounded by perforated tubes (Fig. 3.11d) to helices (Figs. 3.11e to 3.11i). Cavities of smaller radii (high curvature) result in perforated annuli. In order for helical micelles form, the radius of the cavity has to be above a critical value. We start to see defective helices when the diameter of the cavity is 36 (Fig. 3.11e) although there are still some defects observed in the helices. Bigger boxes result in more perfect helices (figs. 3.11f to 3.11i). Larger cavities have smaller curvature and hence the cylinders can align themselves to form uniform helices. The main purpose of using cylindrical cavities to grow mesoporous materials inside them is to obtain HCP mesopohase oriented parallel to the walls of the cylindrical cavity, which means that the HCP phase is oriented orthogonal to the plane of the film (such as an anodized alumina film). Although one of our objectives was to see the conditions that favor defect free orthogonally

46

aligned cylinders, we were not able to observe this orientation. Perforated and interconnected cylinders were the closest we could obtain (fig 3.11b-d) consistent with the observations by Stucky et. al. using self consistent field calculations.[43]

We have also observed height dependence of the uniformity of the helices formed. Fig. 3.12 shows the tail density contour plots of simulated HCP mesophase in hydrophilic cylindrical pores with diameter 54 units and varying height. Once again we see that large boxes allow perfect helices to form. We can also say that defect free helices are formed if the height of the cylindrical cavity is approximately a multiple of the lattice spacing (a ~ 13 in this study). Box heights of 26 (Fig. 3.12b) and 36 (Fig. 3.12e) result in perfect helices compared to the cases where the heights are 16 (Fig. 3.12a), 30 (Fig. 3.12c) and 34 (Fig. 3.12d). This observation can be explained as follows: When the box height is close to being a multiple of lattice spacing, all of the surfactant molecules occupy the cylindrical channels completely and result in a perfect helices with integral number of cylindrical layers in a helix. When the box height deviates significantly from being a multiple of lattice spacing, the mesophase is under strain due to having excess surfactant molecules, thus resulting in defective helices. The results for the helix structure as a function of box size suggest that helices are always preferred for the small boxes that we have been able to simulate. However, if the finite extent of the mesophase is simulated by adding walls at the ends of the channels, concentric ring micelles are formed (not shown) which resemble some of the structures isolated experimentally. We imagine that very long pores or off-lattice simulations of structures in tension may help to simulate the formation of HCP channels aligned along cylindrical cavities, but to do these simulations will require significant advances in the code that we are using.

Fig. 3.13 plots the equilibrium energy of the HCP mesophase as a function of the diameter of the cylindrical cavity. The height (in the Z direction) of the box was kept constant at 16 units in this plot. Also plotted is an expectation curve for the cylindrical cavities. This curve is calculated as follows:

$E = 2\dfrac{\gamma}{R} + E_{bulk}$, where the notation is same as the notation for the slit shaped walls, and R is

the radius of the cylindrical cavity. The value of γ is assumed to be the same as for the slit shaped pores, in spite of the larger curvature of the walls. The number of layers of the cylindrical channels is also indicated on the plot. This is done to draw an analogy between the slit shaped cavities and cylindrical cavities. Similar to the slit shaped pores there is a discrete increase in the number of layers as the cavity diameter increases. A wire is considered as one layer and an annulus is considered to be 2 layers (we will see two layers of cylindrical micelles in an annulus starting from one side of the cavity and moving through the center to the other side). This plot

47

shows that there is a good agreement between the theoretically predicted energy values and actual energy values. Also there exists transition radius where there is a jump in the number of cylindrical layers between two the opposite ends of the diameter of the cylinder. The numbers of layers are marked on the plot. The transitions between the numbers of layers occur when the box size increases by a multiple of the d-spacing (~ 11).

3.3.4. Effect of Spherical Confinement

Similar to cylindrical walls, we have used neutral and hydrophilic walls when simulating the HCP mesophase in spherical cavities. These cavities mimic what might be observed in precipitated droplets of lyotropic liquid crystal or in aerosol particles. Hydrophobic walls behave similar to the hydrophilic walls except for a monolayer of surfactant present on the walls. Fig. 3.14 shows a representative simulation result of a cylindrical mesophase in a spherical cavity of diameter 58 units with neutral walls. We can see the cylindrical micelles oriented normal at the wall-micelle interface. As we go deeper into the spherical cavity, we see merging of the micelles at random points because the system tends to maintain a constant micelle diameter. The orientation of these cylinders depends on the radius of the cavity, but the micelles are always oriented radially towards the walls of the cavity. This type of structure has been found to form in CTAB/silica particles precipitated from ammonia solutions containing a large concentration of ethanol.[168-171]

Hydrophilic spherical cavities results in several interesting structures. Figure 3.15 shows the HCP mesophase present in hydrophilic spherical cavities of different radii. As the radius increases we see a transition from a uniform layer (fig. 3.15a) to perforated structures (fig. 3.15b). Further increase in the radius induces ordered perforations, and finally we also observe cylindrical channels curving along the walls of the cavity. We also see a gradual increase in the number of cylindrical layers between two ends of the diameter of the spherical cavity as the radius increases. Fig 3.16 shows a plot of the equilibrium energy of the HCP mesophase confined in a spherical cavity as a function of the radius of the cavity. Results for both hydrophilic and neutral walls are plotted. Also plotted are the expected energy curves calculated as follows:

$E = 3\dfrac{\gamma}{R} + E_{bulk}$, where the notations are same as the notations for the slit shaped walls, and R is the radius of the cylindrical cavity. The value of γ is also same as the slit shaped pores. The number of layers of the surfactant molecules is also mentioned in the plot. Similar to the slit shaped pores there is a discrete increase in the number of cylindrical layers. A sphere is considered as one layer and an annulus is considered to be 2 layers. This plot shows that there is

a good agreement between the theoretically predicted energy values and actual energy values. Also there are transition radii where there are jumps in the number of layers of surfactant molecules and this transition radius is a multiple of d-spacing, similar to the cylindrical cavity. Unlike slit and cylindrical cavities, the energies of the HCP phase in spherical cavities is always less than the theoretical energy predicted by the equation above. This is because of the high curvature of the spherical cavity which increases the number of interactions of an adsorbed bead with the wall and thus lowers the energy somewhat more than anticipated.

Another trend in the energies is that as the traverse from slit to cylindrical to spherical cavities we see that actual energies calculated by the MC simulation are lower than the continuum model predictions which are given by the equations above. Although we did not quantify this argument this fits into the argument above that curved surfaces result in energies lower than the continuum model predictions.

3.4.   Conclusions

Using MC simulations and conditions similar to those used to study ideal H_4T_4 surfactant phase behavior by Larson, we have obtained 2D HCP mesophase in simulation boxes with periodic boundaries. We have successfully simulated the 2D HCP mesophase in confined environment in slit shaped, cylindrical and spherical cavities. In all these confinements we have used hydrophilic, hydrophobic and neutral walls. Using the Radial Distribution Function (RDF) of the tail site densities we obtained an estimate for the lattice spacing of the HCP mesophase in both unconfined and confined environments. Confined environments show pronounced higher order reflections in the RDF plots, but the dimensions of the associated phase remain almost unchanged due to confinement. Instead, the effects of the confining cavity can primarily be seen in the energetics and the orientation of the mesophase.

In the presence of hydrophilic slit shaped walls the HCP mesophase orients itself in a direction parallel to the wall with (100) plane oriented parallel to the wall. There are always a discrete number of cylindrical layers between the walls. Jumps in layers occur when the distance between the walls is approximately an integral multiple of the 100 d-spacing. Influence of the box size in a direction orthogonal to the direction of the walls has also been measured. Equilibrium energy of the system in the presence of hydrophilic walls is lower than the bulk energy and it approaches the bulk energy value as the box size increases. Neutral slit shaped walls orient the cylinders in a direction orthogonal to the walls, consistent with results obtained by other researchers.[164]

Hydrophilic cylindrical and spherical cavities result in several interesting confinement effects of the HCP mesophase. Hydrophilic cylindrical cavities resulted in a range of structures that

49

include uniform monolayers, perforated cylinders to helices as the diameter of the cavity increased. Bigger boxes resulted in perfect helices. Spherical confinement of the HCP mesophase results in structures similar to the cylindrical confinement that included uniform layers, disordered perforated vesicles, ordered perforated vesicles, and cylindrical channels arranged in layers as the radius of the spherical cavity increased. Neutral walls in cylindrical and spherical cavities resulted in normal alignment of the cylindrical mesophase at the interface similar to the slit shaped cavities. This simulation study has enhanced our understanding of the confinement effects of the cylindrical mesophase and we think has the potential to result in the synthesis of novel mesostructures using surfactant templation.
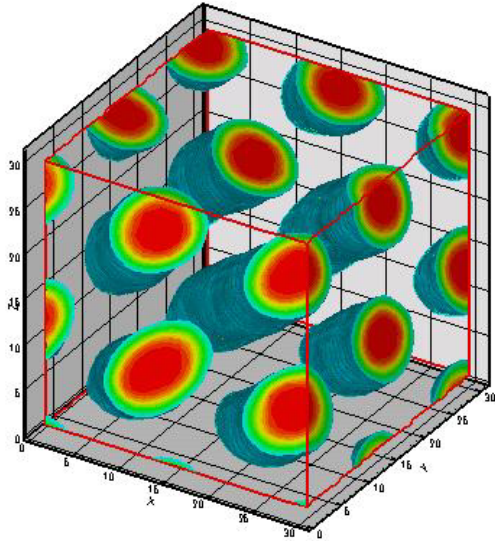
Figure 3.1. Tail densities of HCP mesophase in a 30 * 30 * 30 simulation box
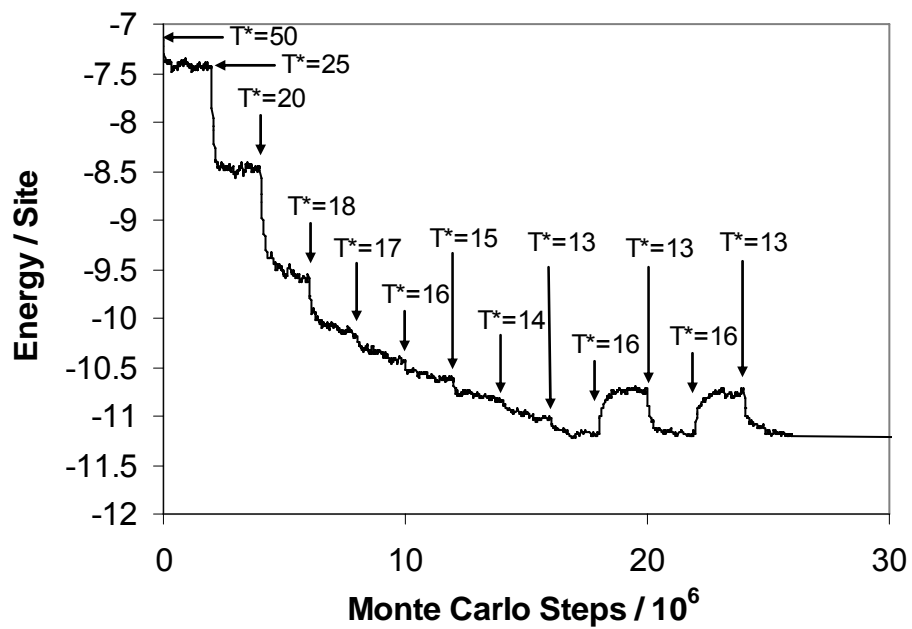
Figure 3.2. Total dimensionless energy per lattice site vs. number of MC steps for a particular simulation with walls present, showing approach to equilibrium under temperature changes.
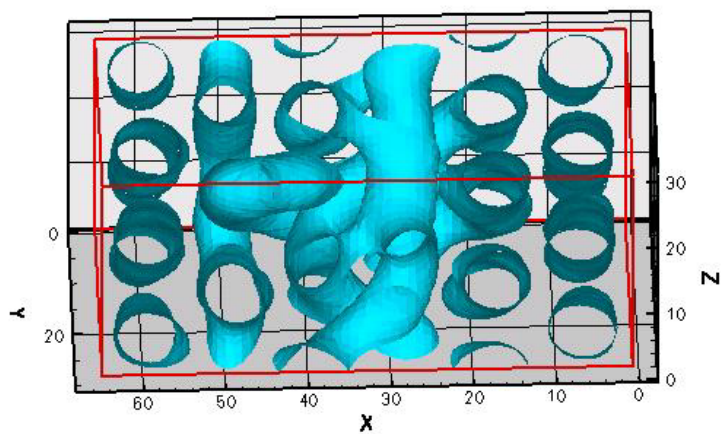
(a)
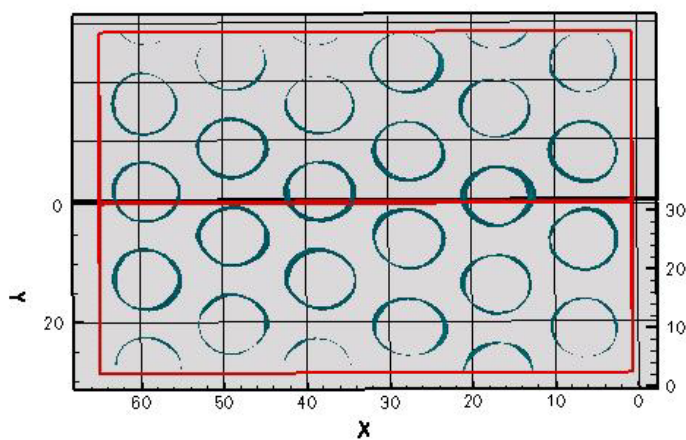
(b)

Figure 3.3. Tail densities in a 65 * 30 * 30 simulation box with hydrophilic walls present in 'x' direction (a) simulated result without annealing and (b) simulated result by annealing the system by increasing T* = 13 to T* = 16 and then cooled to T* = 13 and then equilibrated. 10^6 MC equilibration and 10^6 MC averaging steps were used at each temperature (T* = 13 and T* = 16)
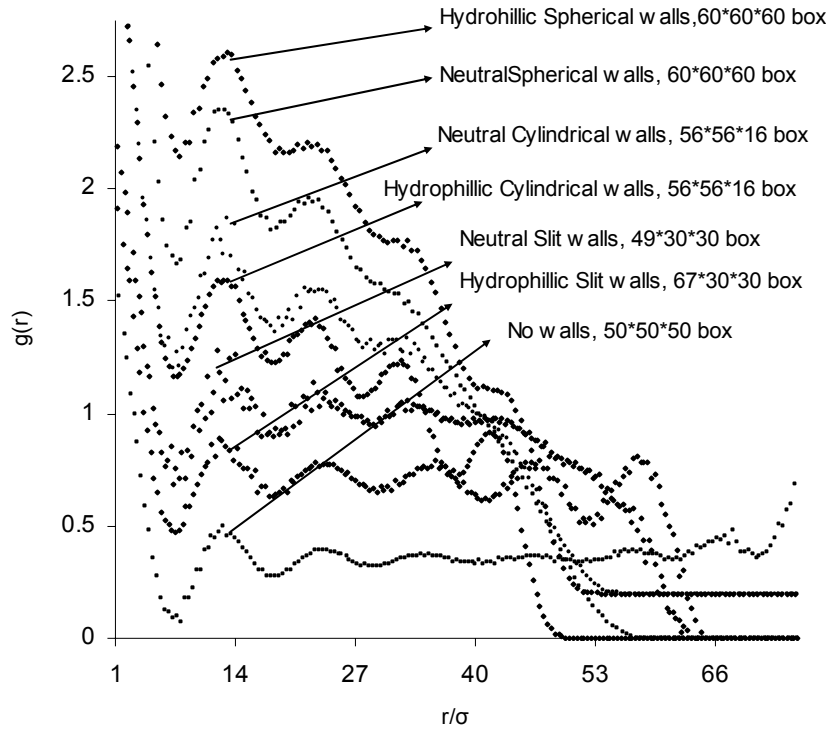
Figure 3.4. Radial Distribution Function (RDF) of simulated tail densities. Box sizes are mentioned in the figure legend
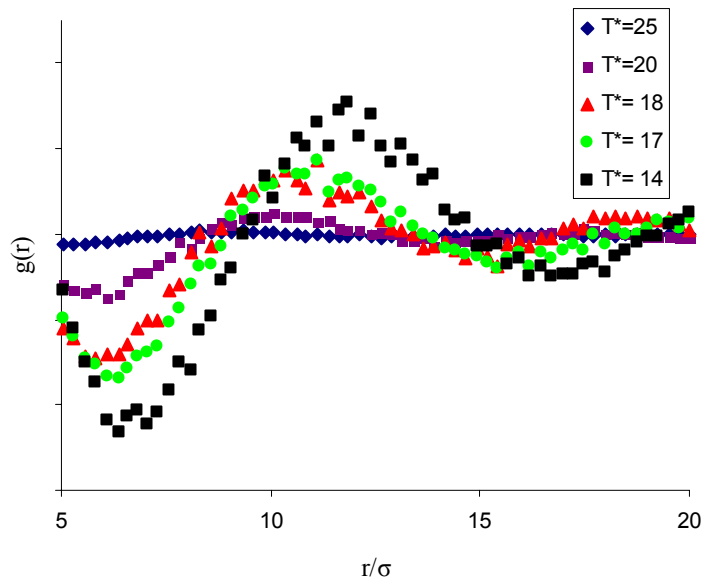
Figure 3.5. Radial Distribution Function (RDF) of simulated tail densities at different dimensionless temperatures. Around T* = 18 we start seeing the appearance of peak.

(a)

(b)

(c)
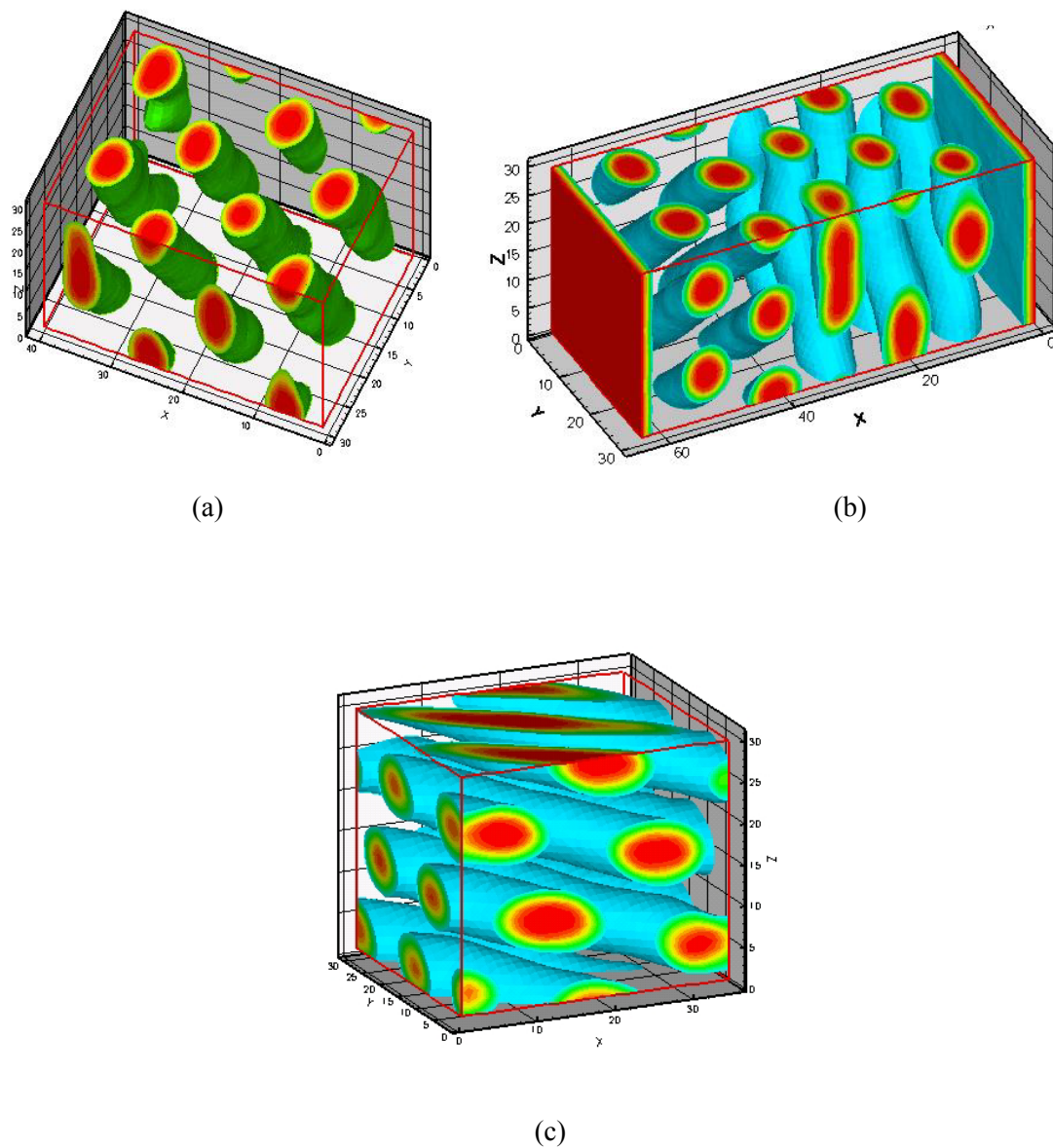
Figure 3.6. Simulated tail density isodensity surfaces for HCP mesophase confine in a slit shaped cavity with walls in the X-direction that are (a) hydrophilic, (b) hydrophobic, or (c) neutral.
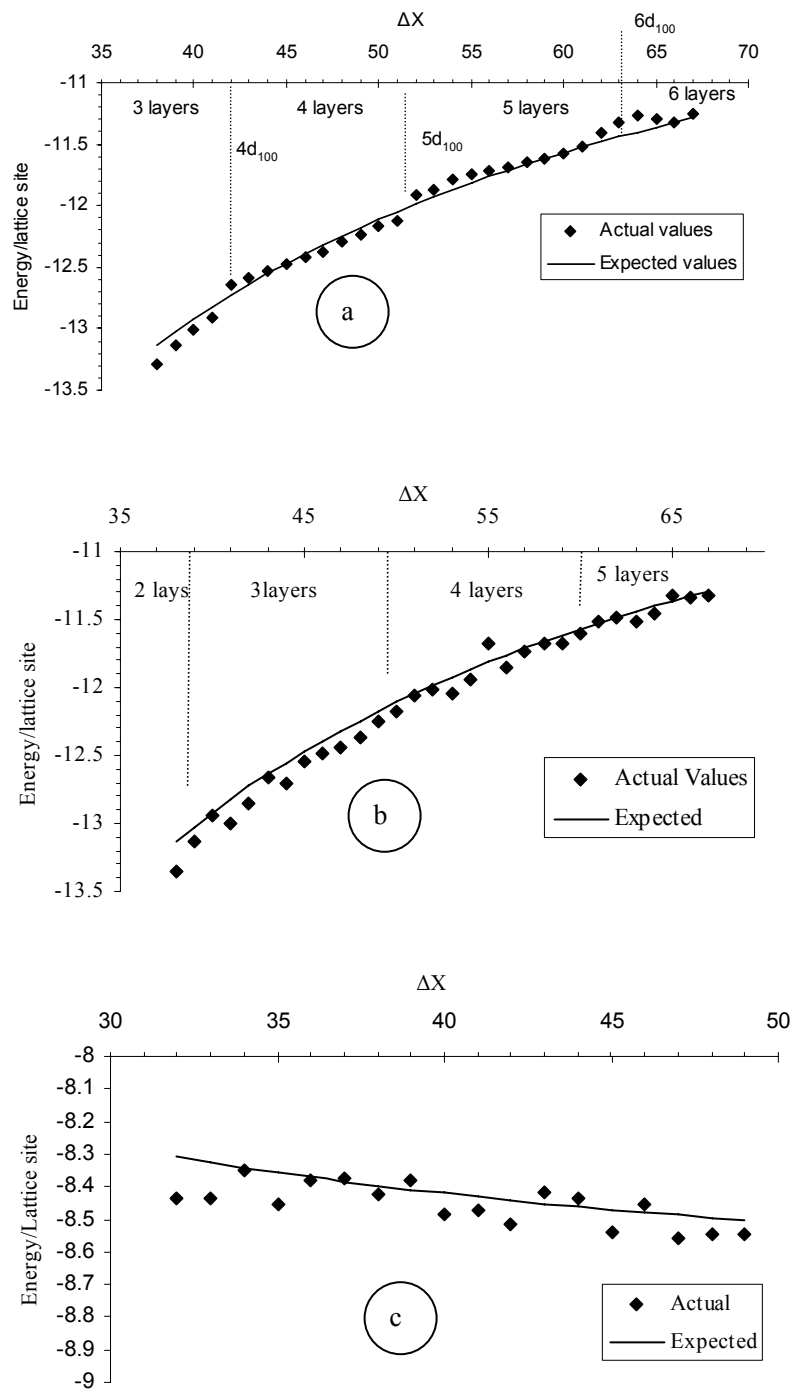
Figure 3.7. Equilibrium energy vs. spacing between the walls in slit-shaped cavities with (a) hydrophilic, (b) hydrophobic, or (c) neutral walls

(a)

(b)

(c)

(d)

(e)
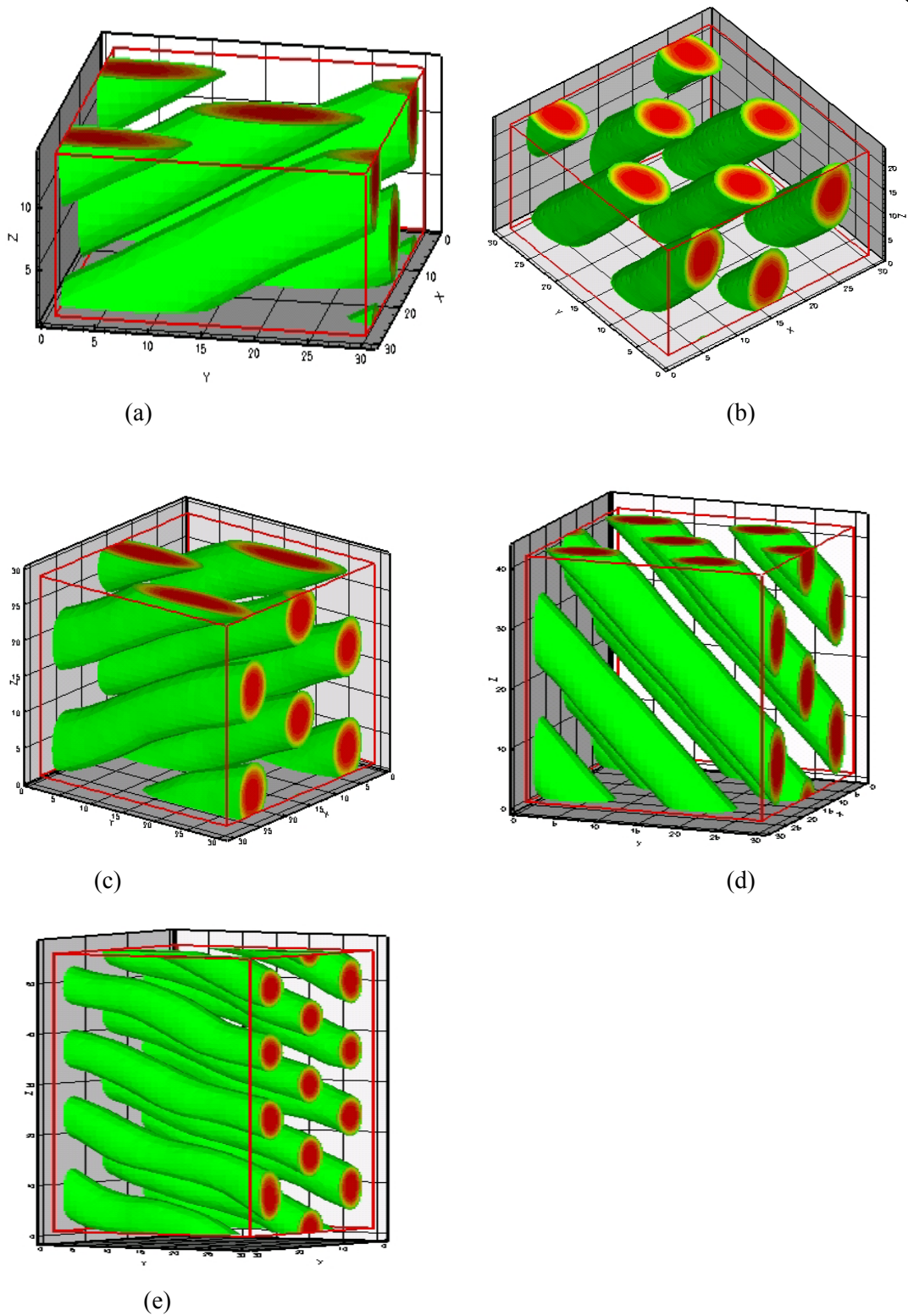
Figure 3.8. Simulated tail density contour plots with hydrophilic walls present in 'x' direction in a 30 * 30 * z box where z'= (a) 14, (b) 23, (c) 29, (d) 42, (e) 56
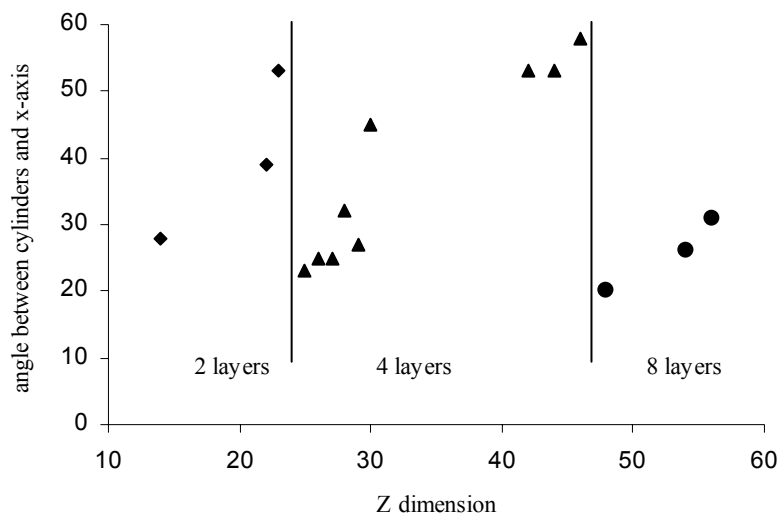
Figure 3.9. Angle of inclination between the cylindrical channels and x-axis as a function of the box dimesion in z- direction. The dimensions in the x- and y- directions were both 30 for this case and hydrophilic walls were present in the x direction.
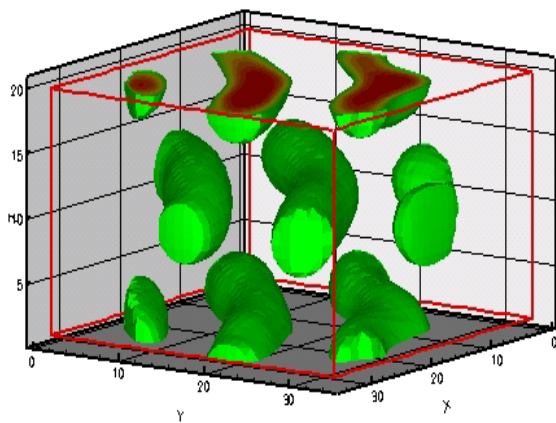
Figure 3.10. Tail densities of a HCP mesophase in a cylindrical cavity (diameter = 32, height = 20) with neutral walls

(a)

(b)

(c)

(d)

(e)

(f)

(g)

(h)

(i)
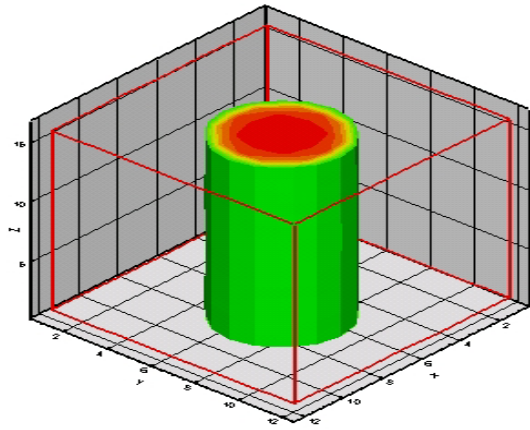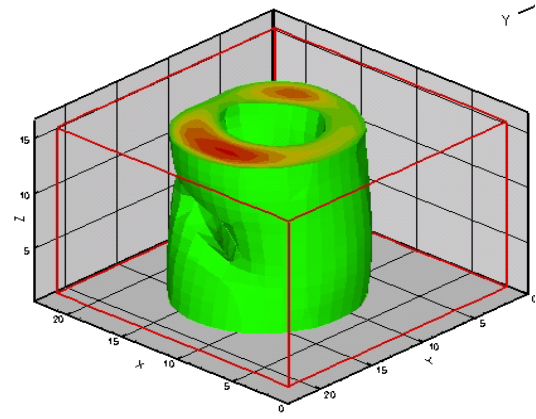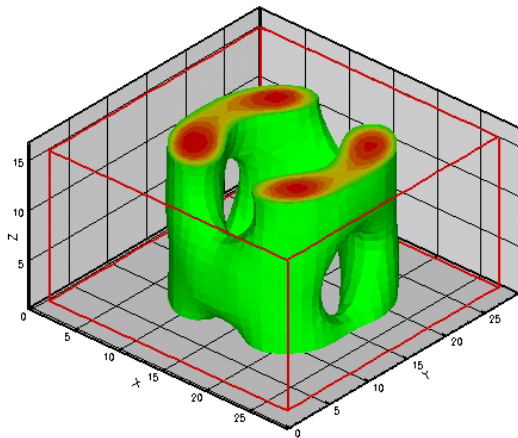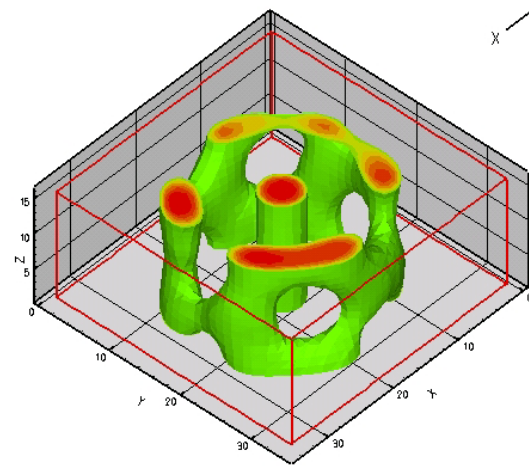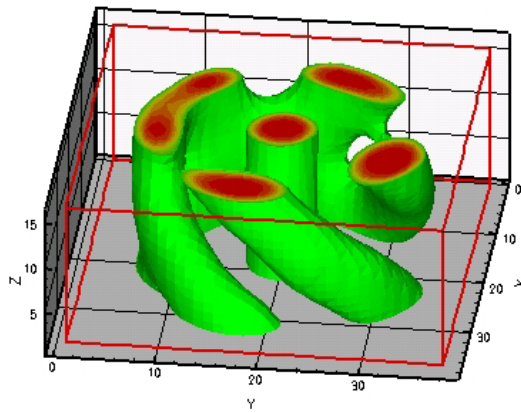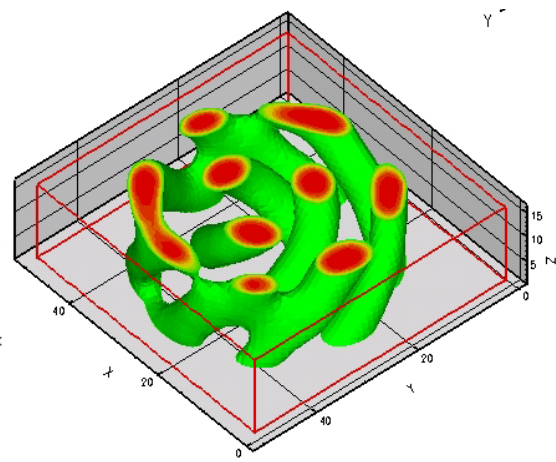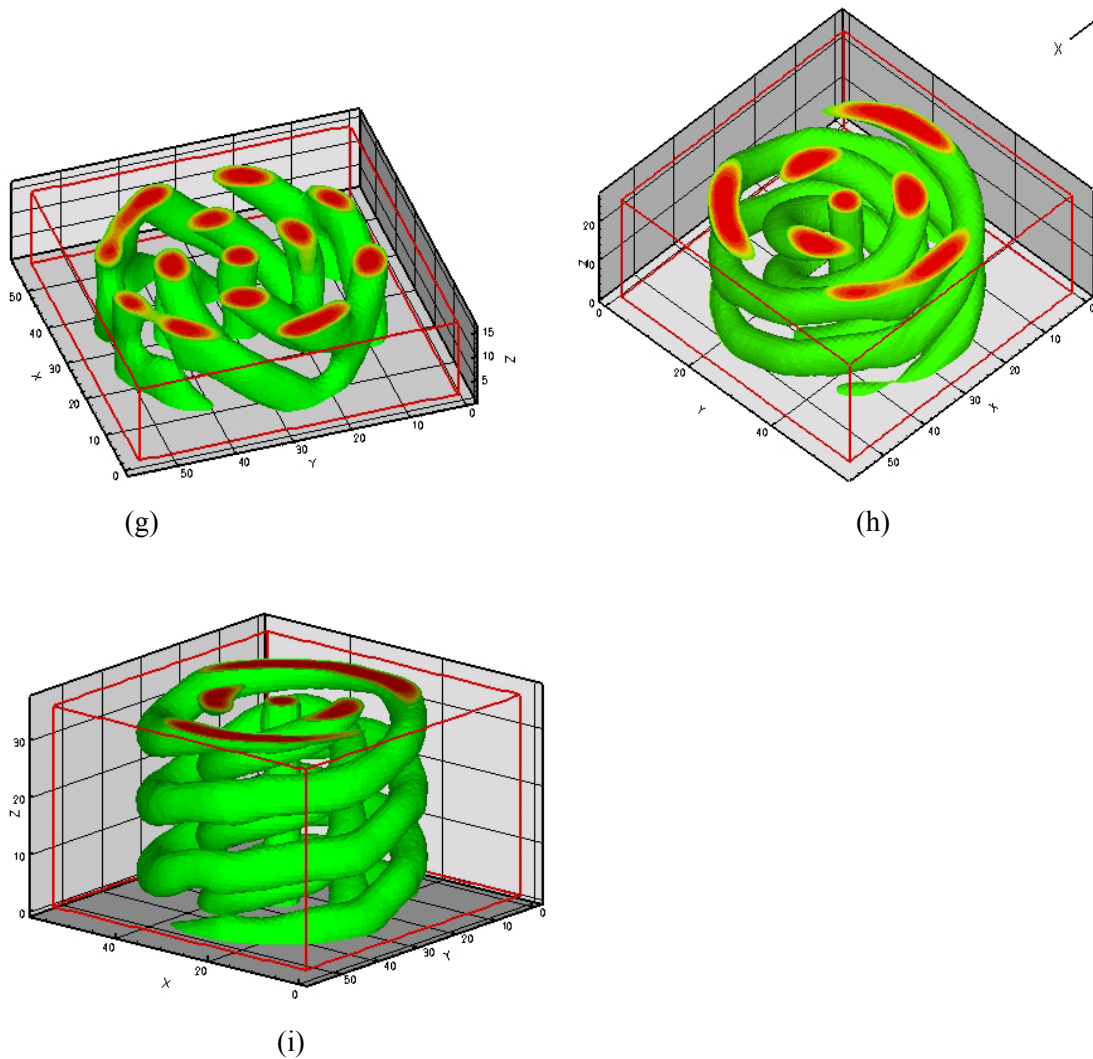
Figure 3.11. Tail densities of HCP mesophase in a cylindrical cavity of diameter 'D' and height 'H' with hydorphilic walls where (a) D = 10, H = 16 (b) D = 20, H = 16 (c) D = 26, H = 16 (d) D = 32, H= 16 (e) D = 36, H = 16 (f) D = 48, H = 16 (g) D = 54, H = 16 (h) D = 54, H=26 (i) D = 54, H = 36
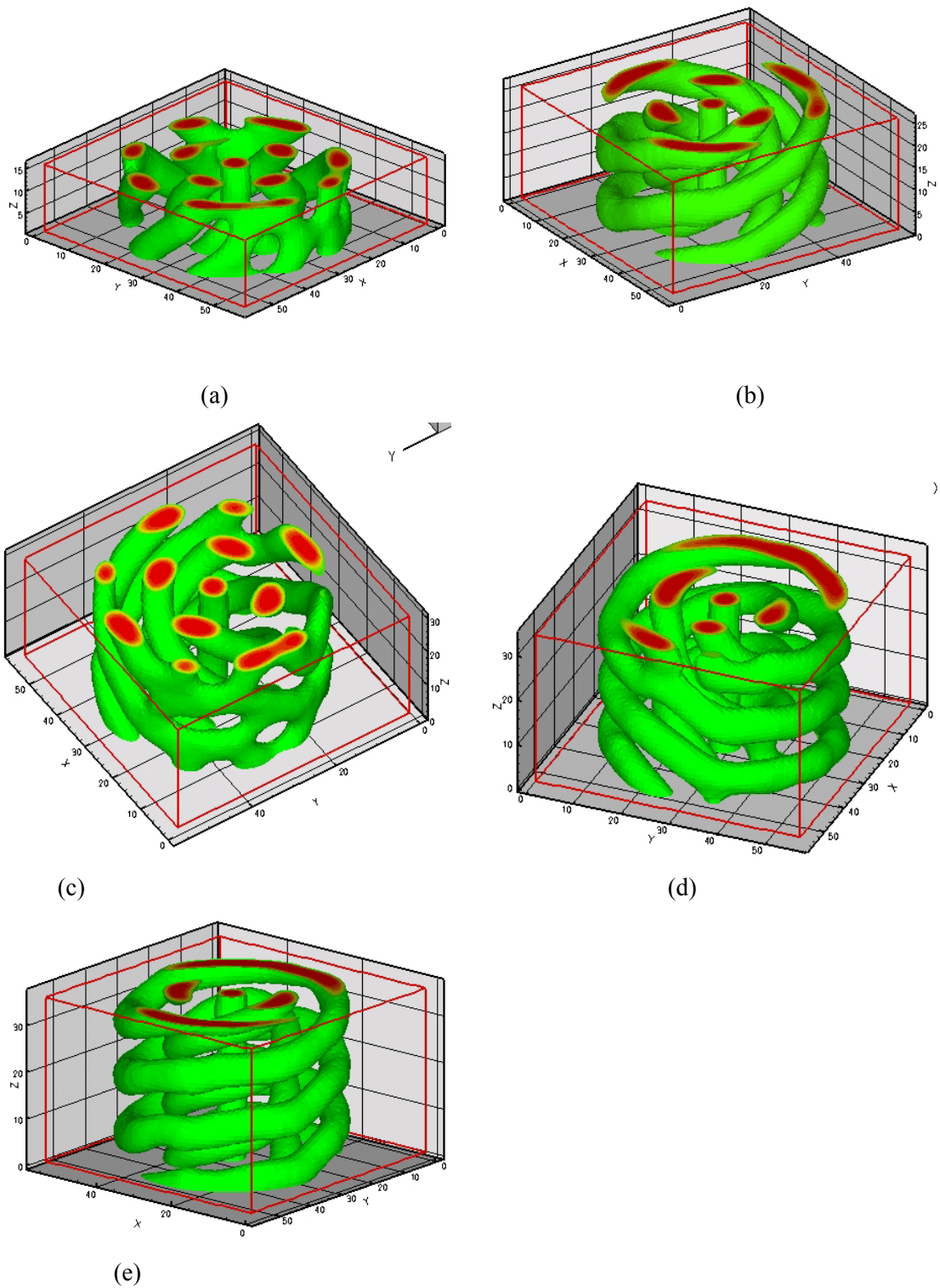
Figure 3.12. Tail densities of HCP mesophase in a hydrophilic cylindrical cavity of diameter 54 and height 'H' = (a) 16, (b) 26, (c) 30, (d) 34, (e) 36
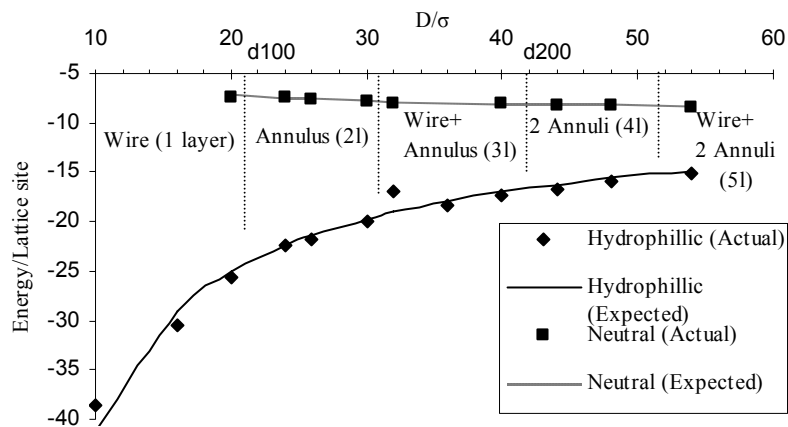
Figure 3.13. Plot of equilibrium energies of the HCP mesophase in cylindrical cavity as a function of the radius of the cavity
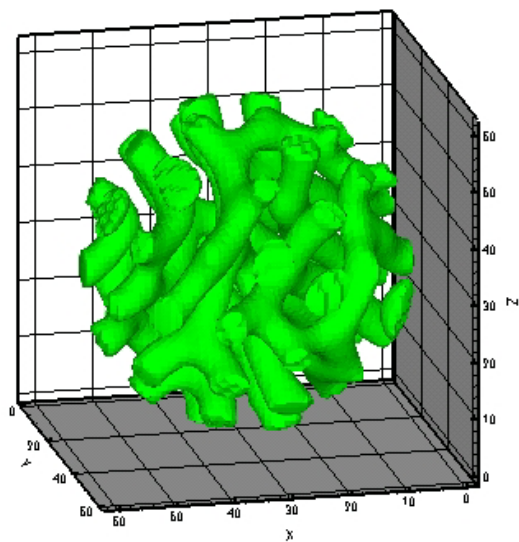
Figure 3.14. Simulated tail densities of surfactant molecules in a spherical cavity of diameter D = 58 with neutral walls

(a)

(b)

(c)

(d)

(e)

(f)
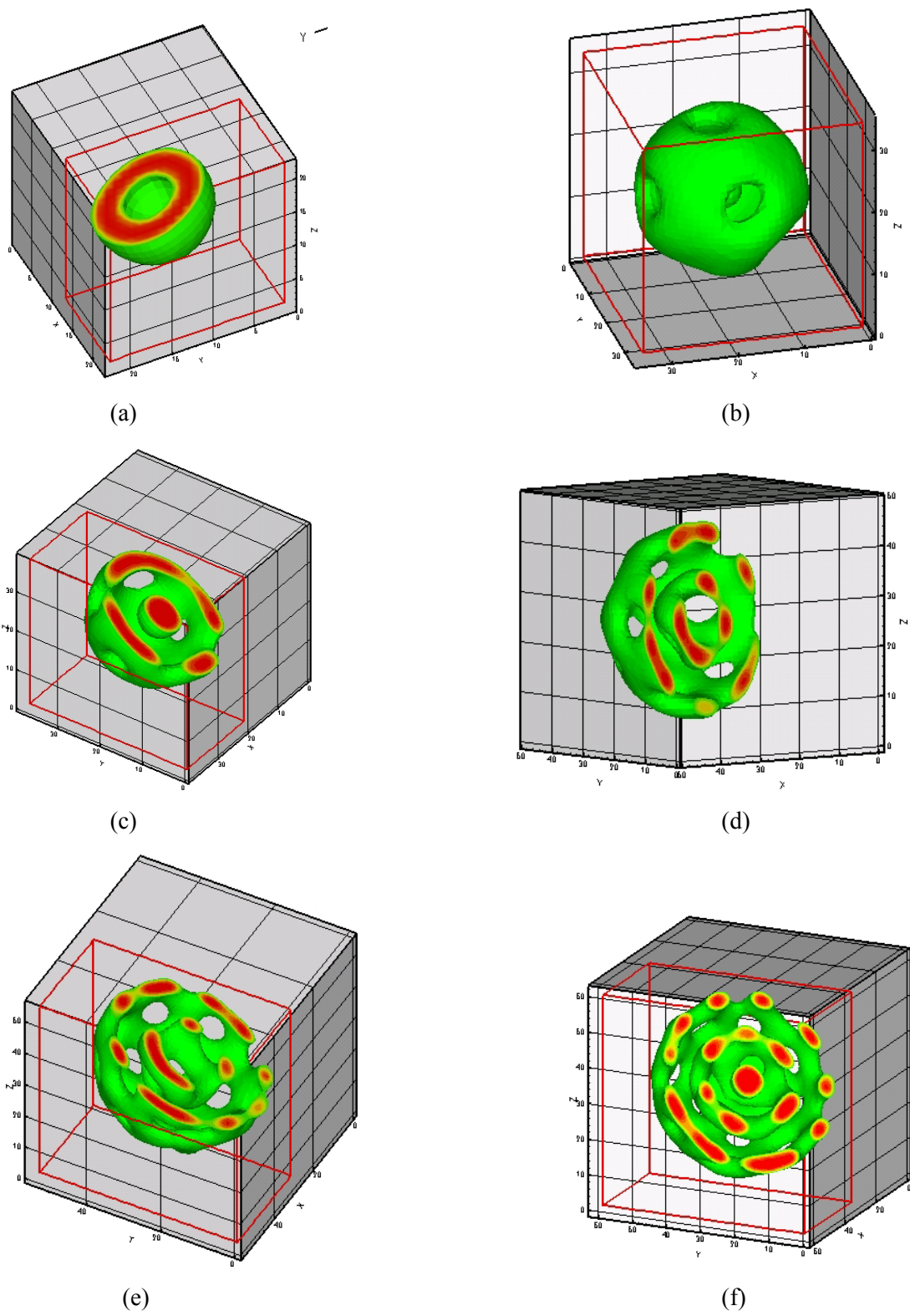
Figure 3.15. Simulated tail densities of surfactant molecules in hydrophilic spherical cavity of diameter D = (a) 20, (b) 32, (c) 36, (d) 46, (e) 52 and (f) 58
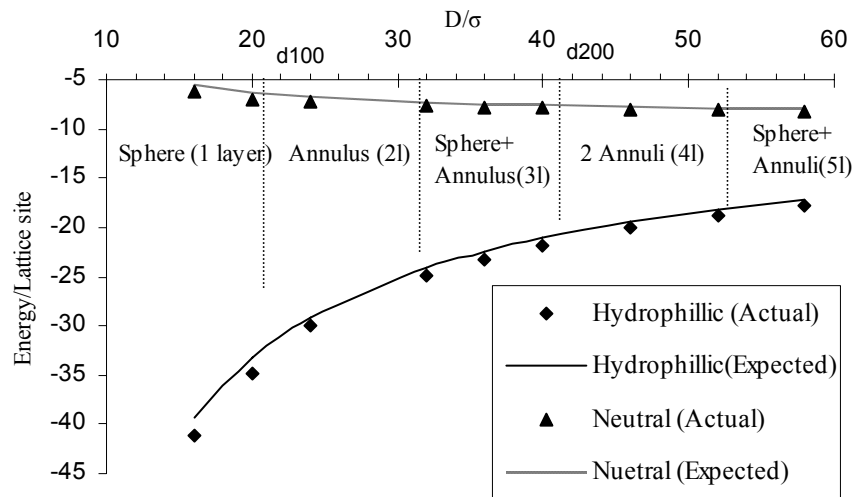
Figure 3.16. Plot of equilibrium energies of the HCP mesophase in spherical cavity as a function of the radius of the cavity

Chapter 4 Synthesis of Surfactant-Templated Silica Films with Orthogonally Aligned Hexagonal Mesophase

4.1. Introduction

Since mesoporous ceramic films with 2D hexagonal close packed (HCP) cylindrical pores were first prepared by surfactant templated coating processes,[64, 172] researchers have sought methods to prepare hexagonal close packed (HCP) cylindrical pore structures oriented orthogonal to the films.[173, 174] This orientation would provide an array of well-defined, unidirectional and uniformly sized pores with a minimal pathlength through the film. Like the close-packed pore arrays of anodized alumina, this structure could be used for many applications including membrane separations, sensor components, and nanoscale templates for arrays of nanorods, nanotubes and other structures.[175, 176] Electrochemical etching of the oxide layer of aluminum is an established method to produce large uniform arrays of cylindrical pores in chemically and thermally robust films.[177, 178] However, the size of the pores in anodized alumina is limited to the range from 10 to 100 nm.[179, 180]

Dip coating of ceramic precursors with self-organizing pore templates (such as surfactants or block copolymers) offers an alternative approach to the synthesis of thin nanoporous metal oxide films.[181] This is a rapid, controllable technique, and removal of the structure directing agents from these films leaves uniform, ordered pores comparable to the size of the micelle templates (in the range of 2 to 10 nm). Using cationic and nonionic surfactants, Lu et al.[64] were first able to conclusively demonstrate the formation of films with well-ordered 2D HCP arrays of cylindrical channels. However, application of these materials for nanotemplating is limited because preferential interactions between the head groups of the surfactant molecules and the substrate aligns these cylindrical channels parallel to the substrate.[64] This parallel orientation makes the pores inaccessible. Cubic bicontinuous pore structures have been used as an alternative to achieve accessible pores.[182, 183] However, bicontinuous pore structures allow diffusion to occur laterally in addition to the preferred direction, and therefore cannot be used to prepare arrays of isolated nanostructures. Orthogonally aligned cylindrical channels are needed for nanotemplating, and for avoiding lateral diffusion. Forming these structures by surfactant templating provides a direct route to a wider range of pore sizes, pore spacing, and matrix materials than have been obtained using anodized alumina.

It has been shown that the macroscopic orientation of 2D HCP mesoporous silica domains within the plane of the film can be controlled by using flow fields and substrate topology.[184-186]

Partial orthogonal alignment has been achieved by using flow fields to generate arrays of topological defects,[187] by seeding the films with nanoparticles,[188] or using controlled evaporation.[175] However, none of these methods has permitted complete orthogonal alignment of the pores. Truly orthogonal pores were recently reported by growing SBA-15 (mesoporous silica prepared using PEO-PPO triblock copolymer as template) within the pores of anodized alumina.[189] This approach takes advantage of the parallel alignment of the surfactant micelles at the surface of the alumina pores, but presents the SBA-15 mesopores over only a fraction of the area, and still necessitates an alumina matrix. If the orientation of the micelles were controlled during synthesis, we should be able to create a pure silica (or other metal oxide) films.

Examples of orthogonal thin film mesostructure alignment are available in the diblock copolymer literature. Electric fields,[190-192] directional crystallization[193], solvent vapor treatment,[194] chemically patterned surfaces[195-199] and engineered surface topography[200, 201] have all been successfully used to align the micro domains in block copolymer films. In addition to these methods, simulations have shown that one can align anisotropic mesophases perpendicular to the substrates by eliminating preferential interactions between the blocks of the amphiphile and the substrate. This approach has processing advantages because it requires no specialized field-generating equipment or lithographic pattern generating methods. Both self-consistent field theory and Monte Carlo simulations have suggested that AB block copolymer lamellar mesophases should align parallel to walls that interact with a strong preference for either block.[202-205] Neutral walls, which have no strong preference for either block, align the lamellae perpendicular to the walls.[203-205] A more recent density functional theory study confirms the same trend for asymmetric block copolymers which form HCP mesophases.[206] Monte Carlo simulations of Rankin et al. confirm that orthogonal alignment is predicted for a short nonionic surfactant HCP mesophases confined between chemically neutral walls.[207]

The theoretical predictions about the effects of substrate chemistry on block copolymer mesophases orientation have been beautifully confirmed by the preparation of orthogonally aligned PS-PMMA block copolymer films in a number of studies by Russel and coworkers.[208-211] However, all of the polymers used have high molecular weights (~70-80 KDalton) so even if one block is selectively removed to create pores,[210] the spacings are still on the order of >20 nm. To the best of our knowledge no one has yet reported using a chemically neutral surface to align the anisotropic mesophases in surfactant-templated ceramics. Substrate surface chemistry has been explored only by comparing films prepared on the hydrophobic surface of graphite to those prepared on hydrophilic surfaces such as mica and silica. Consistent with the predictions of simulations,[37] the HCP channels align parallel to the substrate whether the surface is hydrophilic or hydrophobic.[212] Orthogonal alignment should be achieved on a chemically neutral surface, as

we test here. Pai et al. recently suggested that because mesophases formation coincides with silica polycondensation, the possibility to align and manipulate mesophases may be limited for surfactant-templated sol-gel films.[213] However, Cagnol et al. were able to modulate the phase of CTAB-templated silica by adjusting the humidity after film deposition.[214] We hypothesize that the mobility of silicates after dip coating is sufficient to allow mesophase reorientation when chemically neutral surfaces are present.

We will use triblock surfactant P123 as a pore template, which has an average composition $HO(C_2H_4O)_{20}(C_3H_6O)_{70}(C_2H_4O)_{20}H$. Zhao et al. have previously prepared thin films with 2D HCP pore structure (oriented parallel to silicon wafers) by dip coating.[215] Our strategy will be to modify glass slides by cross linking a thin film of PEO-PPO random copolymer on their surfaces, or by cross linking a thin film of the template copolymer itself on their surfaces. Both of these modification procedures will result in chemically neutral surfaces for the P123 templating agent which we use, but the average size of the PEO and PPO domains on the modified surfaces differs between them. We will show that under the right conditions, these modified slides can be used to prepare orthogonally oriented P123-silica films with HCP mesophases structure.

4.2.   Experimental Section

Before coating, all of the borosilicate glass substrates were cleaned in a 7:3 mixture of concentrated H_2SO_4 and 30% aqueous H_2O_2. Some of the slides were then modified by crosslinking either P123 or a PEO-PPO random copolymer. To a solution of 0.415 mM random copolymer in acetone was added a drop of glycerol to act as a crosslinker. An equimolar amount of 1,6 diisocynatohexane (DH) was then added drop wise to this mixture under constant stirring. The resulting solution was dip coated onto clean glass slides and the slides were aged at 120 ºC overnight to drive the isocyanate-hydroxyl reaction to completion. The same procedure was used to cross link P123 using 0.696 mM of the copolymer.

The coating solution was prepared by addition of a solution of P123 to a prehydrolyzed silica sol following the procedure of Lu et al.[189] First, tetraethoxysilane (TEOS), ethanol, water and HCl (mole ratio 1 : 3.8 : 1: $5*10^{-5}$) were refluxed at 70 ºC for 90 minutes. Then, the remaining water and HCl were added, increasing the concentration of HCl to 7.34mM. After stirring this mixture at 25 ºC for 15 min, the sols were aged at 50 ºC for 15 min. The required amount of P123 was dissolved in ethanol and this solution was added to the above aged silica sol with constant stirring. The final mole ratios were 1 TEOS : 22 C_2H_5OH : 5 H_2O : 0.004 HCl : 0.01 P123. Slides were dip coated with this sol at a withdrawal speed of 7.6 cm/min. Plain or modified slides were used as substrates. After coating a modified slide, an identically modified

slide was placed in contact with one side of the freshly coated slide. The films were then aged and dried at 40 ºC for 24 hr and at 100 ºC for 24 hr. To explore the effect of the relation between the surface and the surfactant chemistry, films were also prepared under identical conditions, but with Brij-56 (primarily $HO(C_2H_4O)_{10}C_{16}H_{33}$) replacing P123 in the sol. The mole ratio of Brij-56:TEOS was 0.0555:1. In the discussion below, P123 will be the surfactant unless Brij-56 is specifically mentioned.

The thickness of each film was measured using a Dektak 6M Stylus profilometer with a diamond stylus. XRD patterns were collected with a Siemens (D-5000) diffractometer using Cu K_α radiation (λ = 1.54098 Å). The thin films were analyzed in Bragg-Brentano geometry without further preparation. Pieces of mesoporous film were scraped off the slides and deposited onto lacey carbon TEM grids. TEM images were recorded on either a JEOL 2000FX or a JEOL 2010F microscope operated at 200 kV.

P123 (BASF), Brij-56 (Aldrich), TEOS (>99%, Fluka), deionized ultra filtered water (Fisher), anhydrous ethanol (Aaper Alcohol & Chemical), acetone (HPLC grade, Fisher), glycerol (99+%, Aldrich), DH (98+%), and random copolymer (75% EO, Mn ~ 12000, Aldrich) were all used as received.

4.3.   Results and Discussion

We start by confirming that the sol forms 2D hexagonal close packed cylindrical channels in films cast onto unmodified slides under the conditions used. Following the procedure described above, we were able to prepare transparent films without any macroscopic defects after deposition and drying by using P123 as a structure directing agent. The thickness of the films was found to be 240 nm using the profilometer. Fig. 4.1(a) shows the XRD pattern of material which was coated on an unmodified glass slide. We can clearly see the (100) reflection and its second order reflection. The d-spacing of the (100) planes is around 5.5 nm. Unlike powder products which show (110) reflection in addition to (100) and (200) reflections, no (110) reflection is observed due to preferential orientation of (100) along the plane of the substrate.[216] This observation is consistent with what others have reported for hexagonal phases and we have confirmed that the pore structure is stable after calcination at 550 °C for 4 hr in air (results not shown).

We modified some of the glass slides by cross linking a thin film of PEO-PPO random copolymer on their surfaces. We then coated these modified slides with the silica sol. A similarly modified slide was placed in contact with the coated slide immediately after coating and kept there during drying and aging. Fig. 4.1(b & c) shows the XRD patterns obtained from two different sides of the same modified, coated slide. The side which was in contact with a

similarly PEO-ran-PPO modified slide showed no reflections in the XRD pattern (fig. 4.1(b)), while the other side of the slide displays two well resolved peaks corresponding to the (100) plane and its second order reflection (fig. 4.1(c)). Similar to the film coated on an unmodified slide, the (100) d-spacing for this material (on the side not sandwiched with another modified slide) is 5.5 nm. The thickness of this and the other films cast onto modified slides were in the range of 240 ± 5 nm, consistent with the films prepared on unmodified slides. There was no evidence in the thickness profiles of any silica film being pulled off when the slides were separated after aging.

As described by Hillhouse et. al., when the HCP cylindrical mesostructure is oriented perpendicular to the substrate, we do not expect to see any peaks in the XRD pattern because the scattering vector does not lie in the plane of the sample in conventional Bragg-Brentano geometry.[216] However, the HCP phase does not need to be perfectly perpendicular to the substrate; HCP domains can have a distribution of angles with respect to the substrate and still show no reflections. Thus, the absence of XRD reflections from a film that was confined between two random PEO-PPO copolymer modified surfaces during aging only demonstrates that the HCP phase is oriented orthogonally away from the plane of the substrate. The presence of a significant amount of parallel-oriented domains would give rise to detectable reflections.

The second way that we modified the surface of the slides was to cross link a thin film of the template copolymer itself (P123) on the surface before coating it with the silica sol. This was done as a test to see whether the blockiness of the PEO and PPO groups on the modified surface influences the ability of the copolymer to act as a neutral surface. The simulations that predicted perpendicular orientation were based on chemically uniform surfaces,[202-207] so it was unknown how the size of the surface modifier blocks would affect orientation. During aging, the film was again confined between identical modified surfaces. Fig. 4.1(e) shows the XRD pattern obtained from the side which was kept in contact to a similarly modified slide. It does not have any reflections, as opposed to the side which was in contact with air (Fig 4.1(d)). For the side in contact with air, the d_{100} spacing is 5.2 nm. The absence of reflections in Fig. 4.1(e) shows that a surface modified with polymer blocks whose size is comparable to that of the surfactant template can still acts as a chemically neutral surface for the alignment of mesostructures.

In order to see if the absence of reflections in films sandwiched between modified slides was just because of confinement or if it was really a surface effect, we coated some silica films on modified slides (random copolymer or P123 modified) and placed an unmodified glass slide in contact with the films immediately after coating. The film was thus sandwiched between one chemically neutral surface and one hydrophobic surface during aging. Fig. 4.2(a) shows the XRD pattern from a film sandwiched between one random PEO-PPO copolymer modified slide

and one unmodified slide. Fig. 4.2(b) shows the XRD pattern from a film sandwiched between one P123-modified slide and one unmodified slide. In both the cases we can clearly see the (100) reflection and its second order reflection. The d_{100} fig. 4.2(a) is 5.2 nm and in fig. 4.2(b) is 5.5 nm. This demonstrates that it is important to sandwich these films between two chemically neutral surfaces in order to observe complete orthogonal alignment.

To confirm that chemical neutrality of the substrate is the reason for the orthogonal alignment, we also prepared silica films in which P123 was replaced with the nonionic surfactant Brij-56. This surfactant has a short PEO headgroup and a short alkane tail, rather than a PPO tail. The small size of the surfactant compared to the PEO-PPO blocks, and its different tail chemistry, should cause different interactions with a modified surface than are seen for P123. Fig. 4.2(c) shows that the Brij-56 templated film sandwiched between random copolymer modified slides gives a distinct reflection consistent with the hexagonal phase of Brij-56 templated films with the channels aligned parallel to the substrate[64] Fig. 4.2(d) shows the same parallel orientation for a Brij-56 templated film sandwiched between P123-modified slides. These observations demonstrate the importance of the modified surface being designed so that it is neutral towards the specific chemistries present in the surfactant template that is being used.

Up to this point, we have been taking the loss of x-ray reflections as an indicator of orthogonal alignment. The absence of x-ray reflections provides better statistical evidence for orthogonal alignment than TEM, since films with some orthogonal alignment sometimes also contain domains with parallel alignment.[175, 187] However, x-ray reflections could also disappear if the long-range order were simply lost. We differentiate between these possibilities by using TEM to directly image the pore ordering in the material. An XRD pattern from a modified surface showing no peaks coupled with TEM images which show hexagonal ordering is sufficient for us to conclude that we have a 2D HCP pore structure oriented orthogonal to the substrate.

Fig. 4.3 shows the TEM image of material removed from an unmodified slide. The piece of film shown contains close-packed cylindrical channels, which in Fig. 4.3 are viewed from the edge. The d-spacing obtained from XRD is consistent with the channel spacing in the TEM images. This confirms that we form a well ordered 2D HCP cylindrical phase on unmodified slides using P123 as a template with the recipe described above. The (100) and (200) reflections in the XRD pattern indicates that the (100) plane of cylinders in the HCP structure lies parallel to the substrate.[216]

Fig. 4.4 shows TEM image of material obtained by scraping material from a slide which was modified with cross-linked PEO-ran-PPO. Fig. 4.4(a) and 4.4(b) are two views of material removed from the film which was dried and aged between two modified slides. We can clearly see regions with hexagonal cylindrical patterns (Fig. 4.4a) and stripe patterns showing that we

have channels rather than spherical pores (Fig. 4.4b). These images show that the absence of XRD reflections is not due to loss of order, but to alignment of the cylindrical pores orthogonal to the substrate. The TEM image of material removed from the other side of the same film (which was in contact with air) shows the same well-defined HCP structure (Fig. 4.4c).

We have also modified the surface of glass slides by cross linking P123 itself on the surface. A representative TEM image of the material scraped off from the side of a slide which was confined with another P123-modified slide is shown in Fig. 4.5a. This image, along with the absence of reflections in the XRD pattern obtained from this same side of the film confirms that we are able to prepare a 2D HCP mesophase orthogonal to the surface. Fig. 4.5b shows that the same HCP pore structure is also found on the side of the film aged in air, even though the XRD pattern indicates parallel pore alignment for this side of the film.

Taken together, the above results show that when the surface of a glass slide is modified by cross linking PEO-PPO copolymers with blocks shorter than or the same size as the template copolymer (random copolymer and P123 modified surfaces, respectively), one can align the 2D hexagonal close-packed cylindrical mesophases in the direction orthogonal to the substrate. However, to see complete orthogonal alignment, it appears to be important to sandwich the freshly deposited film with another modified slide. Films cast on modified slides but exposed to either air (a hydrophobic surface) or unmodified glass (a hydrophilic surface) show at least partial mesophases alignment parallel to the substrate. It is likely that these films actually have an orthogonally aligned layer near the modified substrate. However, preference for one block at the air-film or glass-film interface probably creates a parallel layer near that surface. Also, the experiment with Brij-56 shows how important it is to have modified surfaces that are chemically neutral toward the specific template being used to prepare the film. Either because of the small size of the PEO and alkane segments in Brij-56 or because the modified surfaces have a net attraction for PEO blocks of Brij-56, we observe parallel mesophases alignment of Brij-56 templated films sandwiched between modified slides.

4.4. Conclusions

In this brief report we have demonstrated the preparation of oriented 2D hexagonal close packed cylindrical channels in 240 nm thick P123-templated silica films. We have successfully implemented the idea from molecular simulations that confinement of a nonionic surfactant mesophases between chemically neutral surfaces will align the cylindrical pore channels in the direction orthogonal to the substrate. A combination of XRD and TEM characterization confirmed the preservation of the HCP structure and its orientation out of the plane of the substrate. Both random PEO-PPO and the surfactant itself (P123) have been crosslinked to

70

create chemically neutral surfaces. At this stage, we found it essential to sandwich the films between two chemically modified surfaces to induce complete orthogonal alignment. Contact of one surface of the film with either air or unmodified glass caused a loss of orthogonal alignment. Since the films were all originally cast with one side exposed to air, this suggests that the as-deposited films are able to reorient while aging in contact with a pair of chemically modified surfaces. These films are promising structures for a variety of applications, and in the future we plan to present more detailed studies of the compositional variety allowed by these films, and further characterization of their properties.
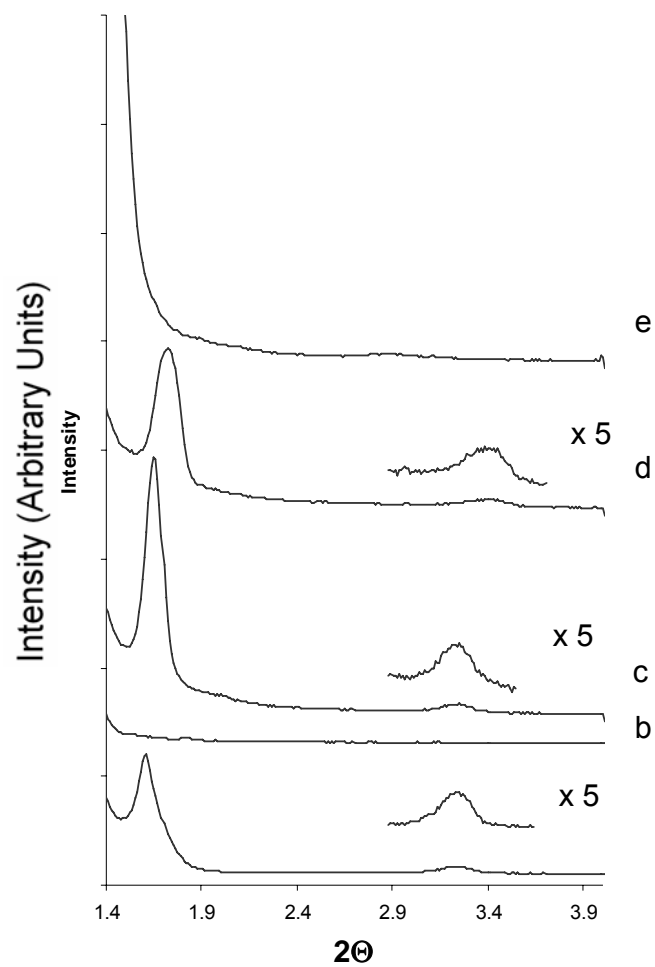
Figure 4.1. XRD patterns of P123-templated silica films (a) coated on an unmodified slide; coated on a slide on which random copolymer was cross linked before coating and exposed to (b) a similarly modified slide or (c) air; or coated on a slide on which P123 was crosslinked before coating and exposed to (d) air or (e) a similarly P123-modified slide. The patterns were offset vertically for clarity, and trace (e) was cut off at a value above which no features are seen.
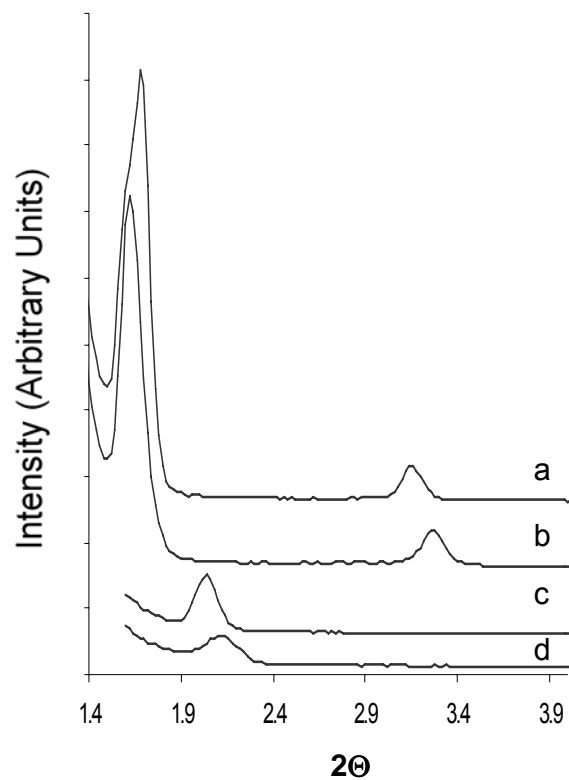
Figure 4.2. XRD patterns of P123 and Brij56 templated silica thin films (a) coated on a random copolymer-modified slide and exposed to an unmodified slide or (b) coated on a P123-modified slide and exposed to an unmodified slide. XRD patterns of Brij-56 templated films (c) coated on a random copolymer-modified slide and exposed to a similarly modified slide or (d) coated on a P123-modified slide and exposed to a similarly modified slide.
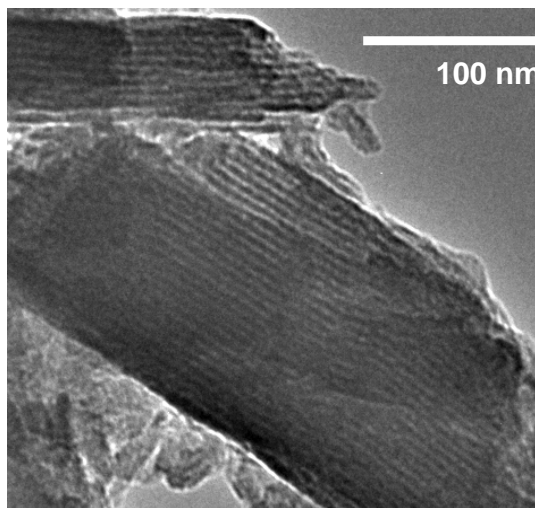
Figure 4.3. TEM image of sample coated on unmodified slide and scraped off.
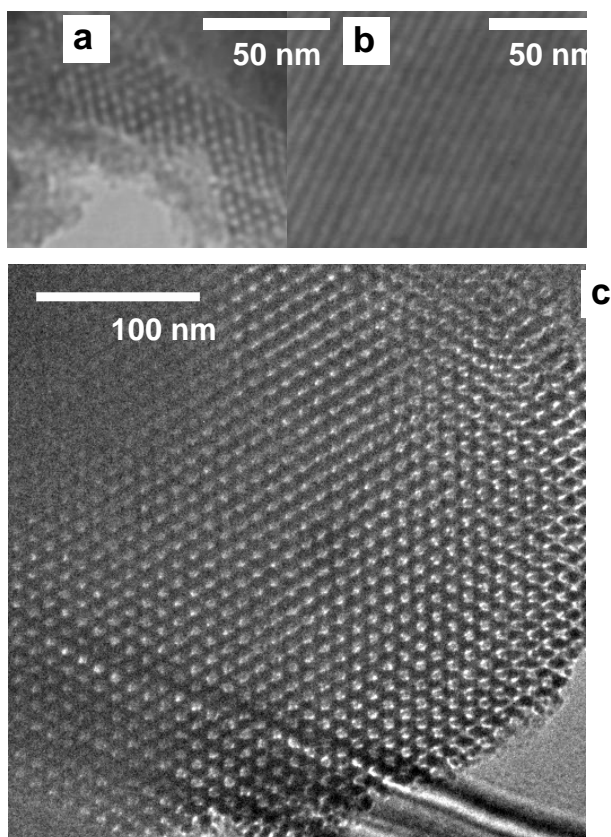
Figure 4.4. TEM images of pieces of P123-templated silica thin film scraped from the random copolymer-modified glass substrate (a) and (b) are two views of the material scraped from the film sandwiched between two random copolymer-modified slides, and (c) is a view of the material scraped from the side exposed to air.
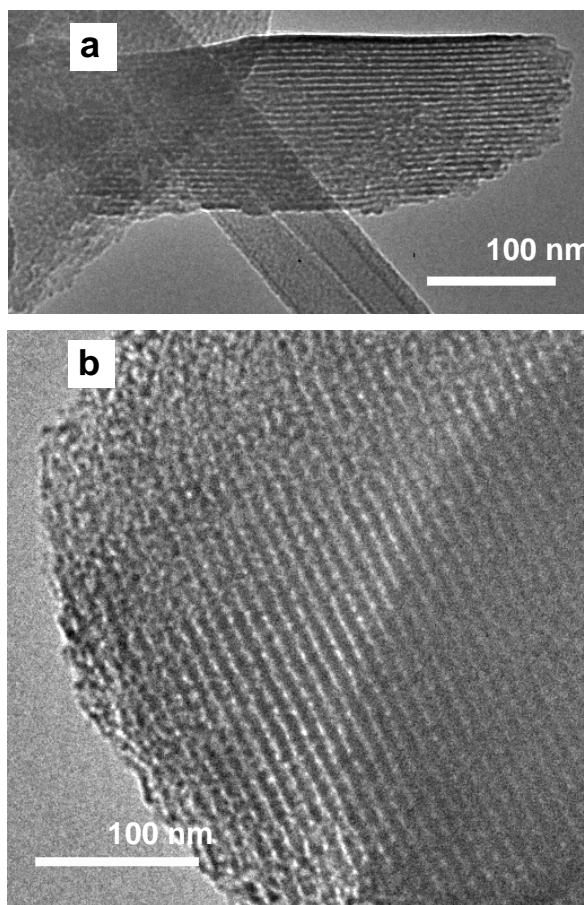
Figure 4.5. TEM images of pieces of P123-templated silica thin film scraped from the crosslinked P123-modified glass substrate. (a) material scraped from the film sandwiched between two crosslinked P123-modified slides, and (b) material scraped from the side exposed to air.

Chapter 5 Generalized Coating Route to Silica and Titania Films with Orthogonally Tilted Cylindrical Nanopore Arrays

We describe a simple, inexpensive coating method to produce thin silica and titania films with surfactant templated, orthogonally tilted cylindrical nanopore arrays. These films can be deposited onto any substrate because orientation of the 2-D hexagonally close packed (HCP) mesophases out of the plane of the film is directed by a chemically neutral sacrificial copolymer layer. Orientation of the HCP mesophases through the entire thickness of films cured in open air is achieved by limiting the coating thickness. This generalizes the coating method by making it possible to deposit oriented films on substrates of any curvature and size. We find a critical thickness between 70 and 100 nm, below which the triblock copolymer surfactant-templated HCP phase aligns completely out of the plane of glass and silicon wafer substrates. Above this thickness, the effect of the chemically neutral bottom layer does not propagate across the entire film, and alignment of the HCP mesophases parallel to the (nonpolar) air interface produces a mixed orientation.

Surfactant templated thin mesoporous ceramic films[64, 172] find applications in a variety of fields like membrane separations,[218, 219] sensors,[53, 220] and catalysis.[221] Though suitable for many applications, anisotropic mesophases like 2-hexagonally close packed (HCP) and lamellar phases have a strong tendency to align parallel to the substrate surface.[222] Parallel aligned HCP channels are not accessible to large solutes, which limits their usefulness. Thus, there has been an ongoing quest to develop fabrication methods for ceramic films with orthogonally aligned HCP cylindrical nanopores. This geometry is ideal for applications requiring a uniform array of accessible but independent cylindrical nanopores where block copolymer films[223] and anodized metal films[224] are currently used. Because controlling orientation in these classes of materials is understood, several groups have used them as templates for oriented ceramic films. One templating approach uses selective mineralization of pre-oriented block copolymer HCP mesophases.[225, 226] This has been quite successful, but disadvantages include relatively large pores (>10 nm), long annealing times prior to mineralization, and the large expense of the copolymers. The second templating approach uses synthesis of mesoporous ceramics within the macropores of anodized alumina.[41, 43] However, researchers are only beginning to understand how to favor the formation of orthogonally oriented HCP silica over circular, helical, and multilamellar structures.[44] Other limitations of this approach are that a large portion of the film

area is taken up by the alumina template, and that gaps are usually introduced by shrinkage of the silica. Bicontinuous 3D mesophase films are another way to achieve accessible nanoporous ceramic films,[39, 130, 227, 228] but they provide alternate diffusion paths that limit the applications of the films.

We recently demonstrated that if, after dip coating, surfactant templated sol-gel silica films are confined between a pair of modified, chemically neutral surfaces, a film is obtained with HCP channels oriented out of the plane of the film.[50] At that time we concluded that it was necessary to sandwich the as-deposited 240 nm thick silica films between two chemically modified surfaces to align the mesophase orthogonal to the film throughout its entire thickness. Here we demonstrate that when the thickness of the silica film is reduced, it is no longer necessary to confine the film between two modified surfaces to achieve orthogonal orientation through the entire thickness. To show this, a clean glass substrate was modified by coating with PEO-r-PPO copolymer which was reacted with 1,6-diisocyanatohexane and a glycerol cross-linker.[229] After curing, these modified glass slides were then coated with a silica sol prepared by a standard procedure.[8] P123 (average composition: $HO(C_2H_4O)_{20}(C_3H_6O)_{70}(C_2H_4O)_{20}H$) was used as surfactant pore template and tetraethylorthosilicate was used as silica precursor. Varying the thickness of the silica films was achieved by diluting the original sol with increasing amounts of ethanol to obtain thinner films. The films were aged and dried at 40 °C for 24 h and 100 °C for 24 h. Aged films were calcined in air by increasing the temperature at 1 °C/min to 500 °C and holding for 4 h. To demonstrate the applicability of chemically neutral surfaces to align the cylindrical channels in other ceramic films, we have deposited surfactant templated titania films on similarly modified surfaces. Titania sols were prepared by adding 2.1 g titanium(IV) ethoxide to 1.53 g conc. HCl (36 wt%). After stirring this mixture for 10 min, a solution containing 0.65 g P123 dissolved in 6 g ethanol was added.[230] Films were dip coated from this sol onto PEO-r-PPO copolymer modified surfaces and were aged in a highly humid environment (RH ~ 95%) in a refrigerator (temperature ~ 4 °C) for 2 h. Titania films were then calcined by increasing the temperature at 25 °C/min to 400 °C and holding for 10 min.[231] Si wafers coated from similarly diluted sols were used as ellipsometry samples to measure the thicknesses of the films. Grazing Incidence Small Angle X-ray Scattering (GISAXS) data were obtained at the Advanced Photon Source at Argonne National Labs on beamline 8-ID using a wavelength of 1.675 Å and a sample-detector distance of 2010 mm. Data were collected with a 2048 x 2048 MarCCD with a pixel size of 79 μm. Powder x-ray diffraction (XRD) patterns were collected on Siemens (D-5000) diffractometer and transmission electron microscopy (TEM) images were collected on a Jeol-2000fx instrument. Scanning Electron Microscopy (SEM) images were

collected on FEI XL30 Sirion SEM with FEG source operated at an accelerating voltage of between 3 and 5 kV.

Fig. 5.1 shows the powder XRD patterns of silica films of varying thickness coated on PEO-r-PPO modified glass surfaces. In the Bragg-Brentano geometry used for XRD, diffraction in the plane of the substrate is not detected. Therefore, an orthogonally tilted mesophase should not yield any XRD diffraction intensity.[232] In Fig. 5.1 we can clearly see that the diffraction intensity decreases as the thickness decreases from 240 nm (Fig. 5.1d). Films with thicknesses of 50 nm and 70 nm cast on copolymer-modified substrates do not show any diffraction peaks at all. In contrast, 50 nm-thick mesoporous silica film of the same composition coated on an unmodified plain glass slide gives an intense (100) peak due to alignment of the 2D HCP phase parallel to the substrate (Fig. 5.1e). This suggests that the loss of intensity in the case of the thinnest films cast onto modified surfaces is not due to the decrease in the thickness, but is an orientation effect.

As direct verification of the orientation indicated by XRD, Fig. 5.2a shows the GISAXS pattern of a 70 nm thick HCP silica film cast onto a PEO-r-PPO substrate and held horizontally in the beam. Consistent with the 2D HCP phase being completely tilted orthogonal to the film, two spots are observed to the left and right of the beam, and no diffracted intensity out of the plane of the film. The converging streaks extending from the spots indicate that there is a distribution of channel orientation angles centered at 90° relative to the substrate. The presence of any parallel aligned HCP domains would give rise to out-of-plane diffraction resulting in spots as seen many researchers, or an oval pattern if a polycrystalline area is sampled.[233, 234] Fig. 5.2b shows the GISAXS pattern of a 100 nm thick silica film on a PEO-PPO modified surface held horizontal to the beam. Even though it is only 30 nm thicker than the sample in Fig. 5.2a, the pattern consists of two horizontal spots on either side of the beam and a diffracted spot out of the plane, connected with diffuse intensity in an umbrella-shaped pattern. This pattern is best interpreted as HCP channels oriented perpendicular to the substrate-film interface and parallel to the film-air interface, with randomly oriented regions or defects joining the two. Based on the XRD results, there appears to be a critical thickness between 70 nm and 100 nm below which the HCP phase is orthogonally tilted across the entire thickness of the film. Above this thickness, the influence of the surface decays enough that parallel and randomly oriented domains contribute to the GISAXS pattern.

In addition to the x-ray scattering studies, direct characterization confirms the orthogonally tilted orientation of the pores in P123-templated films below the critical deposition thickness. Fig. 5.3 shows a representative plane-view TEM image of a 70 nm thick silica film which was cast on a PEO-r-PPO modified multilayer and delaminated from the substrate surface during

calcination.[235] We can clearly see the 2D HCP pattern of pores. This is the first direct TEM evidence of orthogonal pore alignment of the 2D HCP channels in dip coated, templated mesoporous ceramic films. Fig. 5.4 shows SEM images of fractured titania films of different thicknesses deposited on the same type of chemically neutral glass surface. The conductivity of the titania films allowed these images to be captured without metal coating, which has been found to obscure the pore texture of the silica films. The top surface of both samples clearly shows long range hexagonal periodicity. The thicker film (~ 200 nm thick, Fig. 5.4a) was confined between two chemically neutral surfaces to align the channels through the entire thickness, and clearly shows vertically aligned cylindrical channels in the cross sectional view in addition to the hexagonal periodicity of the top surface. The thinner film (Fig. 5.4b) was cured in air without sandwiching, and shows similar hexagonal ordering on the top surface with well aligned channels in the cross section. We also see periodic ridges in the cross sectional image along the length of the pore in this thin film, which may be either an artifact of sample preparation by fracturing or a feature introduced during calcination and crystallization.

These results conclusively demonstrate that modifying substrates with PEO-PPO copolymers to produce a chemically neutral surface allows us to dip coat PEO-PPO triblock copolymer-templated ceramic films with orthogonally tilted HCP pores (centered at perfectly orthogonal but with a distribution of tilted domains). When the thickness of the films is controlled to be below a critical thickness (between 70 and 100 nm in this case), there is no need to confine the film between two modified surfaces to achieve this orientation. Thus, orthogonally tilted HCP nanopore ceramic films can be deposited on substrates of arbitrary shape and curvature (including spheres, wires, tubes, etc.). Because of the sacrificial PEO-PPO block copolymer (removed during calcination) used to induce alignment, this method can be applied to a substrate of any composition onto or into which the PEO-PPO copolymer layer can be deposited, including porous substrates. In results to be reported separately, we have deposited orthogonally tilted membranes onto anodized alumina supports and found permeation results consistent with the pore size. Filtering out 20 nm gold particles using these membranes (while allowing 5 nm gold particles to pass through) shows that defect-free, uniform porous films are formed. This approach is amenable to widespread use and adaptation because the structure directing PEO-PPO surfactants are inexpensive (e.g. roughly 1/4500 the cost of the PS-b-PEO copolymer used in a previous report for selective mineralization[225]), because the evaporation-induced self-assembly process is rapid, and because post-processing can be accelerated and incorporated into microelectronic fabrication processes.[236] By carefully choosing the ceramic precursor, these orthogonally aligned mesoporous ceramic films can find numerous applications in photovoltaics, fuel cells, etc.
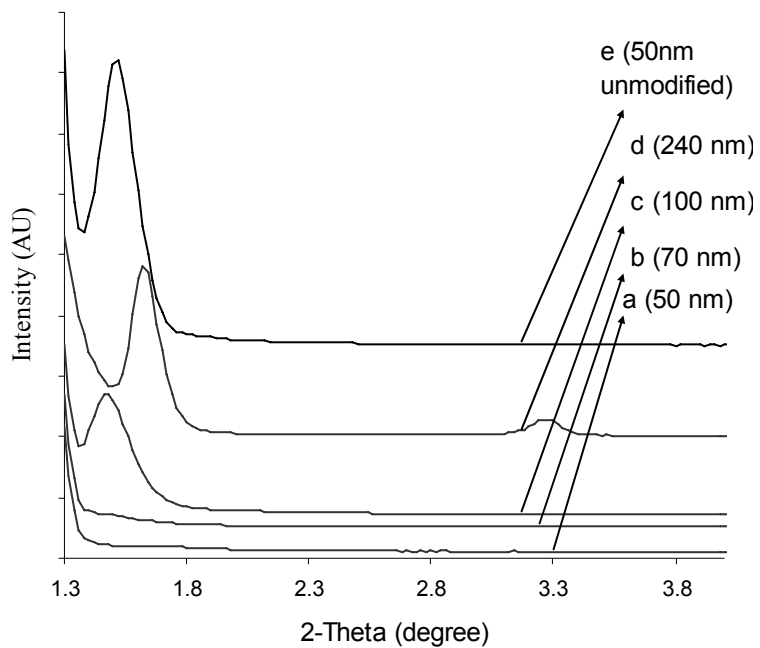
Figure 5.1. XRD patterns of P123 templated films on random copolymer modified slides (a-d) exposed to air (a) 50nm thick, (b) 70nm thick, (c) 100nm thick, (d) 240nm, (e) 50nm thick film on unmodified glass slide.
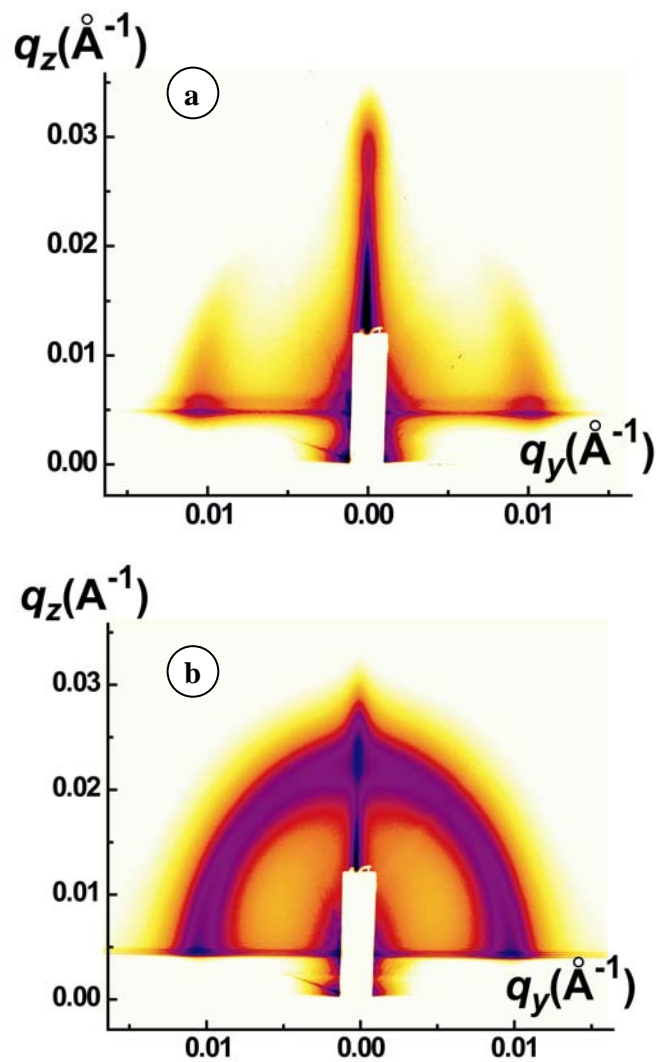
Figure 5.2. GISAXS patterns of mesoporous silica films on modified substrates (a) 70nm thick (b) 100nm thick. These data were collected by Darren Dunphy of Sandia National Laboratories (Abuquerque, NM) at the Advanced Photon Source at Argonne National Lab, with experimental assistance   from   Xuefa   Li   and   Jin   Wang
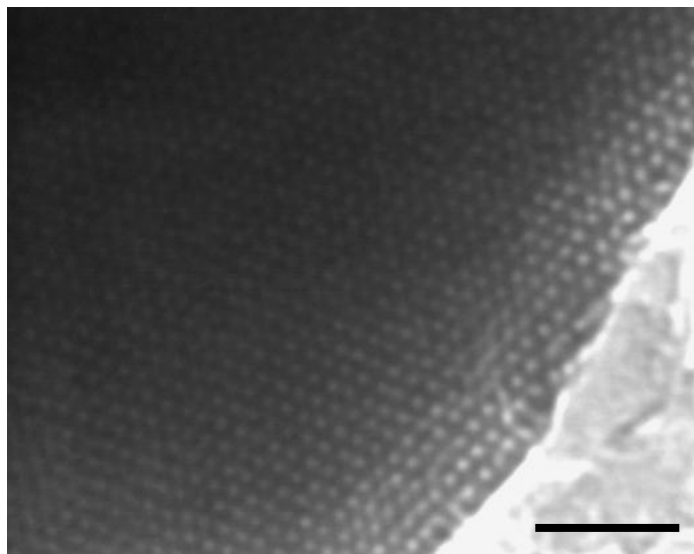
Figure 5.3. Plan view TEM image of 70nm thick silica film coated on random copolymer modified surface. The coating was cast onto a glass slide coated by evaporation techniques with a layer of CaF_2 followed with a layer of amorphous silica. Thermal expansion mismatch caused the silica film to delaminate during calcination. The scale bar is 100 nm.
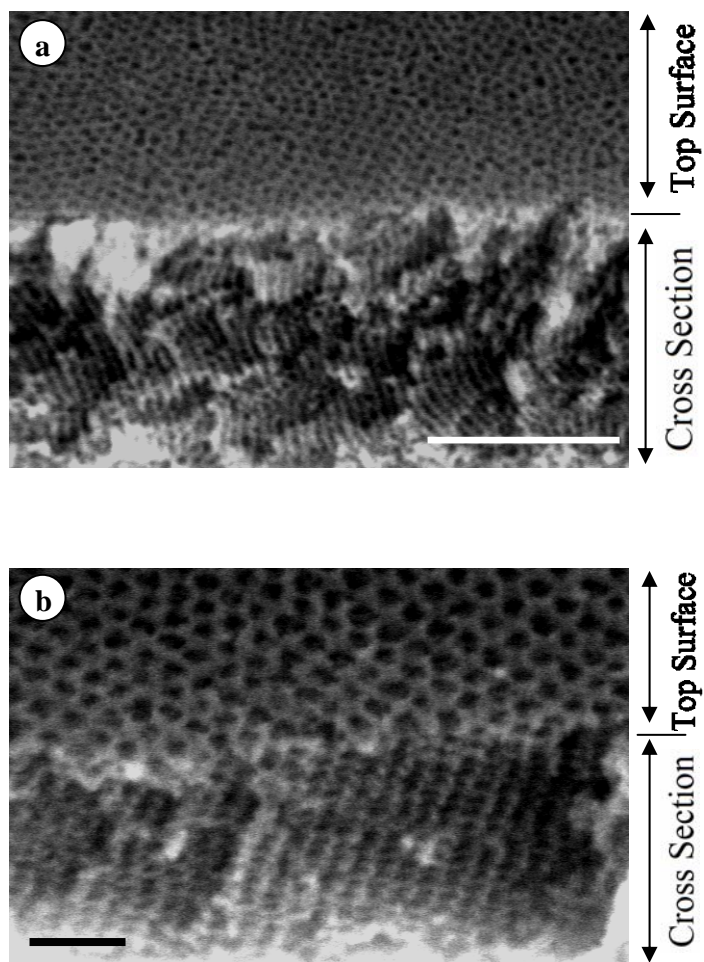
Figure 5.4. SEM images of fractured titania films of different thicknesses: (a) 200 nm thick film confined between two PEO-r-PPO copolymer modified surfaces (scale bar = 100 nm) and (b) 100 nm thick film exposed to air (scale bar = 50 nm). These images were collected by Vignesh Gowrishanker at Stanford University (Palo Alto, CA)

Copyright © Venkat Rao Koganti 2006

Chapter 6 Synthesis and Transport Properties of Orthogonally Aligned Hexagonal Mesoporous Silica Nanofiltration Membranes on Macroporous Supports

6.1.   Introduction

Porous materials are an ongoing area of research due to their advantages in numerous applications, such as chemical and biochemical separations, catalysis, sensors, and nanostructure (e.g. nanowires array) synthesis. Porous ceramic membranes are particularly important because of the broad range of processing conditions under which they can be operated compared to organic membranes. Pore templating of sol-gel materials has recently developed as a common method to synthesize controlled-pore inorganic membranes. For instance, colloidal crystals can be used as templates of ordered spherical macropores, and inorganic precursors can be used to form the ceramic films. Removal of the colloidal particles after condensation of the precursor results in well-defined pores.[222, 237, 238] However, these types of membranes are limited by the sizes of latex particles available (generally ~50 nm to microns) and result in interconnected spherical packings. Anodized alumina membranes are another alternative, in which electrochemical etching of the oxide layer of aluminum is used to produce large uniform arrays of cylindrical pores in chemically and thermally robust films.[239, 240] However, pore sizes are limited to between 10 nm and 100 nm, and anodization does not always yield uniform pores.[241, 242]

The discovery of surfactant templated materials[122, 243] has opened new ways to synthesize ordered mesoporous (pore dimensions between 2 and 50 nm) powders and films.[108, 244] Simple processing and the ability to control the pore size and shape in ceramics makes surfactant templation an attractive method to synthesize mesoporous ceramics. A thin film is a desired morphology for membrane applications. Also, the controllable orientation of pores in thin films makes them better candidates than powders for other applications like sensors, optics, and nanostructure templating. However, in order to use these materials for any of these applications, pore accessibility is essential.

Various research groups have synthesized surfactant templated mesoporous thin films on porous substrates and used them for membrane applications. The majority of the studies concentrated on obtaining accessible pores in surfactant templated mesoporous films – primarily by using bicontinuous mesophase templates. Zhang et. al.[219] and McCool et. al.[218] have used cetyltrimethylammonium bromide (CTAB) to template the pores in silica films on porous alumina supports and conducted gas permeation experiments. 3-D disordered porous networks templated using CTAB served as pathways for the diffusing molecules in the silica membrane. Several research groups have also synthesized ordered bucintinuous Ia3d cubic (MCM 48) films

on porous alumina substrates, and demonstrated their use for gas permeability studies [227], separation of solvents [245, 246] and pressure driven solvent flow experiments [247].

Of the available pore structures in surfactant templated ceramics, the 2-D hexagonal close packed (HCP) cylindrical mesophase is of particular interest because it consists of non-connecting cylindrical pores. 2-D HCP pores provide no alternate paths for the diffusing species between mesopores for applications like membrane separations, catalysis and sensors. An ideal film based on a 2-D HCP phase would have no tortuosity, and thus may facilitate rapid diffusion. Orthogonally aligned cylindrical pores are also excellent templates for arrays of nanoparticles or nanowires. Anodized alumina has been used for this purpose, but surfactant templating provides smaller pores and variable membrane composition.

However, the problem with most HCP films is that favorable (either hydrophilic or hydrophobic) interactions between the substrate surface and the surfactant molecules align the HCP phase parallel to the substrate, thus making these pores inaccessible.[10] Many attempts have been made to control the pore orientation of the cylindrical mesophase in 2-D HCP films, but they often resulted in only partial orthogonal orientation. However, successful methods have been developed. Prouzet and coworkers synthesized inorganic membranes with an accessible HCP mesophase on anodized alumina supports.[248] They found the rare alignment of the cylindrical pores orthogonal to the films, and attributed this to the diffusion of the fluoride ion (used as condensation catalyst for silica) away from the alumina pores. However, because diffusion of the catalyst was the controlling factor for the orientation, this mechanism resulted in a mix of orientations, and the diffusion of the fluoride ion created interconnections between the channels. The same group has also synthesized an ultra filtration membrane using the principle of directed fluoride diffusion. They could not achieve complete orthogonal orientation of the HCP phase and also found that the channels are interconnected.[249] Recently, Kang et. al. modified alumina supports using poly(sodium4-styrenesulfonate) as an ionic linker between the alumina substrate and the silica film.[250] This created mesoporous silica particles on the alumina substrate with HCP phase, but the orientation of the meso channels was not controlled. The random orientation of the silica particles present on alumina support allowed the usage of the membrane for filtration, but transport would only not be as efficient as it could be through an orthogonally oriented film.

Since HCP channels align parallel to hydrophilic alumina surfaces, another way that researchers have tried to synthesize oriented accessible HCP pores by surfactant templating is to synthesize HCP silica inside of the larger pores of anodized alumina (AAO) supports. This could align the HCP pores parallel to the alumina channels, and thus perpendicular to the top surface of the membrane. However, it is also possible for the HCP phase to orient not only

parallel to the alumina macropore surface but also parallel to the film surface to create concentric rings or helical pores. Control over the orientation seems to depend on the size of the alumina macropores, but also is influenced by more subtle synthesis parameters that are not completely understood. Yamaguchi et. al. created HCP orthogonally aligned HCP silica inside of AAO, but the surface orientation effect extends over a limited distance. Distorted cylindrical mesophase was observed far from the alumina wall.[41] Lu et al. were consistently able to prepare orthogonally aligned HCP silica, but they focused on removing the silica from the alumina to generate elongated HCP particles.[42] Wu et. al. prepared orthogonal HCP silica in AAO, but found both experimental and simulation evidence that in confined environment the orientation of the cylindrical channels depends on the degree of confinement.[43] They observed several structures, including helical structures, tubes, and spherical cage-like mesophases upon tightening the degree of confinement inside the pores of anodized aluimina. Also Ku et. al. have observed the formation of intact ring-like pores inside of larger alumina pores, which are inaccessible.[130] Controlling the orientation of the channels in these films by process conditions is only beginning to be understood.[251] Shrinkage of the mesoporous silica away from the alumina walls during drying and calcination often results in gaps that prevent these composite structures from being used as membranes. Ku et al. overcame this problem by using a second step to fill in the gaps with a second phase. However, in a mixed cubic / HCP phase, filtration occurred primarily through the cubic mesophase present in the pores of the alumina but not through the coiled HCP phase.[130] These studies show that while HCP silica can be synthesized inside of the macropores of AAO, the formation of 100% orthogonally aligned HCP silica which completely fills the AAO pores has not been shown.

While preparing HCP silica inside of AAO is an interesting compromise that may eventually lead to orthogonally aligned mesoporous membranes, continuous films would be of more universal utility because they could be deposited on any type of substrate. One route to a continuous film might be to prepare free standing surfactant templated mesoporous films which can be mechanically stabilized on a support. Unfortutately, attempts to synthesize free standing films with HCP mesophase at air-water [252, 253] and oil-water interfaces[254] have yielded either coiled particulate structures of channels parallel to the film, thus making them inaccessible. Free standing 3-D hexagonal silica films have been synthesized to obtain accessible mesoporous membranes, but the problem of interconnected pores still persists.[255]

Recently we have published a report of a simple approach to orienting 2D HCP mesoporous silica films orthogonal to non-porous substrates.[50] We used the polyethylene oxide (PEO) – polypropylene oxide (PPO) - PEO triblock surfactant P123 as a pore template, which has an average composition $HO(C_2H_4O)_{20}(C_3H_6O)_{70}(C_2H_4O)_{20}H$. By analogy with successful

approaches to the orientation of HCP block copolymers normal to substrates, we modified glass slides by cross linking a thin film of PEO-PPO random copolymer on their surfaces, or by cross linking a thin film of P123 itself on their surfaces. Both of these modification procedures will result in chemically neutral surfaces for the P123 templating agent which we used. We prepared 240±5 nm thick films, and showed that it was essential to sandwich the films between two modified surfaces to completely align the HCP mesophase so that it is tilted orthogonal to the substrate. We have also synthesized thinner films (thickness <100 nm) on similarly modified surfaces and found that the thinner films do not need another modified surface to tilt the HCP pores in the silica films.[29] Using X-Ray Diffraction (XRD) and Transmission Electron Microscopy (TEM) evidence we suggested that there exists a critical thickness between 70 and 100 nm below which the HCP cylinders are tilted normal to the substrate surface across the entire films thickness. Above the critical thickness we found random orientations of the mesophase towards the air-film interface. This approach can be easily generalized because the crosslinked copolymer can be deposited onto any nonporous substrate, or can even be loaded into a porous substrate to allow a continuous film to be deposited over the pores. Here, we demonstrate that the use of crosslinked PEO-PPO films as chemically neutral layers can be extended to permit the formation of continuous, orthogonally tilted HCP (o-HCP) silica films on porous supports. These oriented mesoporous films of different thicknesses will be deposited on commercially available macroporous AAO supports (pore diameter of ~200 nm). Liquid permeability experiments will demonstrate pore accessibility and uniformity. Permeability of different sized gold particles will show that the membranes are defect-free and can be used for size-based separation. This approach to the synthesis of supported mesoporous films can be generalized to any film composition (such as mixed oxides, zirconia, titania, etc.), any type of macroporous support on which the mesoporous film is stable, and because no sandwiching is required (for thinner films), any porous support geometry (such as tubes) can be employed.

6.2.   Experimental Section

Thin mesoporous silica films on glass substrates were synthesized as described previously.[50] Commercially available anodized alumina membranes (Anodisc membranes (pore size ~ 0.2μm) from Whatman) were modified by dip coating and crosslinking either P123 (Aldrich) or random PEO-r-PPO copolymer (25 wt% PPO, Aldrich). To a solution of 0.415 mM random copolymer in acetone was added a drop of glycerol to act as a crosslinker. An equimolar amount of 1,6-diisocynatohexane (DH) was then added drop wise to this mixture under constant stirring. The resulting solution was dip coated onto anodiscs and the anodiscs were aged at 120 ºC overnight

to drive the isocyanate-hydroxyl reaction to completion. The same procedure was used to cross link P123 using 0.696 mM of the copolymer.

The mesoporous silica coating solution was prepared by addition of a solution of P123 to a prehydrolyzed silica sol following the procedure of Brinker et al.[108] First, tetraethoxysilane (TEOS), anhydrous ethanol, deionized ultrafiltered water and HCl (mole ratio 1 : 3.8 : 1: $5*10^{-5}$) were refluxed at 70 ºC for 90 minutes. Then, the remaining water and HCl were added, increasing the concentration of HCl to 7.34 mM. After stirring this mixture at 25 ºC for 15 min, the sols were aged at 50 ºC for 15 min. The required amount of P123 was dissolved in ethanol and this solution was added to the above aged silica sol with constant stirring. The final mole ratios were 1 TEOS : 22 C_2H_5OH : 5 H_2O : 0.004 HCl : 0.01 P123. Slides were dip coated with this sol at a withdrawal speed of 7.6 cm/min. Thickness of the films was adjusted by adding anhydrous ethanol to the fresh sol to dilute all ingredients to produce thinner films.

After deposition, some films were sandwiched with another modified substrate that was prepared with isocyanate crosslinking as described above. Characterization of the structure of thicker sandwiched films (thickness ~ 240nm) and thinner non-sandwiched films (thickness < 100 nm) on glass substrates are published elsewhere.[50, 256] Here we report the permeability results for thicker (thickness ~ 240 nm) and thinner films (< 200 nm) on modified alumina membranes. After coating with undiluted sols, relatively thick silica films (thickness ~ 240nm) were prepared. An identically modified AAO membrane was placed in contact with both the sides of the freshly coated membrane. Films were also prepared on modified AAO which were not sandwiched, and all of the thinner films prepared from sols diluted with ethanol were not confined between two modified surfaces. Coated alumina membranes were aged and dried at 45 ºC for 24 hr and at 100 ºC for 24 hr. Films were calcined in air at 500 °C for 4 hrs to remove the surfactant and the cross linked copolymer. The temperature ramp rate was 0.5 °C/min.

The thickness of each film was estimated by measuring the thickness of films coated from the same sols onto silicon wafers, using a Gaertner 7109-C-338G ellipsometer. Permeability of the silica membranes was measured by conducting liquid (ethanol) flow measurements using a filter holder assembly (Fisher). Pressure was varied across the membrane and flux was measured for various pressure drops. Different sized gold particles (20nm and 5nm) were passed through membrane to see if the flux observed in the liquid flow measurements is due to flow through the pores of the silica membranes or because of defects which might have developed during calcination. UV/vis spectra of gold nanoparticle solutions before and after filtration were collected using an Ocean Optics USB/SS UV/vis spectrometer.

P123 (BASF), TEOS (>99%, Fluka), deionized ultra filtered water (Fisher), anhydrous ethanol (Aaper Alcohol & Chemical), acetone (HPLC grade, Fisher), glycerol (99+%, Aldrich), DH

(98+%), and random copolymer (75% EO, Mn ~ 12000, Aldrich) were all used as received. The AAO supports were obtained from Fisher Scientific.

6.3.   Results and Discussion

We have previously demonstrated that the sol described above (with P123 template) yields silica films of thickness 240±5 nm with well ordered 2-D HCP cylindrical mesophase on unmodified glass slides.[50]   Completely orthogonally tilted 2-D HCP (o-HCP) mesophase was obtained by confining the 240nm thick silica film between two PEO-r-PEO or PEO-b-PPO copolymer modified surfaces before calcination.[50] We describe these films as orthogonally *tilted* because while GISAXS with a 2D detector shows a prominent spot in the plane of the films due to perfectly orthogonal domains, streaks extending away from these spots indicate a (narrow) distribution of tilt angles away from orthogonal.[256] We have also shown that thinner films (thinned by diluting the sol with various amounts of ethanol) on similarly modified glass substrates also yield orthogonally tilted channels when the thickness less than 100 nm.[256] Using XRD and TEM data the critical thickness was estimated to be between 70 nm and 100 nm. Below the critical thickness, sandwiching the coated slides is not necessary because the orientation from one chemically neutral surface is able to propagate across the entire film. Here we establish that this idea can be used on porous substrates as well, and confirm the pore accessibility using permeation and filtration experiments. The membranes on anodisc supports are prepared by a straightforward coating procedure, and the coated anodiscs are simply cured and calcined in ambient air. In the interest of brevity, the results for films coated on supports modified by cross linking random copolymer are presented here. Substrates modified by cross liking P123 also show identical orientation and permeation effects.

To be able to utilize silica films with o-HCP pores as membranes, to assess the continuity of the films, and to confirm the accessibility of the pores, the modification procedure used for nonporous substrates was extended to Anodisc substrates. The crosslinked PEO-r-PPO modifier is hypothesized to block the Anodisc pores temporarily so that a continuous film of silica can be deposited. Macroscopically P123-templated defect-free silica films of varying thickness were deposited onto modified Anodisc membranes.   Two cases of particular interest are the 240 nm thick o-HCP silica film on a PEO-r-PPO modified Anodisc which was sandwiched between two modified surfaces before calcination; this will be referred to as MEM-1. A o-HCP membrane prepared by drying and calcination in air (without sandwiching) of a 70 nm thick silica film cast onto PEO-r-PPO modified porous alumina will be referred to as MEM-2. These thickness values are those of films coated on silicon wafers from similarly diluted sols. To illustrate that a silica membrane was indeed deposited at the top surface of the Anodisc, Figure 6.1 compares plane-

view SEM images of anodized alumina without any silica film on top and anodized alumina with mesoporous silica film (thickness ~ 240nm) on top of it. The silica-coated Anodisc exhibits greater scattering of electrons from the whole surface than the uncoated Anodisc, leading to a decrease in the contrast of the image. This appearance is consistent with a uniform silica film on top AAO membrane is uniform without any defects. Thinner silica membranes do not show this difference because they are electron transparent. Thinner sections of the 240-nm thick film also appear darker, but nanoparticles filtration experiments (below) confirm that these regions are not cracks.

Ethanol flow measurements through the Anodisc-supported o-HCP membranes confirms a level of permeability consistent with the orientation of the pores. Fig. 6.2 shows the flux vs. pressure drop for the MEM-1 and MEM-2 membranes. The flux varies linearly with pressure drop, suggesting that flow occurs through pores of uniform size. As we would anticipate, the thinner films (MEM-2) have higher flux than thicker films (MEM-1). The Hagen-Poisseuille equation (eq. 1) is used to interpret these data:

$$J = \frac{\varepsilon r^2 \Delta p}{8 \mu L} \qquad \text{eq. 1}$$

where J is the flux observed, ε is the porosity of the silica membrane (calculated based on the refractive index of the films measured to be 0.5), Δp is the pressure drop, μ is the viscosity of ethanol and L is the length of the flow. When using this equation, it is assumed that the entire pressure drop is due to the pores in silica film and that the alumina membrane does not offer any resistance for the ethanol flow.

With eq. 1, the pore diameter is estimated to be approximately 4 nm for the 70 nm thick film and 3.5 nm for the 240 nm thick film. Based on the d-spacing of the (100) peak in XRD patterns in the case of parallel oriented cylindrical pores (5.5nm), pore size was approximated to be slightly less than 5.5nm (after subtracting the estimated wall thickness from the unit cell parameter).[28, 29] We have confirmed by nitrogen adsorption of films prepared with the sol composition and cast on glass cover slips that the pore diameter is 5.4 nm. The agreement of the flow results with this value is very good, considering that the Hagen-Poiseuille equation neglects entrance effects and the effects of any boundary layer on the flow. When using the Hagen-Poisseuille equation, it was assumed that the resistance to flow comes only from the silica film, and that the alumina membrane offers no resistance. This is reasonable because of the pore size of alumina pores is described by the manufacturer to be 200 nm, which is approximately 50

times that of the silica pores. To confirm this, flux measurements with uncoated Anodisc supports were attempted, but the flow was so much faster than it is through the silica membranes that it was difficult to measure accurately.   For these calculations, the length of the channels is approximated to be twice the thickness of the silica film because silica film is present on both the sides of alumina membrane. The silica film might have slightly sunk into the pores of alumina membrane during calcination in which case the actual length of flow is more than the value that we used and hence the actual pore size is slightly more than the above calculated numbers. Also this approximation for the length of flow might have led to the difference in the pore diameter calculated for the two thicknesses because the extent of penetration of the silica into the AAO pores might be different for different thicknesses. Given the uncertainties about the geometry of the pores, the agreement of the x-ray, nitrogen adsorption and permeation experiments is excellent.   This agreement is consistent with the films being defect-free; if there were a large number of large defects in the silica films, then we would have expected significant differences in the pore diameters estimated by the Hagen-Poisieulle equation and other methods.

Fig. 6.3 illustrates the observed ethanol flux vs. thickness of silica membranes for a fixed pressure drop of 6 in. Hg across the membrane. As expected, the flux increases as the thickness decreases for the air-cured (non-sandwiched) films. The Hagen-Poisieulle equation predicts a reciprocal relationship between flux observed and the thickness of the film when other parameters are held constant. We do not see an exact reciprocal relationship between the flux and thickness even for the first three thicknesses (50, 70 and 125 nm). This can attributed the possibility that as the thickness increases, more defects can occur, leading to changes in the orientation of the cylindrical channels and the presence of a small amount of tortuosity which is not accounted for in the Hagen-Poisieulle equation. X-ray diffraction of films on glass slides shows a critical thickness near 100 nm above which intensity begins to appear. This intensity indicates that there are domains oriented parallel to the substrate, which would be expected to impede flow in a membrane. A 240 nm thick membrane prepared without being confined between modified surfaces shows hardly any permeability at all. For the case of films of thickness 240 nm we clearly see that sandwiching the membrane between modified surfaces is necessary to tilt the pores orthogonal to the substrate through the entire thickness and hence to obtain permeability through the membrane. When this is done, the flux for the 240 nm sandwiched film and the fluxes of the thinnest two non-sandwiched films fall on a single curve consistent with the Hagen-Poisieulle equation (the curve in Fig. 6.3). When AAO membranes modified with crosslinked PEO-r-PPO were coated with a silica sol without any surfactant template and calcined, the ethanol flux was essentially zero within the range of pressures and

flowrates that we could access (results not shown). Without surfactant templation, a microporous silica membrane would be expected to form from an acidic sol, with a low amount of porosity. This observation confirms that the flux observed for the case of aligned mesoporous films is due to the mesopores templated by the surfactant mesophases and that the flux through the micropores present in silica matrix is negligible. HCP films with the pores aligned parallel to the substrate present the same type of microporous silica barrier, and this is why the non-sandwiched 240 nm thick films show such a low ethanol flux.

While the solvent permeation experiments are consistent with the pore size expected in the film, it is difficult to be completely certain that the results are not a result of an increase in nanometer-scale defect density as the film thickness decreases. To confirm that the permeation results are due to flow through uniform mesopores, we performed filtration experiments using 20 nm and 5 nm gold colloids. Fig. 6.4 shows the UV/vis spectra of 20 nm colloidal gold solution before and after filtration through MEM -1. The peak at around 525 nm is characteristic of the colloidal gold. The absence of this peak in the filtrate clearly shows that 20 nm gold was completely filtered out by the ~5 nm silica pores. To check the accessibility of the pores for smaller particles, 5 nm gold colloidal solution was passed through the same membranes and the UV/vis spectra are compared before and after filtration in Fig. 6.4 for MEM-1. Again, the peak at around 525 nm is monitored for the presence of colloidal gold particles. These spectra show that a significant fraction of the 5 nm gold particles pass through the membrane. We attribute the slight decrease in the intensity of the peak at 525nm to the fact that the particle size distribution in the colloidal gold solution is not perfectly monodisperse; the larger particles in the distribution may be too large to pass through the o-HCP silica pores. The above two experiments with different sized gold particles clearly show that the silica film is defect free at the nanometer scale. Similar gold filtration experiments done using MEM -2 are shown in figs. 6.5 & 6.6. Fig. 6.5 shows the data before and after passing a 20 nm gold solution through the MEM-2 sampe. It shows that the 20 nm gold particles are completed filtered out by the exceptionally thin membrane MEM-2. Fig. 6.6 shows UV/vis data for 5nm gold colloidal solution before and after filtration with MEM-2. Figs. 6.5 & 6.6 show that the pores of MEM -2 are accessible to gold particles that are smaller than 5 nm, where as the membrane completely blocks the particles whose nominal diameter is 20 nm. These gold filtration data once again confirm that the silica membranes on anodized alumina supports are defect free. When the thickness of silica film is 50 nm we observed that a significant amount of 20 nm gold particles passed through the membrane (data not shown). This might be because of defects which might have developed during calcination. At this point, we suspect that there exists an optimum thickness below which the silica membrane on the top of anodisc develops defects during calcination. Our results suggest

that 70 nm might be the optimum thickness where the film has cylindrical pores aligned perpendicular to the substrate and is also uniform. Films that are less than 70 nm thick are slightly defective and allow the 20 nm gold particles to pass through.

The above results show that the idea of the aligning cylindrical channels perpendicular to non-porous substrates with chemically neutral surface modification can be successfully extended to porous supports. The use of a crosslinked PEO-PPO layer in the process of preparing the templated silica films allows this approach to be generalized in this manner. The thickness of the silica films on the top of modified substrates is an important parameter to prepare defect free, aligned films. Above a certain critical thickness (between 125 and 70 nm in this study) we see 2D HCP mesophase aligning parallel to the surface, which is evident from very low permeabilities for films on porous supports. This thickness is consistent with the value of ~100 nm observed in previous structural characterization studies. For films less than 70 nm thick, we find evidence that while the permeability is high, the films are more prone to form defects during processing, and as a result, the films are not able to filter 20 nm gold particles.

6.4. Conclusions

We have demonstrated here that it is possible to extend the synthesis of mesoporous thin silica films with orthogonally tilted 2-D hexagonal close packed (o-HCP) mesopores from non-porous glass/silica substrates to porous (anodized alumina) substrates. The alignment is promoted by using a chemically modified surface which is equally attractive to the polar and nonpolar regions of the silica-surfactant mesophase that forms shortly after dip coating. Because this chemically neutral layer is formed by crosslinking hydroxide-terminated PEO-r-PPO or P123 copolymers, a porous substrate can be filled / coated with the neutral layer, and then coated with a silica sol.

As previous studies on non-porous substrates have shown, the film thickness has a large impact on the success of the process. Thicker films (thickness ~ 240nm) have to be confined between two modified surfaces to be fully aligned, whereas thinner films (thickness < 100 nm) need not be confined to obtain complete alignment of the cylindrical mesochannels. XRD patterns suggest that we have completely tilted o-HCP phase in both thin[256] as well as thicker films[50] coated on modified surfaces.

When deposited on porous supports, the mesoprous films can be used as membranes. Accessible, uniform films that are 240 nm and 70 nm thick have been deposited on top of porous alumina supports. This idea can be successfully extended to any porous or nonporous substrate (including arbitrarily curved substrates). This idea of neutral surface aligning the 2D HCP cylindrical mesophase results in mesoporous films on the top of porous substrates rather having cylindrical pores inside the pores of porous substrates.[41] This overcomes the difficulty sometimes

found with mesoporous silica of forming helical or ring-shaped pores when confined inside of anodized alumina pores.[43] High permeability of ethanol in the orthogonally aligned silica membranes confirmed the accessibility of the pores. The uniformity of the silica membranes was demonstrated by passing gold colloids of different sizes. UV/vis data showed that 20 nm particles are filtered out while particles close to 5 nm in diameter passed thorough the orthogonally aligned silica membranes. Thicker sandwiched films are completely defect free. In the case of thinner non-sandwiched films, there appears to be an optimum thickness giving both orthogonally aligned pores and films without nanometer-scale defects. Films that are thinner than the optimum thickness develop defects during calcinations which are indicated by their inability to filter 20 nm gold nanoparticles. In the future, these films should be useful for size based separations of macromolecules including inorganic colloids and proteins. In addition, the o-HCP channels should find numerous applications in the areas of sensors and catalysis.

(a)   (b)
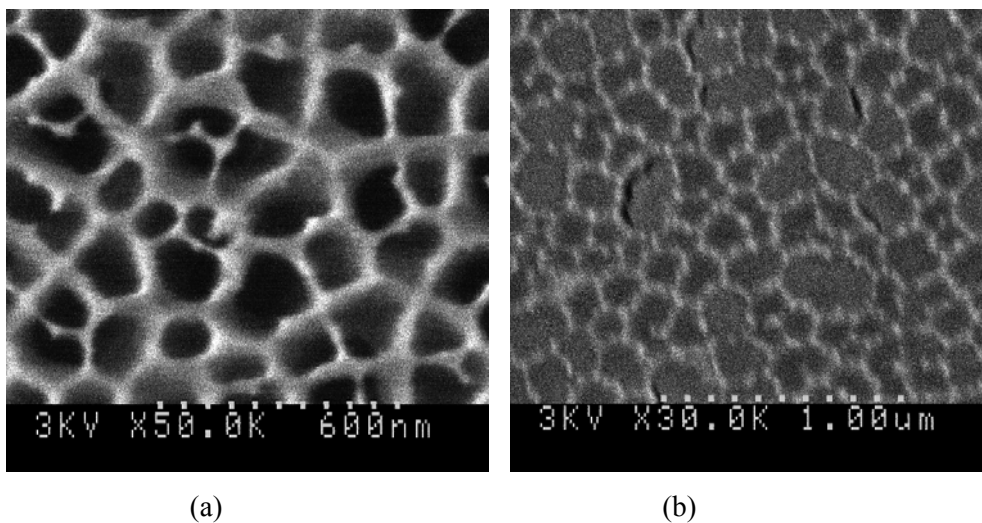
Figure 6.1. SEM image of (a) as obtained anodisc, (b) anodisc with 240nm silica film on top (silica film is calcined).
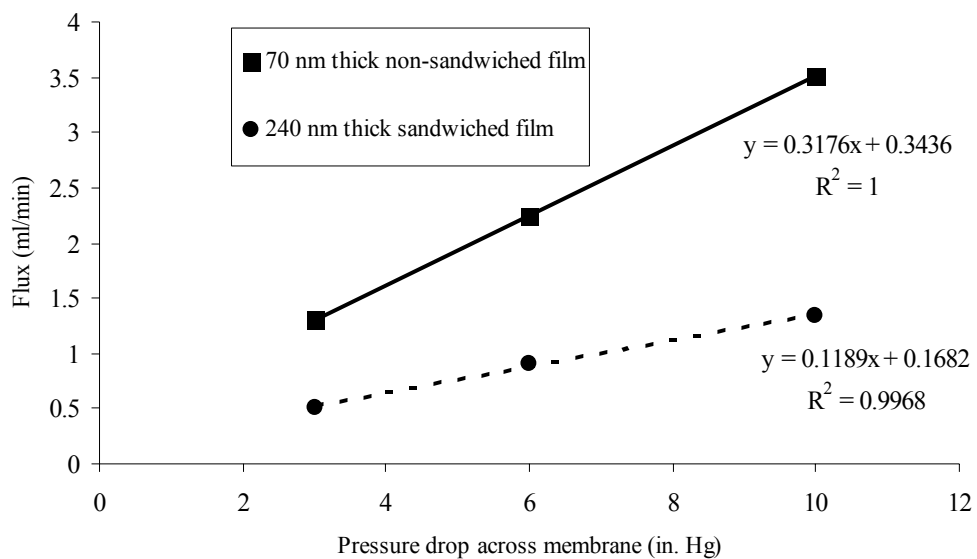
Figure 6.2. Ethanol flux vs. pressure drop across the membrane for different thickness
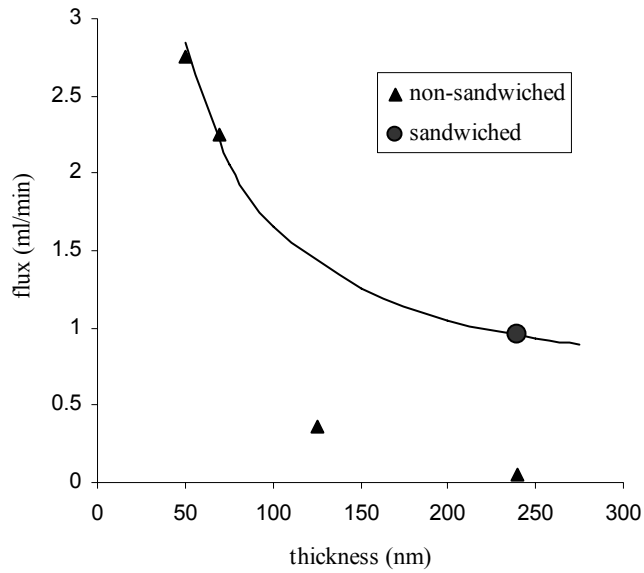
Figure 6.3. Ethanol flux vs. thickness at a pressure drop of 6 in. Hg across the membranes
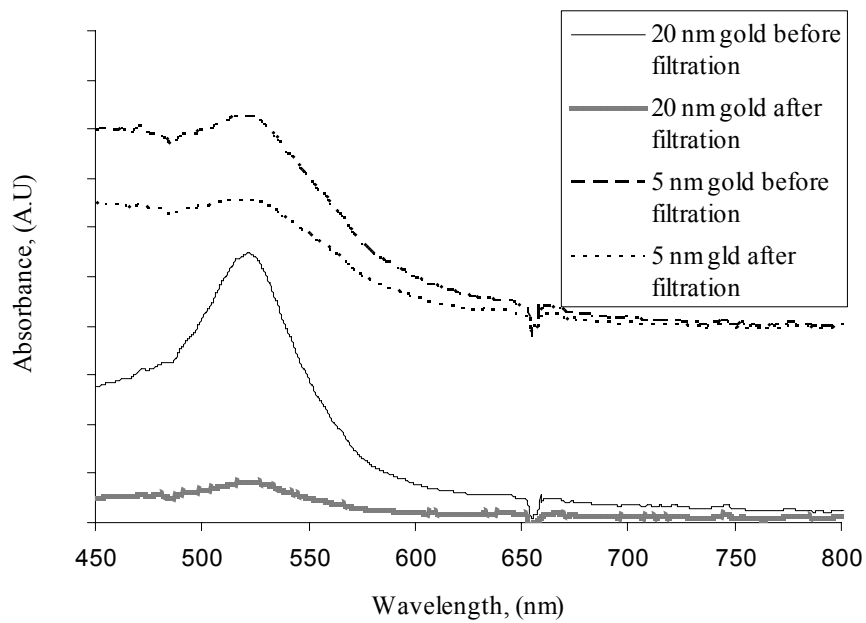
Figure 6.4. UV-vis data of 20nm and 5nm colloidal gold solution before and after filtration through MEM -1

96
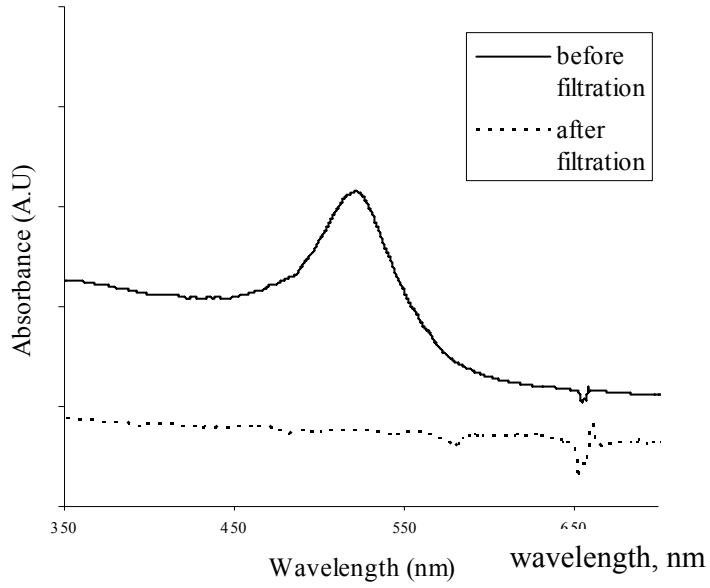
Figure 6.5. UV-vis data of 20nm colloidal gold solution before and after filtration through MEM -2
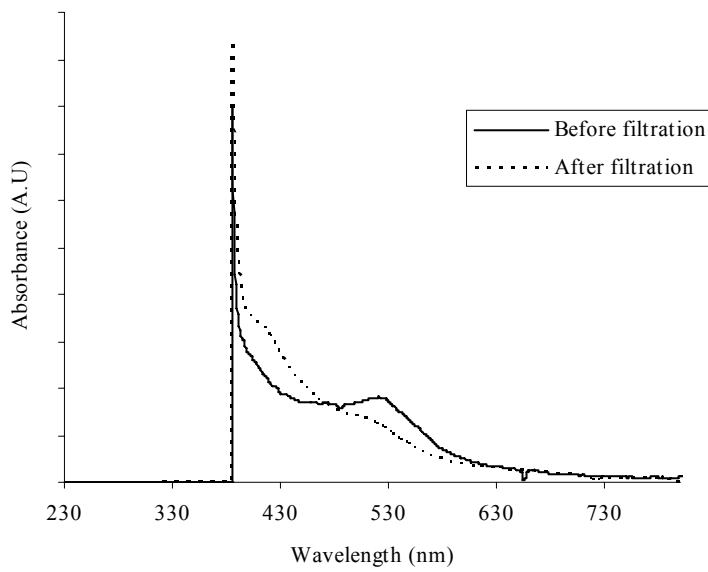
Figure 6.6. UV-vis data of 5nm colloidal gold solution before and after filtration through MEM - 2

Chapter 7 Surfactant Templated Mesoporous Nanocrystalline Titania Films with Orthogonally Aligned Cylindrical Nanopores

7.1. Introduction

The introduction of nanocrystalline titania thin film electrodes for photoelectrochemical cells by Grätzel and co-workers has highlighted the importance of research in the synthesis of nanostructured titania films because of their potential applications in the areas of electrochromic devices, photocatalysts, sensors etc.[257, 258] These thin film electrodes have surface areas that are approximately 3 orders of magnitude higher than flat electrodes and thus can increase the efficiency of absorption and utilization of photon energy.[259] Mesoporous, nanocrystalline titania is a promising alternative to many existing materials to fabricate electronic devices and also in the area of environmental applications.[259, 260] High surface areas of mesoporous materials along with several other characteristics like easily tunable and functionalizable pore dimensions make these materials important in several applications. Excellent charge transport properties of mesoporous titania have been demonstrated in the liquid electrolyte dye-sensitized solar cell.[257] Hexagonal close packed cylindrical channels are an important geometry for infiltration with electronically conductive organic polymers because several studies have shown that the transport, absorption, and emission properties of these polymers can be tuned to great advantage inside of HCP pores.[261, 262]

Surfactant templation combined with inorganic precursor chemistry results in well ordered mesoporous materials with controllable pores sizes and geometries. These materials were originally synthesized in the form of powders,[59, 122] but applications in the areas of membranes, electronic materials, sensors etc. benefit more from a thin film geometry. In 1997, Brinker et. al. synthesized these mesoporous materials in the form of films using the Evaporation Induced Self Assembly (EISA) process.[64] Dip coating substrates from a solution containing inorganic precursors, surfactant and solvent accompanied by rapid evaporation of volatile solvents (ethanol and water) results in ordered mesostructures within minutes after film deposition. Silica films were synthesized initially using surfactant templation. Since then, several research groups have synthesized a variety of pore geometries in silica films and developed applications of these films in a variety of areas.[53, 220, 227, 245, 247]

The amorphous and electrically insulating nature of silica limits the application of silica films to areas like membrane separations, adsorbents, low-k dielectric layers, and so on. Electrical conductivity of the inorganic frame work is essential for applications as components of electronic materials. As discussed above, titania is an excellent alternative material. Unlike silica, titania can crystallize into the anatase phase which acts as an n-type semiconductor.

98

Using surfactant templation techniques analogous to those used for silica, we can synthesize mesoporous titania from solution based precursors. The chemical, photoactivity and electronic advantages of titania over silica have made surfactant templated titania films an expanding recent area of research, and several interesting applications of titania films have been realized in the areas of photovoltaics, photocatalysis, etc.[263, 264]

Working with titania precursors is more difficult than silica precursors because of their high reactivity. In classical sol-gel titania precursors (e.g. titanium (IV) ethoxide and titanium (IV) n-butoxide) the oxidation state of the metal is smaller than its preferred coordination number. To increase its coordination number the metal uses its vacant d orbitals to accept lone pairs from nucleophilic ligands. A typical abundant nucleophile is the oxygen atom of water, and the ability for coordination expansion of titanium makes these precursors very reactive. In addition, transition metals can form M-OH-M bridges through olation reactions, leading to rapid precipitation of hydroxyl species under uncontrolled conditions. To inhibit the condensation of the titania precursors and to allow time for self assembly to occur, we use protons (H^+ ions) as inhibitors.[265] Several studies have concentrated on controlling the hydrolysis and condensation of the titanium alkoxides to favor gelation vs. precipation.[265-268] Although different ligands (such as acetylacetonate) can be used as inhibitors, they can interfere in the interactions between titanium species and surfactants, so it is common to use H^+ as inhibitors in the synthesis of surfactant templated mesoporous titania films.[126, 231, 269, 270]

There have been several studies reporting the synthesis of mesoporous, nanocrystalline titania for a variety of applications. Control of synthesis and curing conditions is extremely important for mesoporous anatase films. As discussed above, highly acidic conditions are usually used to slow down the condensation rate. Another important parameter is the relative humidity (RH) of the environment in which these films are cured. It is important to age the as-deposited films in a highly humid environment. A humid environment slows down the evaporation of the solvents from the films, thus providing additional time for rearrangement of titania species and also for the mesoscopic ordering of the surfactant.[231, 270-273] Crepaldi et. al. report on complete synthesis and characterization procedures to obtain ordered mesoporous titania films.[274] They discuss all important chemical and processing parameters important for reproducible construction of mesoporous titania thin films. Jang et. al. study the effects of pH of the coating sol as well as the humidity of the curing environment on the mesostructure of titania films obtained.[275] They suggest an optimum pH (~ -0.6) and humidity (~ 80% RH) values to synthesize highly organized mesoporous titania films.

Calcination of the surfactant molecules removes the surfactant and also induces anatase crystallization. Formation and growth of these anatase nanocrystallites gradually destroys the

99

mesoporous order due to modifications of the valence state of the transition metal via redox reactions and also extensive atomic rearrangement.[269] Using in-situ x-ray diffraction studies Tolbert et. al measured the crystallization kinetics of mesoporous titania films.[231] They measured activation energies for anatase crystallization and mesopore loss, and found optimum conditions for production of crystalline walls with minimal loss of mesoscopic order that require short calcination times at high temperatures. In this study we follow similar calcination procedures to achieve both mesoporous and nanocrystalline titania films. Ozin et. al also studied the evolution of nanocrystallinity in periodic mesoporous anatase films.[276] Although they did not comment on reduction of mesoscopic order during the crystallite formation, they observed a 1D diffusion controlled growth mechanism of anatase crystallites that are aligned along the axis of the HCP cylinders. In this study (as will be discussed later) we did observe a dependence of mesoporous order upon calcination temperature similar to the results of Tolbert et. al.[231] and unlike Ozin et. al.[276]

Using highly acidic conditions that slow down the condensation rate of titania precursors, several 1D, 2D and 3D pore geometries have been synthesized in titania films.[273, 275, 277, 278] Of all these pore geometries the 2D Hexagonally Close Packed (HCP) arrangement of cylindrical meso channels is interesting because of its simple geometry (making it easy to model convection, diffusion and reactions happening in these pores) and non interconnecting pores. Until recently scientists in this area of research have been trying to address a major technical challenge: the EISA process usually aligns the HCP mesophase parallel to the surface. Preferential interactions between the substrate surface and surfactant molecules align the HCP mesophase parallel to either hydrophilic or hydrophobic substrates. Orthogonal alignment of the HCP phase is essential to utilize the films for all applications requiring accessible pores. Inspired by molecular simulations, we recently aligned the HCP mesophase in silica films orthogonal to the surface by coating chemically neutral surfaces with the silica sol (Chapters 4-5).[50, 207] By cross linking a layer of random copolymer on the substrate surface and using this modified surface to coat the silica films, we have eliminated all preferential interactions between the substrate surface and surfactant molecules, resulting in orthogonal alignment of the HCP mesophase. In this work we use the same idea, and by using a titania precursor, we obtain orthogonally aligned HCP mesophase in titania films. These films are characterized by XRD, TEM and SEM.

After confirming the existence of oriented channels in the films we utilize these films to fabricate a hybrid heterojunction solar cell by infiltrating the pores with a semiconducting polymer, regio-regular poly(3-hexylthiophene) (P3HT). It has been recently shown that surfactant templated films can be infiltrated with P3HT.[261] Photovoltaic properties of this type of cell have also been reported, although these studies utilize cubic mesoporous films because of

the lack of availability of oriented cylindrical mesophase.[264] In an article on bulk heterojunction photovoltaic cells, McGehee has described the importance of the oriented cylindrical mesophase to achieve higher transport of the charge carriers in an organic-inorganic heterojunction solar cell.[279] He also reviews the status of conjugated polymer photovoltaic cells where he emphasizes the need for materials with better structural order which can provide better transport of charge carriers to fabricate high efficiency conjugated polymer photovoltaic cells.[280] We will also discuss the efficiencies of the bulk heterojunction solar cells that we fabricate by infiltrating hole conducting P3HT polymer into the pores of the titania films.

7.2.   Experimental

The films in this work were coated onto borosilicate glass substrates (some of which are coated with a thin film of fluorine-doped indium tin oxide, FTO). Before coating, all of the substrates were cleaned with deionized water, acetone and isopropanol. Following the procedure described elsewhere, some of these substrates were modified by cross linking a random copolymer on their surfaces using 1,6-hexyldiisocyanate and glycerol.[50] After aging these modified glass slides at 120 °C overnight, the crosslinking of the random copolymer was considered complete.

The coating sol was prepared by dissolving 0.65 g of P123 in 6 g of anhydrous ethanol. In a separate beaker, 2.1 g titanium (IV) ethoxide was added to 1.53 g of conc. HCl (~ 36 wt%). After stirring this mixture for about 10 min, it was mixed with P123 solution and stirred for another 10 min. This sol was used immediately for coating the glass slides. As described previously, both unmodified and random copolymer modified slides were coated with titania sol. Slides were dip coated at 7.6 cm/min. After coating a modified slide, an identically modified slide was kept in contact with this freshly coated slide to promote the orientation of the HCP phase through the entire thickness of the film.

After coating, humidity of the curing environment for the coated substrates had to be maintained at a high level. Following the procedure described by Tolbert et. al., we aged the coated films in a sealed container with an open beaker of water kept in the container to maintain a high RH.[231] The entire container was kept in the refrigerator maintained at a temperature of ~ 5 °C. The films were aged under these conditions for 2 hr. These aged films were then calcined at 400 °C. The temperature was increased at a rate of 25 °C/min and the slides were kept at 400 °C for 10 min.

Thr thickness of the calcined films was measured using a Dektak 6M stylus profilometer. The calcined films were then characterized using XRD, TEM and SEM to confirm the presence of oriented HCP channels in nanocrystalline titania walls. XRD patterns of the films were

collected on a Bruker Discover D8 diffractometer operated at 40 mV and 40 mA. Glass slides were mounted on the XRD stage without any processing. TEM images and Electron Diffraction (ED) patterns of the titania films were collected on a JEOL 200FX microscope operated at 200 KV. Samples were prepared by scraping the titania film off the glass slides using razor blades. The powder scraped off of the substrate was suspended on a TEM grid and observed by TEM. In order to observe the orientation of the cylindrical channels the titania films were also imaged under SEM. The substrates were fractured to collect both plan view and cross sectional images. The conductivity of nanocrystalline titania helped us to obtain SEM images by allowing imaging without any metal deposition on the samples (this usually obscures imaging of 5 nm pores). Scanning Electron Microscopy (SEM) images were collected on FEI XL30 Sirion SEM with FEG source operated at an accelerating voltage of between 3 and 5 kV at Stanford University.

After confirming the presence of vertically oriented channels in the titania films these films were used to fabricate bulk heterojunction soalr cells. To fabricate the solar cells we used FTO-coated slides as the substrates. The FTO serves as the bottom electrode. A layer of non-templated titania was first deposited onto the FTO. 2.1 g titanium (IV) ethoxide was added to 1.53 g of conc. HCl (~ 36 wt%) and stirred for 10 min. Then 8 ml of ethanol was added to the above mixture and stirred for another 10 min. Substrates were coated with this solution and heated at 450 °C for 1 hr. The thickness of this titania layer was 60±5 nm. This layer was deposited to ensure that the P123 used in the subsequent stages cannot come into direct contact with the bottom FTO electrode.

Mesoporous titania films were then deposited on top of these substrates using the procedure described above to achieve orthogonally aligned cylindrical channels. The mesoporous titania film thickness was maintained at around 100 nm by diluting the coating solution with ethanol. During the synthesis stage the films were sandwiched between two modified surfaces to ensure complete alignment of the channels through the entire film thickness. After calcination, the films were ready for polymer infiltration. For comparison, solar cells were also fabricated using non-templated titania films. This resulted in solar cells with a layer of non-templated titania beneath a layer of P3HT. These are the first generation bilayer heterojunction solar cells.[280]

P3HT solutions for infiltration were prepared as follows. The polymer used was regio-regular poly-3-hexylthiophene (P3HT) purified by Soxhlet extraction. A required amount of P3HT (~20 mg) was placed in a glass vial with a stir bar and a controlled quantity of tetrahydrofuran (THF, ~2 ml) was added. The mixture was heated at 60 ˚C and stirred, on a hot-plate, for a few hours to ensure dissolution. About 20 mg of P3HT in 2 mL of THF yields films of 100 nm thickness when spin-coated at 2000 rpm.

P3HT was infiltrated into the pores of the titania using the procedure described by Coakely et. al.[261] Polyimide (thermosetting polymer) was applied on one side of the titania. This protects the device from damage and possible shorting when the leads are clamped on. The substrates were cleaned in UV-ozone for 30 minutes to remove carbonaceous deposit on top of the titania and to expose the surface of the titania. The substrates were transfered into a glove-box immediately. All subsequent steps occured inside the glove-box. The P3HT polymer solution was the spin coated onto the substrates as described in the previous paragraph. In the case of mesoporous titania, a 100 nm film of P3HT was enough to provide for sufficient polymer for subsequent infiltration into the pores. In the case of flat titania for bilayer solar cells, the thickness was around 50 nm. For mesoporous titania samples a melt infiltration step was needed for the polymer to infiltrate the mesopores, in which the films with polymer were heated at 200 ˚C for between 2 to 8 minute, on a hot-plate and then allowed to cool slowly. Some of the polymer from the film was expected to infiltrate into the pores. The amount of infiltration depends on the pore-size, molecular weight of the polymer, temperature and time of infiltration. The excess polymer on top of the pores was then washed off by dripping solvent onto a spinning sample. Polymer that was within the pores should not have been washed off. A fresh overlayer of polymer solution was then deposited to give a layer ~ 50 nm thick. Ag electrodes were deposited on top of the polymer layer, in a thermal evaporator. The devices were then annealed on a hot-plate at 135 ˚C for a few hours. Devices were tested for photovoltaic performance using a SpectraPhysics 81150 solar simulator operated at AM 1.5 conditions.

Titanium (IV) ethoxide (95% pure) was obtained from Gelest Inc. and was used at obtained without any further purification. Anhydrous ethanol (Aper Alcohol), conc. HCl (Fisher Scientific) and P123 (Sigma) were all used as obtained. Regio-regular poly-3-hexylthiophene (P3HT) was purchased from Aldrich and purified by Soxhlet extraction prior to use.

7.3. Results and Discussion

Synthesizing ordered defect free mesoporous titania films with nanocrystalline walls on unmodified glass substrates is a significant challenge. High reactivity of the titania precursors require special handling and the synthesis and curing conditions must be controlled much more carefully than those used for surfactant templated mesoporous silica. Using highly humid conditions for aging the as deposited films, we have successfully synthesized well ordered titania films. Fig. 7.1 shows the XRD patterns of a mesoporous titania film coated on an unmodified glass substrate synthesized by following the method described above. We can see well ordered (100) reflection coming from the HCP cylinders oriented parallel to the substrate surface. This film was aged for two hours in a sealed container with an open vessel of water in side it to

maintain high level of humidity. Samples which were aged at lower relative humidity show poorly ordered or disordered structures (results not shown). This observation is consistent with reports of several other researchers working in this area.[231, 274]

The other important parameter that must be controlled to obtain the desired titania films is the calcination temperature. In Fig. 7.1 the sample was calcined at 400 °C by the increasing the temperature at 25 °C/min after two 2 hr aging in a highly humid environment. The film was kept at 400 °C for only 10 min before being allowed to cool. We found that 2 hr aging was optimum to obtain well ordered films. Calcination of the films at higher temperatures or for longer times at 400 °C resulted in a loss of the mesoporous order. This is probably because of excessive growth of the anatase crystallites resulting in loss of mesoporosity as explained in the introduction.

We did not observe any wide angle XRD peaks for the films corresponding to large anatase crystallites. This makes sense because with a calcination temperature of only 400 °C, the crystallites remain small enough to avoid mesopore deformation, meaning that they should be only a few nanometers in diameter. Broadening of the diffraction from crystallites this small is so large that they cannot be observed by XRD. To confirm the existence of nanocrystallite we performed Electron Diffraction (ED). Fig. 7.2 shows a TEM image of a titania film on unmodified glass slides along with the corresponding electron diffraction pattern. We can clearly see diffraction rings from the anatase crystalline phase. This confirms that even though we do not observe any wide angle peaks in XRD the titania is nanocrystalline.

After confirming the presence of mesoporosity as well as nano-crystallinity in the titania films coated on unmodified slides, we coated these films on random copolymer modified surfaces following the previously published substrate modification procedure.[50] Fig. 7.3 shows the XRD patterns of titania film on modified surfaces. It shows XRD patterns collected from two sides of the modified glass side. One side is exposed to air, while and the other side is exposed to a glass slide modified with crosslinked PEO-r-PPO copolymer. We can clearly see that side exposed to air has well ordered (100) reflection. The side exposed to a similarly modified slide has a small hump around the same 2θ. As discussed in our previous study, this reduction in the (100) reflection intensity is because of the existence of orthogonally aligned cylindrical channels.[50, 232] When the HCP phase is oriented at an angle close to orthogonal to the substrate, we do not expect to observe any reflections in conventional Bragg-Brentano geometry.[232]

Loss of mesoporous order will also result in loss of XRD reflections. To confirm the presence of order and also to show that the loss of XRD intensity is not due to a loss of order, we observed the samples under SEM. Fig. 7.4 shows SEM image of titania film deposited on modified glass slides that has been confined between two modified surfaces. We can clearly see that the top

surface shows 2D hexagonal periodicity of the pores. Also the cross sectional view shows vertically aligned cylindrical channels, which confirms the presence of orthogonally aligned cylindrical mesochannels through the entire thickness of the film. As discussed in Chapter 6, the pores are not all perfectly orthogonal to the film, but are distributed about an angle of 90° with respect to the substrate. Perfect orientation is not required for organic-inorganic photovoltaic composites; only accessibility to the 2D HCP pore array by the P3HT polymer.

These results suggest the existence of well ordered hexagonal phase on chemically modified surfaces. We achieved this modification by coating the slides with a random copolymer. During calcination the copolymer is also removed thus we achieve the oriented cylindrical mesophase on glass substrates which can be further used for several applications. In this work we also fabricated a bulk heterojunction solar cell using these titania films.

Fig. 7.5 shows a schematic of the bulk heterojunction solar cell fabricated using the titania films (reprinted with permission from Coakley, K.; M.McGehee, M. D. *Appl. Phys. Lett.* **2003**, *83*, 3380.[264] Copyright 2003 American Institute of Physics). Fig. 7.6 shows the I-V curve of the device under AM 1.5 conditions. For comparison, the I-V curve of the bilayer heterojunction solar cell is also included. The performance of the solar cell with aligned cylindrical channels does not show significant improvement over the bilayer solar cell. The high surface area in the mesoporous film should improve the performance of this cell over the bilayer solar cell because of the increased number of excitons that can be separated and transferred to the corresponding electrodes.[280] The power efficiency of the solar cell is calculated as 0.101%. Coakely et. al have reported an efficiency of around 0.45% for an optimized solar cell fabricated using cubic mesoporous titania.[264]

Also the optical density of the films after polymer infiltration is low (~ 0.15, data not shown). Low optical density and the power conversion efficiencies similar to bilayer solar cell suggest that the P3HT polymer was not actually infiltrated into the pores of the titania film by the procedure employed. Presently we can explain these phenomena in two different ways. Firstly the surfactant might not have been removed completely by the brief calcination step, and thus partially decomposed surfactant blocks the pores so that P3HT cannot infiltrate the pores. The other possible reason is that the pore size is so that polymer is not able to filter into the pores of the titania film. Further experiments have to be done to isolate the reason for under-performance of these cells. These initial experiments do suggest the potential to fabricate solar cells using these films, although the performance of the cells has to be improved.

7.4.   Conclusions

In this work we have successfully synthesized mesoporous nanocrystalline titania films on unmodified glass surfaces. We have successfully transferred the idea of chemically neutral surfaces aligning anisotropic mesophases orthogonal to these titania films.[50] Using several characterization techniques we have confirmed the presence of orthogonal channels in the titania films. We have also fabricated a bulk heterojunction solar cell using these titania films with aligned meso channels by infiltrating region-regular P3HT semiconducting polymer into the pores. Initial results of show that the performance of these solar cells has no improvement over bilayer heterojunction solar cells in which there are two layers of titania and P3HT one above other. This suggests that the polymer is not infiltrated into the pores of the titania films. We attribute this either to the presence of small pores or to the incomplete removal of the surfactant template. Further experiments have to be done to improve the performance of the P3HT/o-HCP titania heterojunction solar cells.
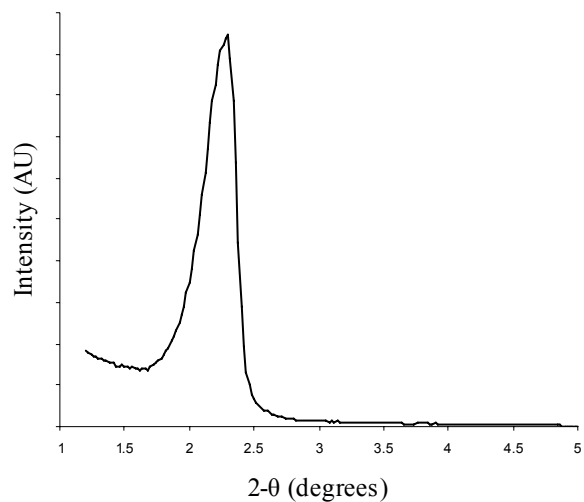
Figure 7.1. XRD pattern of calcined titania film on unmodified glass slide.

(a)

(b)
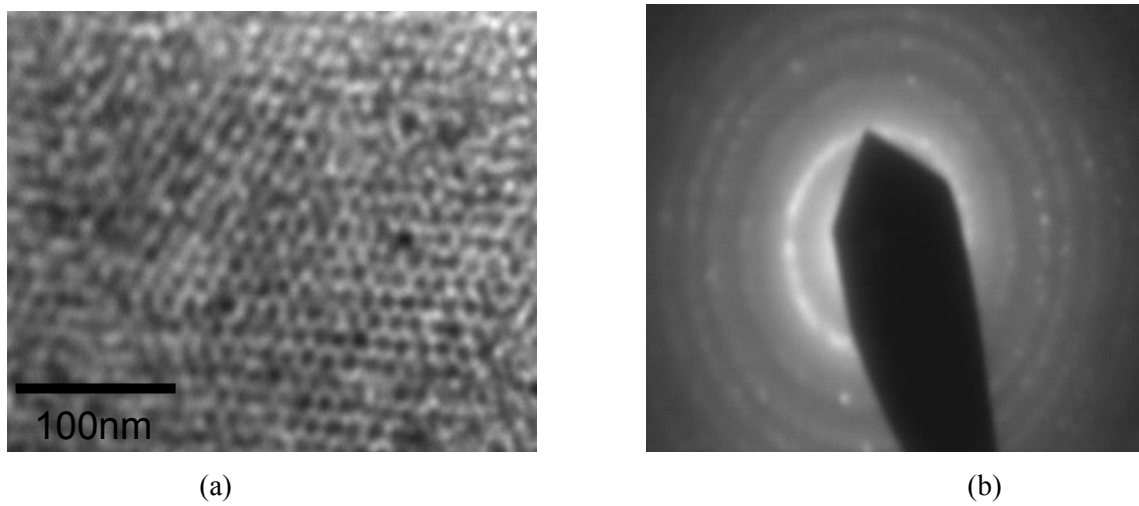
Figure 7.2. TEM image (a) of a titania film on unmodified glass slide and the corresponding electron diffraction pattern (b).
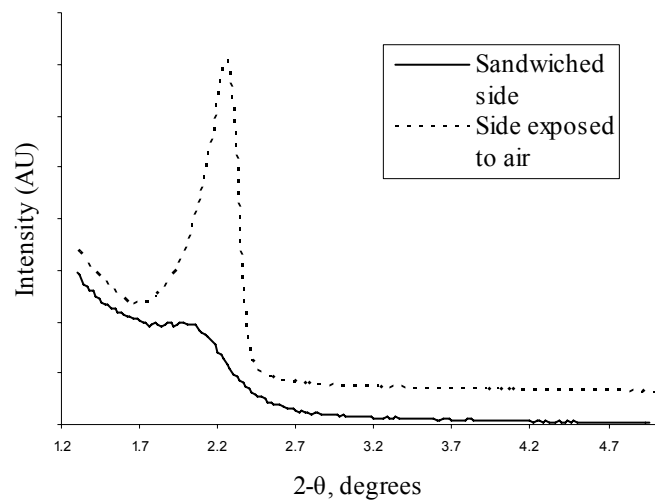
Figure 7.3. XRD pattern of titania film on modified glass surface.
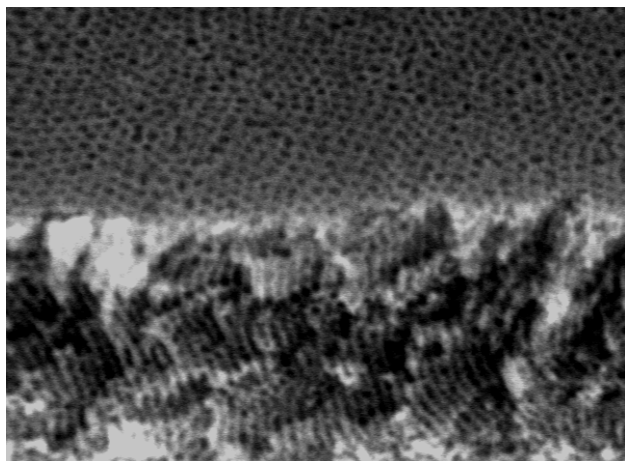
Figure 7.4. Cross sectional SEM image of a 240 nm thick titania film on modified glass slide. Film was confined between two modified surfaces and fractured for SEM imaging.
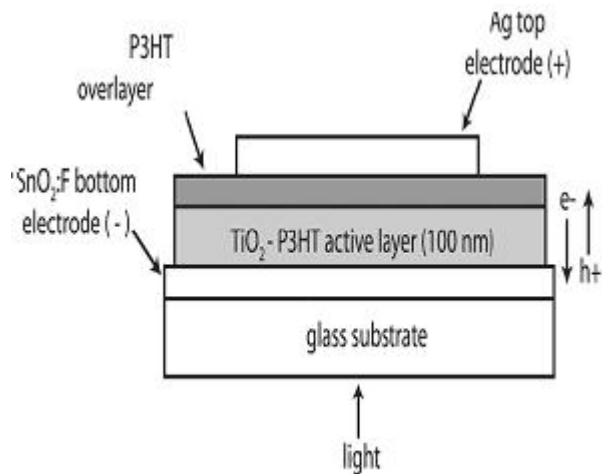
Figure 7.5. Schematic of the solar cell fabricated using the titiania films. This figure is adapted from Coakeley et. al.[264]
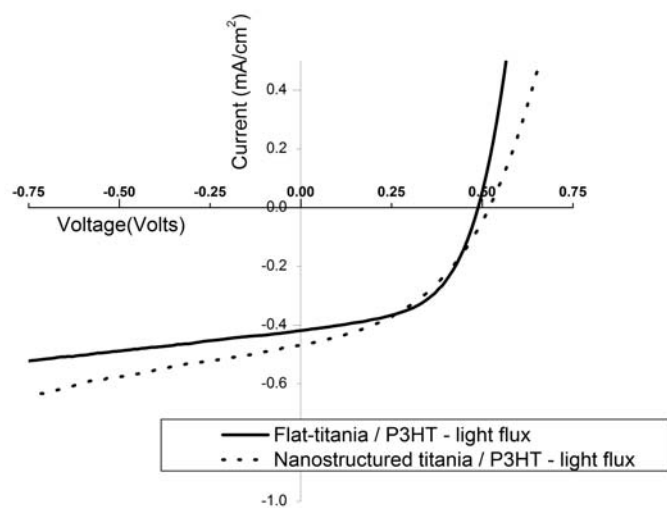
Figure 7.6. I-V curve of the solar cells fabricated by spin coating P3HT onto flat titania or nanostructured porous titania films.

Copyright © Venkat Rao Koganti 2006

109

Chapter 8 Conclusions

This dissertation mainly describes one aspect of surfactant templated sol-gel thin films in extensive detail: achieving orthogonal orientation of the 2D Hexagonally Close Packed (HCP) mesophase. We have explained the alignment of cylindrical channels in terms of two factors: engineering the interactions between mesoscale surfactant molecules and surfaces, and controlling the condensation reaction to ensure flexibility of nanoscale metal oxide building blocks. Orthogonally aligned 2D HCP cylindrical mesophases has been achieved in silica and titania films and the films have been extensively characterized to demonstrate this success. Two applications to these oriented nano structures have been developed, one in the area of silica membranes and second one in the area of titania-based photovoltaics.

In Chapter 4 we first presented our results demonstrating orthogonal alignment of cylindrical channels in 240 nm thick P123-templated silica films. To accomplish, we successfully implemented the idea from molecular simulations (Chapter 3) that confinement of a nonionic surfactant mesophases between chemically neutral surfaces will align the cylindrical pore channels in the direction orthogonal to the substrate. A combination of XRD and TEM characterization confirmed the preservation of the HCP structure and its orientation out of the plane of the substrate. Both random PEO-PPO and the surfactant itself (P123) have been crosslinked to create chemically neutral surfaces. Contact of one surface of the film with either air or unmodified glass caused a loss of orthogonal alignment in 240-nm-thick films prepared using the unmodified dip coating procedure originally described by Brinker's group. Since the films were all originally cast with one side exposed to air, this suggests that the as-deposited films are able to reorient while aging in contact with a pair of chemically modified surfaces. This contradicts some of the thinking in this field, which has focused on ordering during and shortly after coating, and has assumed that minimal changes occur after a film is ordered and completely dried. Our ability to reorient the mesophase in films is a direct consequence of the IR results presented in Chapter 2, which suggest the presence of an induction time period during which silica network is still reacting (and still flexible) and therefore can be manipulated using external forces. This realization is important not only because it enables the orientation effect to be observed in Chapter 4, but also because it can be utilized for post-deposition alteration of sol-gel films, for instance using electrical/magnetic fields, changing the vapor composition, or bringing a film into contact with another slide for imprinting with textural or chemical features.

After synthesizing silica films with aligned cylindrical channels we tried to answer one basic question: "How can silica matrix being inorganic be flexible enough to be reoriented along with the surfactant molecules after depositing the film?" To answer this question we performed

Fourier Transformed Infrared Spectroscopy (FTIR) experiments in Chapter 2 to understand the kinetics of the thin film formation in silica films. We have synthesized mesoporous silica films using CTAB, P123 and Brij-56 surfactants as templates to explore the limitations that this approach may have for different classes of templates. After depositing the silica sol on Si wafers transmission IR spectra of the silica films were collected at regular intervals of time. Monitoring the bands from the silanols and the siloxane bonds we concluded that the condensation of the silanols in the film depends on the kind of surfactant used and also the relative humidity of the cuiring environment.

For the first time in this area of research we found evidence for the presence of an induction time (T_i) after the film deposition during which the condensation rate of the silica network is at its minimum and the silica network is presumably flexible. T_i depends on the kind of surfactant used. Monitoring the silanol band intensity, we concluded that if the surfactant is a nonionic triblock copolymer such as P123, T_i is the maximum compared to the cases when Brij-56 and CTAB were used. We attributed this to surfactant structure and its implications for the interfacial interactions with the ceramic network. Also, a humid environment was found to delay the condensation further than a dry environment. All of the changes in the silanol band intensity are complemented by corresponding changes in the siloxane band intensity. This is an important observation suggesting that the silica network in surfactant templated mesoporous films is flexible for some time in the order of minutes, and can still be manipulated to do post coating modifications. Until today researchers in this area reported changes in the mesostructure in the order of seconds to couple of minutes depositing the film. Our results suggest the existence of additional time frame in the order of several minutes for post synthesis modifications. The flexibility of the silica matrix proven by the IR experiments makes it possible for us to achieve the orthogonal orientation of the channels in chapter 4.

In chapter 3 we discuss the MC simulations we performed to understand the effect of different kinds of surfaces and confinements on the orientation of the HCP mesophase in addition to confirming that neutral surfaces orient HCP cylinders orthogonal to the substrate surface. Using conditions similar to Larson, we have obtained 2D HCP mesophase in simulation boxes without walls. We have successfully simulated the 2D HCP mesophase in confined environment in slit shaped, cylindrical and spherical cavities. In all these confinements we have used hydrophilic, hydrophobic and neutral walls.

In the presence of hydrophilic or hydrophobic slit shaped walls the HCP mesophase orients itself with (100) plane oriented parallel to the walls and with a discrete number of cylinder layers between the walls. Jumps in layers occur when the distance between the walls is approximately an integral multiple of the d-spacing, 'd_{100}'. Influence of the box size in a direction orthogonal to

the direction of the walls has also been understood. Equilibrium energy of the system in the presence of hydrophilic walls is lower than the bulk energy and it approaches the bulk energy value as the box size increases. Neutral slit shaped walls orient the cylinders in a direction orthogonal to the walls consistent with results obtained by other researchers.

Hydrophilic cylindrical and spherical cavities result in several interesting confinement effects of the HCP mesophase. Hydrophilic cylindrical cavities resulted in a range of structures that include uniform monolayers, perforated cylinders to helices as the diameter of the cavity increased. Bigger cavities resulted in perfect helices, although coincidence of the box length with an integer number of unit cells was required. Spherical confinement of the HCP mesophase results in structures similar to the cylindrical confinement that included uniform layers to perforations to ordered perforations to cylindrical channels arranged in layers as the radius of the spherical cavity increased. Neutral walls in cylindrical and spherical cavities resulted in normal alignment of the cylindrical mesophase at the interface similar to the slit shaped cavities. This type of pore alignment has been observed in particles precipitated from aqueous ethanol, and this is the first simulation showing a qualitative explanation for how radially oriented micelles can form in a liquid crystal dispersion.

We have successfully explained the orientation phenomena of the HCP mesophase on chemically modified surfaces in terms of two parameters that need to be controlled: interfacial interactions between the surfactant molecules and the substrate surface and flexibility of the microstructural silica network for some time after deposition. After orienting the cylindrical channels in 240 nm thick silica films, we studied the thickness effects on the orientation of the films. In Chapter 4 we concluded that to align the cylindrical channels in 240 nm thick films, confining the films between two modified surfaces is essential. In chapter 5 we demonstrated that if the thickness of the silica films is around 100 nm or less we do not have to sandwich the films between two modified surfaces. Using X-Ray Diffraction (XRD) and Grazing Incidence X-Ray Scattering (GISAXS) techniques we have conclusively demonstrated that silica films that are 70 nm thick and less will have orthogonally oriented cylindrical channels when present on chemically neutral surfaces. By delaminating a 70 nm thick silica films from the surface of a modified glass slide we obtained a plan view TEM image showing very well ordered oriented cylindrical pores. To complement these results we also showed plan view and cross sectional SEM images of titania films with orthogonally oriented channels. These data are the first reported pieces of evidence for orthogonally oriented HCP channels in ceramic thin films, which open up significant prospects for several interesting applications because of the potential to be coated on any kind of surface.

Being the first group ever to report oriented HCP mesophase on non-porous substrates in surfactant templated silica films, in Chapter 6 we have the demonstrated that it is possible to extend the synthesis of mesoporous thin silica films with orthogonally aligned 2-D hexagonal close packed (o-HCP) mesopores from non-porous glass/silica substrates to porous (anodized alumina) substrates. The alignment is promoted by using a chemically modified surface which is equally attractive to the polar and nonpolar regions of the silica-surfactant mesophase that forms shortly after dip coating. However, the film thickness has a large impact on the success of the process. Thicker films (thickness ~ 240nm) have to be confined between two modified surfaces, whereas thinner films (thickness < 100nm) need not be confined to obtain complete alignment of the cylindrical mesochannels. XRD patterns suggest that we have completely aligned HCP phase in both thin as well as thicker films coated on modified surfaces.

When deposited on porous supports, the mesoprous films can be used as membranes. Accessible, uniform films that are 240 nm and 70 nm thick have been deposited on top of porous alumina supports. This idea can be successfully extended to any porous or nonporous substrate (including arbitrarily curved substrates). This idea of neutral surface aligning the 2D HCP cylindrical mesophase results in mesoporous films on the top of porous substrates rather having cylindrical pores inside the pores of porous substrates, and therefore overcomes the difficulty sometimes found with mesoporous silica of forming helical or ring-shaped mesostructures when confined inside of anodized alumina pores (similar to the structures observed in the simulations of the HCP phase in hydrophilic cylindrical cavities in Chapter 3). High permeability of ethanol in the orthogonally aligned silica membranes confirmed the accessibility of the pores. The uniformity of the silica membranes was demonstrated by size-selective filtering of gold colloids. UV/vis data showed that 20 nm particles are filtered out while particles close to 5 nm in diameter passed thorough the orthogonally aligned silica membranes. Thicker sandwiched films are completely defect free. In the case of thinner non-sandwiched films, there appears to be an optimum thickness giving both orthogonally aligned pores and films without nanometer-scale defects. Films that are thinner than the optimum thickness develop defects during calcinations which are evident from the 20 nm gold filtration data. The pore size of silica membranes can, in principle, be easily tuned from 5 nm to more than 50 nm as required by using solvents and temperature to swell the micelle templates. In the future, these films should be useful for size based separations of macromolecules including inorganic colloids and proteins. In addition, the o-HCP channels should find numerous applications in the areas of sensors and catalysis.

After synthesizing mesoporous silica membranes with accessible cylindrical pores, in Chapter 7 we describe the synthesis of mesoporous nano crystalline titania films on unmodified glass surfaces. We have successfully transferred the concept from Chapter 4 that chemically neutral

surfaces induce orthogonal HCP mesophase alignment to mesoporous titania films with the target application being photovoltaic cells. Some of the most knowledgable experts in the field of inorganic-organic hybrid solar cells, including Michael McGehee at Stanford University, have suggested that o-HCP titania is the ideal film structure. This is because of the well-known ability of cylindrical mesopores to control electronic transfer and transport properties of conjugated polymers such as poly(3-hexylthiophene) (P3HT). Using several characterization techniques we have confirmed the presence of orthogonal channels in the titania films. We have also fabricated a bulk heterojunction solar cell using these titania films with aligned meso channels by infiltrating regio-regular P3HT semiconducting polymer into the pores. Initial results show that the performance of these solar cells has not yet achieved improvement over bilayer heterojunction solar cells consisting of a layer of P3HT on a nonporout titania film. This suggests that the polymer is not infiltrated into the pores of the titania films, and if it is that it is not aligned. We attribute this either to the presence of small pores or to the incomplete removal of the surfactant template. Further experiments have to be done to improve the performance of the solar cells. The crystallization of titania during calcination must be undertood and controlled to allow complete removal of surfactants without loss of order due to excessive anatase crystal growth. The effects of process parameters such as surfactant and precursor concentration must also be better understood to allow the pore size and wall thickness to be independently controlled. This will allow us to control the infiltration of P3HT and stability of the photovoltaic cells better.

Despite a need for imporovement of photovoltaic performance in the first cells that were attempted, the major aim outlined in the introduction to orient the cylindrical channels orthogonal to the substrate surface in sol-gel ceramic films has been achieved. Versatility of the approach has been demonstrated by using silica, silicon, and porous anodized alumina substrates. Silica membranes synthesized on porous alumina showed excellent permeability as well as a high degree of uniformity indicated by size based exclusion of gold particles. The versatility of the type of film has been demonstrated by extending the synthesis from silica to titania. Titanium alkoxides are typical high-reactivity precursors, and our ability to successfully make o-HCP films with titania suggests that other researchers will be able to apply this technique to other semiconducting oxides. Although the power conversion efficiency of the solar cell fabricated using these films does not yet show improvement over existing cells, the process is flexible enough to allow steps to be taken to improve efficiency. These experiments were the first steps taken to fabricate thin film solar cells using these o-HCP films, and a favorable comparison of these cells to existing solar cells can be seen as a good start.

This novel pore structure can find numerous applications in several different areas. Catalysis, sensors, low-K dielectric materials, photocatalysis, etc. are some areas to mention a few. Intersting applications should result in fuel cells where we can use these materials as proton exchange membranes using zirconia, ceria, and other transition metal oxide precursors.

Appendix A Orthogonal Orientation of Cylindrical Meso Channels with Smaller Pore Sizes

A. 1   Introduction

Synthesis of mesoporous silica films with oriented cylindrical channels using P123 as surfactant template is discussed in Chapter 4. P123 is a polymeric surfactant, and because of its large size the resulting materials have pore sizes 5 nm and above. For some applications like membrane separations, smaller pore sizes are desirable. In this chapter we describe our work to synthesize silica films with orthogonally aligned HCP channels with pore sizes that are less than 5 nm. We use a commercially available nonionic surfactant with decaethelyneglycol hexadecylether as its primary component (Brij-56) as the surfactant template. Similar to P123, Brij-56 has polyethelyneglycol (PEO) head group, but the number of PEO units in Brij-56 is less in P123. Brij-56 also has a much smaller tail compared to P123.

In Chapter 4, we used a random copolymer modified surface to act as a chemically neutral surface for P123 template. For Brij-56 we cannot use the same surface because the basic building blocks of Brij-56 are different from P123. P123 has a PPO chain as hydrophobic unit, whereas Brij-56 has an alkyl chain as hydrophobic unit. Attemps to align Brij-56 templated films using surfaces modified with crosslinked PPO-r-PEO or P123 were not successful. We suspect that this is because the length scale of the PEO and PPO blocks is significantly greater than the length of the head and tail of Brij-56, which does actually not make the surface act chemically "neutral". To achieve a neutral surface for Brij-56, we will modify the glass surface by partial silylation, which replaces the terminal –OH groups with –CH$_3$. Scheme.1 shows the reaction happening at the surface of a glass slide when it reacts with a silane. Silylation will only be carried out partially so that the surface is not completely hydrophobic. The degree of silylation will be quantified by measuring the contact angle between water and the modified glass slides. Using non-ionic surfactants we hope to achieve equal interaction of glass surface with both head and tail of the surfactant molecules. An ionic surfactant (which has either a positive or negative charge in addition to having polar head and non polar tail) on the other hand poses an additional, longer-ranged interaction between the counter ion and the surface thus making it difficult to achieve equal interaction.

$$\text{OH} \quad \text{OH} \qquad + \qquad (\text{CH}_3)_3\text{SiCl} \qquad \longrightarrow \qquad \begin{array}{c} \text{Si(CH}_3)_3 \\ | \\ \text{O} \quad \text{OH} \end{array} \quad + \quad \text{HCl}$$

Scheme.1: Reaction between trimethylchlorosilane and hydrophilic glass surface resulting in a modified surface

To confirm the orientation of the HCP cylinders we use both XRD and TEM as characterization techniques. As explained in Chapter 4 and demonstrated conclusively in Chapter 5 with additional techniques, when the cylindrical pores are oriented orthogonal to the substrate we do not see any peaks in the XRD patterns in conventional Bragg-Brentano geometry. Absence of peaks in XRD patterns and well ordered pores in TEM images confirmed the presence of orthogonally oriented cylindrical channels.

A. 2   Experimental Section

Before preparing the films, some of the glass slides were modified using TMCS. Before modifying, the glass slides were cleaned using a piranha solution made up of a 7:3 (by volume) mixture of concd H_2SO_4 and 30 wt% H_2O_2 solution. Hexane was used as solvent to avoid the presence of an excessive amount of dissolved water. The clean slides were immersed in hexane and then TMCS was added in an atmosphere of nitrogen so that its reaction with atmospheric moisture is reduced. Varying degrees of modifications were achieved by using different amounts of TMCS. The degree of modification was quantified by measuring the contact angle between the glass slides and water. A drop of water was placed on the glass slide and its image was projected on to a sheet of paper. The angle is then measured manually.

Following the procedure described in Chapter 4 for preparing P123 templated films, we prepared the sol for dip coating Brij-56 surfactant templated thin films. As mentioned above, the main component of Brij-56 is decaethyleneglycol hexadecyl ether. The coating sol was prepared by addition of a solution of Brij-56 to a prehydrolyzed silica sol. First, tetraethoxysilane (TEOS), ethanol, water and HCl (mole ratio 1 : 3.8 : 1:5*10^{-5}) were refluxed at 70 ℃ for 90 minutes. Then, additional water and HCl were added, increasing the concentration of HCl to 7.34mM. Also at this time required amount of water to reach the final mole ratio was added. After stirring this mixture at 25 ℃ for 15 min, the sols were aged at 50 ℃ for 15 min. Brij-56 in the required amount was dissolved in ethanol and this solution was added to the above aged silica sol with constant stirring. The final mole ratios were 1 TEOS : 22 C_2H_5OH : 5 H_20 : 0.004 HCl : x brij-56. In order to fix the value 'x' we performed several experiments with different value for 'x'. Slides were dip coated with the above prepared sol at a withdrawal speed of 7.6 cm/min. A value of x=0.055 was fixed, which results in 2D HCP cylindrical mesophase on unmodified surfaces. This hexagonal orientation was confirmed using XRD.

After coating, the films were aged and dried at room temperature for 24 hrs, then at 70 ℃ for 24 hrs, and finally at around 120 ℃ for 24 hrs. After these steps the silica would have condensed into a reasonably stiff network. The films were then calcined in air at 500 ℃ for 4 hr.

Brij-56 and TEOS (99% pure) were obtained from Fluka. De-ionized ultra filtered water (Fisher), anhydrous ethanol (Fisher) and hexane were used as solvents. Trimethylchlorosilane was obtained from Sigma-Aldrich (99+% pure) and was handled under nitrogen with transfer by gas-tight syringe to avoid introduction of atmospheric moisture prior to silylation.

XRD patterns were collected with a Siemens (D-5000) Diffractometer. Keeping the glass slides in the sample holders and placing the holder in the slot provided in the diffractometer was sufficient to obtain the diffraction patterns. TEM was used to directly observe the pore structure of these materials. Mesoporous material was scraped off of the slides and was deposited onto lacey carbon grids to view under the TEM. These images were recorded on a JEOL 2000FX microscope operated at 200 kV. We have tried microtoming in order to delaminate the film from the slide with the intention of viewing the material from a known direction. Microtoming involves inverting a capsule of epoxy resin on to the glass slide and allowing the resin to solidify. This cured resin was then pulled off the capsule. Using a diamond cutting tool, a thin piece from the surface of the capsule was sliced off with the intention of getting a plan view of the material delaminated from the substrate. Microtomed powders (scraped from substrate surface) were also used to help confirm the pore structures.

A. 3   Results and Discussion

Using the procedure described above we have successfully synthesized thin, transparent, defect free SiO_2 films on plain glass substrates using Brij-56 as surfactant template. We have also coated partially TMCS-modified glass slides with the silica precursor sol. The slides are modified to different degrees using different amounts of TMCS. The degree of modification was quantified by measuring the contact angle between water and the modified surface. Fig. A.1 shows the XRD patterns of Brij-56 templated silica films on glass slides as a function of different degrees of modification. Contact angles are also indicated on the plots. Glass slide with contact angle of 25° is the unmodified slide. We can clearly see a well ordered (100) reflection in many of the curves which is attributed to presence of cylindrical channels oriented parallel to the substrate. The d-spacing is around 3.5 nm

As the contact angle increases the intensity of the (100) peak decreases. At contact angles around 65° the XRD intensity of the (100) peak is the least. At higher angles we again see an increase in the XRD intensity. As discussed in Chapter 4, this suggests that we see orthogonally oriented cylindrical channels at intermediate levels of TMCS modification. In this study we

found least intensity of the (100) peak around contact angles of 65°. This is also consistent with the simulation results discussed in Chapter 3 that suggest that HCP phase orients itself orthogonal to the substrates only on neutral surfaces. On hydrophilic and hydrophobic surfaces we observe HCP cylinders oriented parallel to the substrate. When the surface is modified to contact angles higher than 65° the surface is hydrophobic resulting in parallel orientation of cylindrical channels.

In order to confirm that the loss of intensity in XRD patterns is due to orthogonal orientation of the HCP channels and is not due to a loss in mesoporous order, we observed these materials under TEM. Fig. A.2 shows the TEM image of silica films coated on unmodified glass slide. The film was scraped off the glass slide and then microtomed. As expected wee see a well ordered cylindrical array of pore channels. Well ordered (100) peak in fig. A.1 for slide with contact angle 25° and the TEM image in fig. A.2 suggest that we have highly ordered mesoporous materials on unmodified slides. Fig. A.3a shows the XRD pattern of a silica films coated on a glass slide that has a contact angle with water of 64°. We can clearly see the absence of XRD peaks. The materials was then scraped off and suspended on a TEM grid and then observed under TEM. Fig. A.3b shows a representative TEM image of this material. We can see a well ordered array of cylindrical channels consistent with the HCP phase. This confirms that the loss of intensity in the XRD patterns in fig. A.3a is because of the orthogonal orientation of HCP channels.

Scraping off the material from the glass slide destroys the orientation information. One way of preserving the orientation is to replicate the film surface onto a cellulose acetate tape. Using the standard procedures, we replicated the surface meso structure of a silica film coated on an unmodified slide. We observed the cellulose acetate tape under TEM. Fig. A.4 shows the TEM image of the cellulose tape which has the film meso structure replicated onto it. We can clearly see the parallel aligned cylindrical channels. This procedure was not successful when trying to replicate the surface of a film with aligned cylindrical channels.

In another attempt to preserve the orientation we have tried to pull off the film as it is by using an epoxy resin. A capsule of epoxy resin was inverted on the film and was then cured. After curing the resin was pulled off and microtomed to preserve the orientation. Fig. A.5 shows a TEM image of the film that was pulled off and then microtomed. The film was coated on a slide that was modified with TMCS to obtain a water contact angle of 60°. We can clearly see the orthogonally oriented cylindrical channels arranged in hexagonally close packed crystal structure.

All these observations confirm the presence of orthogonally aligned cylindrical channels with pore sizes around 3.5 nm when the substrate surface is appropriately modified. The main issue in

this regard has been obtaining the modified surface consistently. In this work substrate surface was reacted with TMCS in hexane. The amount of TMCS required to obtain a modified surface with water contact angle of ~ 65° was not consistent. TMCS is very reactive with moisture and controlling the rate of reaction is very important to obtain consistent modifications. This has been a major challenge and is yet to be addressed properly. Although proper care was taken while transferring TMCS from the bottle into hexane by having a continuous flow of N_2 to minimize reaction of TMCS with atmospheric humidity, we could not achieve consistent modification. Presently, we believe that the concentration of hydroxyl groups on the surface of the cleaned slides will have to be measured and controlled precisely to be able to achieve reproducible modification of the surface. Further studies will be needed for this purpose, or to find other substrates (such as polymer coupons) that will act chemically neutral towards Brij-56 templated films.

Another challenge that we have encountered is that contact angle might not be an adequate measure of surface modification. It gives the effect of surface modification on a size scale of millimeters. An ideal parameter would give the effect of surface modification on a size scale in the order of nanometers. In spite of these difficulties in obtaining reproducible modifications, we are able to obtain orthogonally aligned HCP cylinders when the surface is modified to the right extent. Both XRD and TEM evidence support the existence of orthogonally oriented HCP cylindrical channels when the surface is properly modified.

A. 4   Conclusions

In this chapter we have successfully demonstrated that using chemical modification techniques we can achieve a chemically neutral surface which can align the 2D HCP mesophase of a short-chain surfactant orthogonal to the substrate. By partially replacing the terminal –OH groups on plain glass substrates with –CH_3 we achieved a uniform distribution of –OH and –CH_3 groups on a glass substrate. This was achieved when the substrate surface reacts with TMCS in hexane. The degree of modification was quantified by measuring the contact angle between water and modified surface. This neutral substrate was used to coat silica films using Brij-56 as surfactant template. XRD and TEM evidences show that on appropriately modified surfaces (water contact angle ~ 65°) we do not see any XRD peaks, but the TEM images show well ordered HCP mesophase. We have also used microtoming and replication sample preparation techniques to prepare TEM samples. Using these sample preparation techniques we have successfully prepared TEM samples without losing the orientation information. These TEM images how parallel and perpendicular cylindrical channels on unmodified and modified surfaces respectively. Although there are some difficulties in obtaining consistent modifications we can presently say that the

chemically neutral surfaces obtained by the procedure described above align the HCP mesophase perpendicular to the substrate surface resulting in cylindrical pores with diameters below 4 nm.
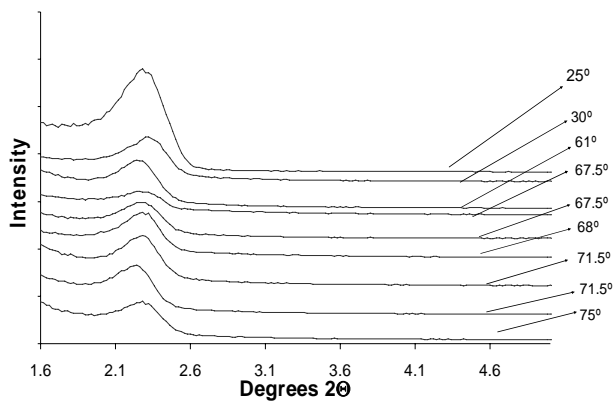
Figure A.1. XRD patterns of silica films on glass slides as a function of degree of modification of the glass slide. Glass slides were modified by TMCS.
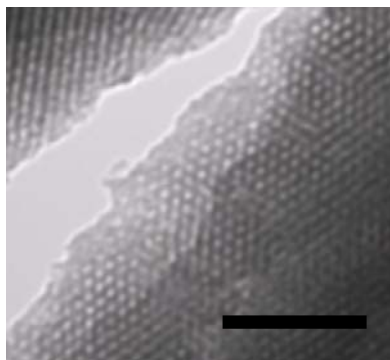
Figure A.2. TEM image of the silica film scraped off from an unmodified glass slide. Scale bar is 100 nm.
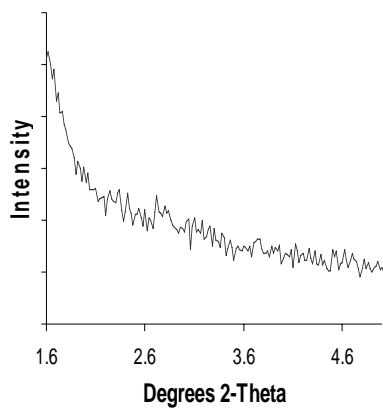
(a)
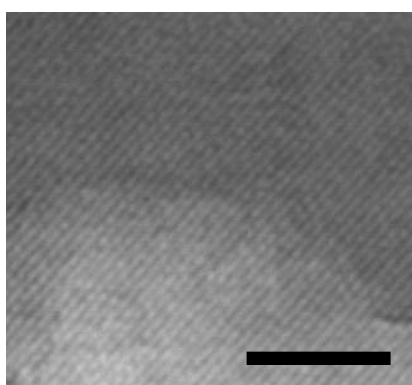
(b)

Figure A.3. XRD pattern of silica films on glass slide with water contact angle 64° prior to coating of the film (a) and TEM image of the film scraped off from the same slide (b). Scale bar is 100 nm.
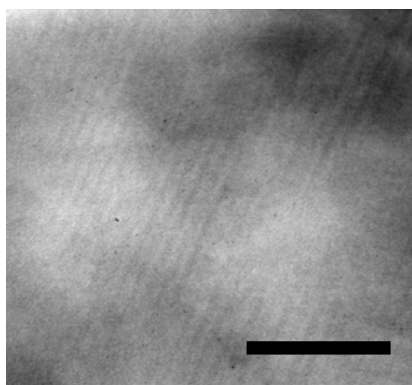
Figure A.4. Plan view image of silica film on unmodified glass slide. The surface is replicated onto a cellulose acetate tape and this is the image of the tape. Scale bar is 100 nm.
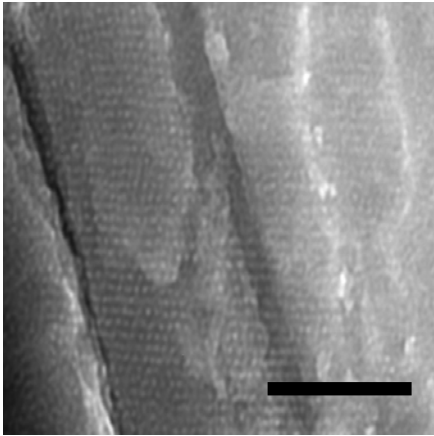
Figure A.5. TEM image of film pulled off from a glass slide with water contact angle of 60°. The film was pulled off using a capsule of epoxy resin and was then microtomed. The scale bar is 100 nm. The ridges in the background of the images result from the microtoming itself.

Appendix B Synthesis of Mesoporous Silica Powders with Organic Functionalities using Nanocasting

B. 1   Introduction

The main focus of this thesis has been to synthesize oriented mesoporous inorganic films using surfactant templation and to explore applications of these films. As explained in the introduction, the mechanism of formation of ordered phases in thin films is quite different from powders. In powders the mesophase forms using a mechanism called cooperative self assembly. This mechanism involves simultaneous precipitation of silica and mesophase formation. This mechanism has been explained at greater detail in literature.[282,283] In the case of films the mesophase formation is completed well before the condensation has begun. As explained in chapter 1 in thin films volatile solvents evaporate within seconds after casting the film. This evaporation induces the self assembly (EISA) of the surfactant species.[284] In other words self assembly is complete with in seconds and the inorganic precursors are still in the hydrolyzed form and are not condensed.

Nanocasting is a strategy for the synthesis of mesoporous inorganic powders using a mechanism that has similarities with the EISA process. In 1995, Göltner and coworkers used concentrated surfactant liquid crystalline phases as templates for the synthesis of mesoporous silica.[281] Surfactant was dissolved in water at high concentrations (~ 50 wt%). At this concentration the surfactant formed a 2D HCP mesophase. To this mixture with a preformed mesophase, TMOS was added slowly. Hydrolysis of TMOS produced methanol which destroyed the HCP mesophase initially established. However, evaporation of the methanol using gentle vacuum reformed the HCP mesophase with hydrolyzed silica species which could condense around the micelles to form a materials with 2D HCP mesophase. Since the mesophase is cast into silica, this procedure is also called nanocasting. Thus this process is similar to the EISA process which has been the major focus of this dissertation. The pore structures achieved using nano casting procedure are more predictable than those formed with the cooperative assembly approach because the technique is based on making an analogy between binary solvent/surfactant liquid crystals and mesoporous materials precursors.[282] The nanocasting technique allows the design of porous materials with controlled pore size and pore morphology.[282]

The main objective of this appendix is to synthesize organic-inorganic hybrid materials using the nanocasting procedure. Adding organic groups to the inorganic frame work will greatly change the physical and chemical properties of the inorganic materials and hence will extend the scope of utilizing these materials for various applications.[285,286] Standard procedure to synthesize functional materials utilizes post-synthesis grafting with organoalkoxysilanes.[287] Although this

procedure has resulted in interesting functional materials, the ideal method to obtain functional materials would be to incorporate the functionality into the frame work while synthesizing the materials. Organically modified silica precursors and bridged silica precursors provide excellent alternatives to obtain functionalized materials without post synthesis grafting. Many studies in the literature have synthesized these hybrid materials using cooperative assembly.[288-290] Because of the above mentioned advantages of nanocasting over cooperative self assembly, we will use the nanocasting procedure to synthesize organic-inorganic hybrid materials. In this work we use bis(trimethoxysilyl)ethane as a precursor, which has the following structure:

$$(CH_3O)_3 - Si - CH_2 - CH_2 - Si - (OCH_3)_3$$
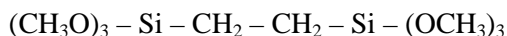
The above compound has hydrolyzable ethoxy groups on either end of the molecule and an ethylene bridge to provide organic character to the pore walls. The hydrolysis and condensation of this precursor is similar to the hydrolysis and condensation of tetraethoxy silane (TEOS) discussed in Chapter 1, and in fact this precursor generally forms gels more easily than tetraalkoxysilanes because of the organic bridging group. The final product contains built-in organic groups in the walls of silica matrix. Here, we will use CTAB as surfactant template, and TMOS and BTMSE as materials precursors.

B. 2   Experimental Section

0.5 g of CTAB was dissolved in 1.1 g of water in a glass vial. The mixture was stirred for about 5 min to dissolve the CTAB. The pH of water was ~ 2 when the precursor was TMOS and was ~ 4 when the precursor was BTMSE to minimize the condensation rate of the precursor. After stirring the surfactant/water mixture, the vial was transferred on to a hot plate at 50 °C. In about a minute the white solution turned transparent and then it formed a gel. This signifies the formation of the mesophase. Based on the concentration of CTAB the mesophase formed is 2D-HCP (this has been confirmed by polarized optical microscopy studies of other members of our research group). To this mixture the precursor (1.2 g of TMOS or 1 g of BTMSE) was added under constant stirring. After the stirring the precursor for about 2-3 min the resulting mixture was immediately transferred to a Petri dish and was spread to form a thin film. The Petri dish was then kept on a hot plate (50 °C) for 1 day. Methanol formed during the hydrolysis of the precursors was allowed to naturally evaporate during the initial stages of heating at 50 °C. A transparent gel was recovered and was then ground into fine powder. This powder was heated at 100 °C for 24 hr. The powder was then exposed to NH_3 vapor for 24 hrs to promote complete condensation of silica. To do this, 0.1 ml of conc. NH_4OH was placed in the vicinity of the silica powder in a sealed environment. Care was taken so that powder does not come into direct contact with NH_4OH. Evaporation of the ammonia solution created the ammonia vapor for materials

treatment. After the NH_3 treatment the samples were washed with ethanol to remove the surfactant.

TMOS (Sigma), BTMSE (Gelest), CTAB (Sigma), de-ionized ultrafiltered water (Fisher), concentrated ammonia (~29%, Merck) and anhydrous ethanol (Aaper Alcohol and Chemical) were all used as received.

B. 3   Results and Discussion

Using the procedure above we synthesized well ordered silica powders with ethane groups built into the frame work of silica. To start, we synthesized pure silica powders using the nano casting procedure. Fig. B.1 shows the powder XRD patterns of the silica powder at different stages of synthesis. Ammonia treatment was essential to rapidly obtain materials with stiff silica network. This figure shows the XRD plots of as synthesized materials and materials after ammonia treatment and after removing the surfactant. We can clearly see the well ordered (100) peak and higher order (110) and (200) reflections characteristic of 2D HCP mesophase materials.

After confirming that the synthesis procedure yielded well ordered HCP materials using non-bridged precursor (TMOS) we used the same procedure to synthesize silica materials with built in organic functionality. We used BTME as silica precursor. The amount of precursor was calculated based on the work by Chmelka et. al.[291]. They presented a generalized approach to calculate the amount of precursor required from the phase diagram of the surfactant. The strategy is based on replacing the volume of water in a desired phase with the equivalent volume of the condensed material.

Fig. B.2 plots the XRD patterns of material synthesized using BTMSE as precursor. XRD patterns of as synthesized material along with ammonia vapor treated materials and materials after removing the surfactant are shown. We can clearly a well ordered (100) peak in the plots. This shows that the materials has a 2D HCP mesophase. Absence of higher order reflections signifies that the materials is not as well ordered as the pure silica materials synthesized using TMOS as precursor. Synthesizing materials using BTMSE as precursor by adding TMOS to the BTMSE also resulted in well ordered materials. Fig. B.2 also shows the XRD pattern of the material synthesized using two precursors TMOS and BTMSE (mole ratio of TMOS : BTMSE = 0.75) of as synthesized materials before removing the surfactant template. Although we do not see improvement in the order of the material by adding TMOS to the BTMSE, these results show potential to synthesize materials with desired loadings of the organic groups.

These results show that we have successfully synthesized pure silica as well hybrid silica materials using nanocasting procedure. We have also used other bridged precursors like bistrimethoxysilylhexane (BTMSH) and bistrimethoxysilylpropylamine (BTMSPA) to synthesize

mesoporous materials. The high reactivity of these precursors to yield condensation products made it difficult to obtain ordered materials using these precursors.

B. 4   Conclusions

   In this short study we have successfully synthesized mesoporous silica and ethylene-bridged organosilica powders using the nanocasting approach. Using TMOS as silica precursor we have synthesized 2D HCP mesoporous materials. XRD patterns proved the existence of the mesophase. We have also shown that the nanocasting method can be extended to bridged precursors. Using BTMSE as precursor we synthesized silica powders with ethane bridge built into the inorganic frame work. Precursors with different bridging groups were highly reactive, thus hindering the self assembly process to result in ordered materials.
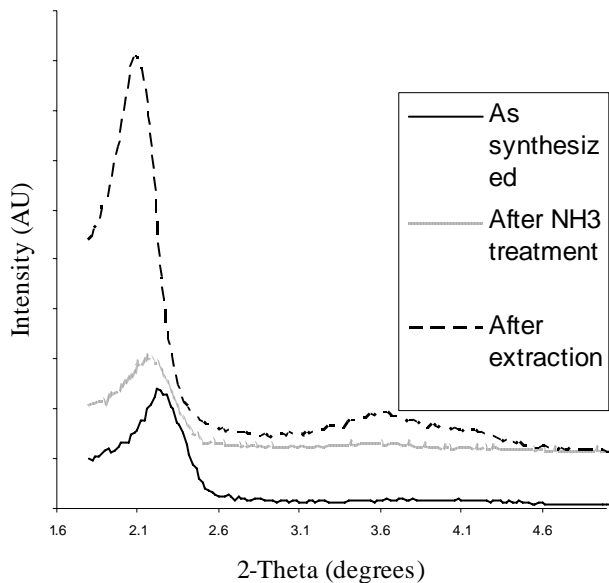
Figure B.1. XRD patterns of silica powders synthesized using TMOS as silica precursor
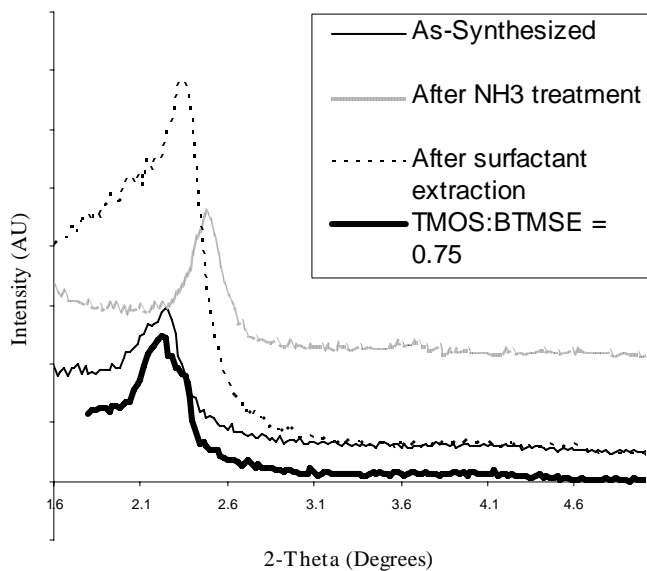

Figure B.2. XRD patterns of silica powders synthesized using BTMSE as silica precursor

References

1. Zhao, X. S. L., G. Q. M.; J. Millar, G. J. *Ind. Eng. Chem. Res.* **1996**, *35*, 2075.
2. Beck, J. S. V., J. C.; Roth, W. J.; Leonowicz, M. E.; Kresge, C. T.; Schmitt, K. T.; Chu, C. T.-W.; Olson, D. H.; Sheppard, E. W.; McCullen, S. B.; Higggins, J. B.; Schlenker, J. L. . *J. Am. Chem. Soc.* **1992**, *114*, 10834.
3. Kresge, C. T. L., M. E.; Roth, W. J.; Vartuli, J. C.; Beck, J. S. . *Nature* **1992**, *359*, 710.
4. Ying, J. Y.;Mehnert, C. P.Wong, M. S. *Angew. Chem. Int. Ed.* **1999**, *38*, 56.
5. Ciesla, U.Schüth, F. *Current Opinion in Colloid & Interface Science* **1999**, *27*, 131.
6. Ogawa, M. *Supramolecular Sci.* **1998**, *5*, 247.
7. Lu, Y. F., H.; Stump, A.; Ward, T. L.; Rieker, T.; Brinker, C. J. *Nature* **1999**, *398* 223.
8. Lu, Y. F. B., C. J.; Sellinger, A.; Fan, H. Y. *Adv. Mater.* **1999**, *11*, 579.
9. Hua, Z.-L.;Shi, J.-L.;Wang, L.Zhang, W.-H. *Journal of Non-Crystalline Solids* **2001**, *292*, 177.
10. Sarah H. Tolbert, S., H.; Schaffer, T. E.; Feng, J.; Hansma, P. K.; Stucky, G. D. . *Chem. Mater.* **1997**, *9*, 1962.
11. Falcaro, P.;Costacurta, S.;Mattei, G.;Amenitsch, H.;Marcelli, A.;Guidi, M. C.;Piccinini, M.;Nucara, A.;Malfatti, L.;Kidchob, T.Innocenzi, P. *J. Am. Chem. Soc.* **2005**, *127*, 3838.
12. Alonso, B.;Balkenende, A. R.;Albouy, P.-A.;Amenitsch, H.;Rager, M.-N.Babonneau, F. *J. Sol-Gel Sci. Technol.* **2003**, *26*, 587.
13. Yang, H. C., N.; Sokolov, I.; Ozin, G. A. *J. Mater. Chem.* **1997**, *7*, 1285.
14. Liu, W. Z., Y.; Wang, C. *Inorg. Mater.* **2006**, *42*, 641.
15. Monnier, A.;Schüth, F.;Huo, Q.;Kumar, D.;Margolese, D.;Maxwell, R. S.;Stucky, G. D.;Krishnamurty, M.;Petroff, P.;Firouzi, A.;Janicke, M.Chmelka, B. F. *Science* **1993**, *261*, 1299.
16. Firouzi, A.;Kumar, D.;Bull, L. M.;Besier, T.;Sieger, P.;Huo, Q.;Walker, S. A.;Zasadzinski, J. A.;Glinka, C.;Nicol, J.;Margolese, D.;Stucky, G. D.Chmelka, B. F. *Science* **1995**, *267*, 1138.
17. Lu, Y. F., H.; Stump, A.; Ward, T. L.; Rieker, T.; Brinker, C. J. *Nature (London, United Kingdom)* **1999**, *398* 223.
18. Huo, Q.;Margolese, D. I.;Ciesla, U.;Feng, P.;Gier, T. E.;Sieger, P.;Leon, R.;Petroff, P. M.;Schueth, F.Stucky, G. D. *Nature* **1994**, *368*, 317.
19. Tanev, P. T.Pinnavaia, T. J. *Science (Washington, D. C.)* **1995**, *267*, 865.
20. Ciesla, U.;Demuth, D.;Leon, R.;Petroff, P.;Stucky, G.;Unger, K.Schueth, F. *J. Chem. Soc., Chem. Commun.* **1994**1387.
21. Huo, Q.;Margolese, D. I.;Ciesla, U.;Demuth, D. G.;Feng, P.;Gier, T. E.;Sieger, P.;Firouzi, A.;Chmelka, B. F.et al. *Chem. Mater.* **1994**, *6*, 1176.
22. Bagshaw, S. A.;Prouzet, E.Pinnavaia, T. J. *Science* **1995**, *269*, 1242.
23. Bagshaw, S. A.Pinnavaia, T. J. *Angew. Chem., Int. Ed. Engl.* **1996**, *35*, 1102.
24. Antonelli, D. M.Ying, J. Y. *Chem. Mater.* **1996**, *8*, 874.
25. Antonelli, D. M.;Nakahira, A.Ying, J. Y. *Inorg. Chem.* **1996**, *35*, 3126.
26. Doshi, D. A.;Gibaud, A.;Liu, N.;Sturmayr, D.;Malanoski, A. P.;Dunphy, D. R.;Chen, H.;Narayanan, S.;MacPhee, A.;Wang, J.;Reed, S. T.;Hurd, A. J.;van Swol, F.Brinker, C. J. *J. Phys. Chem. B* **2003**, *107*, 7683.
27. Gibaud, A.;Grosso, D.;Smarsly, B.;Baptiste, A.;Bardeau, J. F.;Babonneau, F.;Doshi, D. A.;Chen, Z.;Brinker, C. J.Sanchez, C. *J. Phys. Chem. B* **2003**, *107*, 6114.
28. Doshi, D. A.;Gibaud, A.;Goletto, V.;Lu, M.;Gerung, H.;Ocko, B.;Han, S. M.Brinker, C. J. *J. Am. Chem. Soc.* **2003**, *125*, 11646.
29. Grosso, D.;Balkenende, A. R.;Albouy, P. A.;Ayral, A.;Amenitsch, H.Babonneau, F. *Chemistry of Materials* **2001**, *13*, 1848.

30.   Cagnol, F.;Grosso, D.;Soler-Illia, G. J. d. A. A.;Crepaldi, E. L.;Babonneau, F.;Amenitsch, H.Sanchez, C. *J. Mater. Chem.* **2003**, *13*, 61.

31.   Grosso, D.;Babonneau, F.;Albouy, P.-A.;Amenitsch, H.;Balkenende, A. R.;Brunet-Bruneau, A.Rivory, J. *Chem. Mater.* **2002**, *14*, 931.

32.   Tiemann, M.;Goletto, V.;Blum, R.;Babonneau, F.;Amenitsch, H.Linden, M. *Langmuir* **2002**, *18*, 10053.

33.   Alonso, B.;Balkenende, A. R.;Albouy, P.-A.;Durand, D.Babonneau, F. *New J. Chem.* **2002**, *26*, 1270.

34.   Grosso, D.;Babonneau, F.;Soler-Illia, G. J. d. A. A.;Albouy, P.-A.Amenitsch, H. *Chem. Commun.* **2002**748.

35.   Grosso, D.;Babonneau, F.;Sanchez, C.;Soler-Illia, G. J. d. A. A.;Crepaldi, E. L.;Albouy, P. A.;Amenitsch, H.;Balkenende, A. R.Brunet-Bruneau, A. *J. Sol-Gel Sci. Technol.* **2003**, *26*, 561.

36.   Brennan, T.;Roser, S. J.;Mann, S.Edler, K. J. *Langmuir* **2003**, *19*, 2639.

37.   Innocenzi, P.;Falcaro, P.;Grosso, D.Babonneau, F. *J. Phys. Chem. B* **2003**, *107*, 4711.

38.   Innocenzi, P.;Kidchob, T.;Bertolo, J. M.;Piccinini, M.;Cestelli Guidi, M.Marcelli, C. *J. Phys. Chem. B* **2006**, *110*, 10837.

39.   Xomeritakis, G.;Braunbarth, C. M.;Smarsly, B.;Liu, N.;Kohn, R.;Klipowicz, Z.Brinker, C. J. *Micropor. Mesopor. Mater.* **2003**, *66*, 91.

40.   Nishiyama, N. P., D. H.; Koide, A.; Egashira, Y.; Ueyama, K.; . *J. Membr. Sci.* **2001**, *182*, 235–244.

41.   Yamaguchi, A.;Uejo, F.;Yoda, T.;Uchida, T.;Tanamura, Y.;Yamashita, T.Teramae, N. *Nature Materials* **2004**, *3*, 337.

42.   Lu, Q.;Gao, F.;Komarneni, S.Mallouk, T. E. *Journal of the American Chemical Society* **2004**, *126*, 8650.

43.   Wu, Y.;Cheng, G.;Katsov, K.;Sides, S. W.;Wang, J.;Tang, J.;Fredrickson, G. H.;Moskovits, M.Stucky, G. D. *Nat. Mater.* **2004**, *3*, 816.

44.   Platschek, B.;Petkov, N.Bein, T. *Angewandte Chemie-International Edition* **2006**, *45*, 1134.

45.   Huang, E.;Rockford, L.;Tussell, T. P.Hawker, C. J. *Nature* **1998**, *395*, 757.

46.   Thurn-Albrecht, T.;Steiner, R.;DeRouchey, J.;Stafford, C. M.;Huang, E.;Bal, M.;Tuominen, M.;Hawker, C. J.Russell, T. P. *Adv. Mater.* **2000**, *12*, 787.

47.   Huang, E.;Russell, T. P.;Harrison, C.;Chaikin, P. M.;Register, R. A.;Hawker, C. J.Mays, J. *Macromolecules* **1998**, *31*, 7641.

48.   Jeong, U.;Ryu, D. Y.;Kho, D. H.;Kim, J. K.;Goldbach, J. T.;Kim, D. H.Russell, T. P. *Advanced Materials (Weinheim, Germany)* **2004**, *16*, 533.

49.   Hillhouse, H. W.;van Egmond, J. W.;Tsapatsis, M.;Hanson, J. C.Larese, J. Z. *Micropor. Mesopor. Mater.* **2001**, *44*, 639.

50.   Koganti, V. R.Rankin, S. E. *J. Phys. Chem. B.* **2005**, *109*, 3279.

51.   Hyeok, C. E., S.; Dionysios, D, D. *Appl. Catal., B* **2006**, *63*, 60.

52.   Perez, L. C. K., L.; Peng, B.; Thelakkat, M. . *J. Phys. Chem. B.* **2006**, *110*, 8723.

53.   Bearzotti, A. B., J. M.; Innocenzi, P.; Falcaro, P.; Traversa, E. . *Sens. Actuators. B* **2003**, *95*, 107–110.

54.   Dimitrios, B., J. C. . *PCT Int. Appl.* **2005, 49 pp.**

55.   Takeo, Y. H., Z.; Hidekazu, U.; Itaru, H.; Teruaki, K. . *J. Phys. Chem. B.* **2004** *108*, 13341.

56.   Liu, N.;Chen, Z.;Dunphy, D. R.;Jiang, Y.-B.;Assink, R. A.Brinker, C. J. *Angew. Chem., Int. Ed.* **2003**, *42*, 1731.

57.   Hogarth, W. H. J. D. d. C., J. C.; Drennanb, J.; Lu, G. Q. . *J. Mater. Chem.* **2005**, *15*, 754–758.

58.   Kresge, C. T. L., M. E.; Roth, W. J.; Vartuli, J. C.; Beck, J. S. *Nature* **1992**, *359*, 710.

59. Beck, J. S. V., J. C.; Roth, W. J.; Leonowicz, M. E.; Kresge, C. T.; Schmitt, K. T.; Chu, C. T.-W.; Olson, D. H.; Sheppard, E. W.; McCullen, S. B.; Higggins, J. B.; Schlenker, J. L. *J. Am. Chem. Soc.* **1992**, *114*, 10834.
60. Nishiyama, N. P., D. H.; Koide, A.; Egashira, Y.; Ueyama, K. *Journal of Membrane Science* **2001**, *182*, 235.
61. Feng, X. F., G. E.; Wang, L. Q.; Kim, A. Y.; Liu, J.; Kemner, K. M. *Science* **1997**, *276*, 923.
62. Hayward, R. C. A.-H., P.; Chmelka, B. F.; Stucky, G. D. *Microporous and Mesoporous Materials* **2001**, *44*, 619.
63. Braun, A. E. *Semiconductor International* **1999**, *56*, 25.
64. Lu, Y. G., R.; Drewien, C. A.; Anderson, M. T.; Brinker, C. J.; Gong, W.; Guo, Y.; Soyez, H.; Dunn, B.; Huang, M. H.; Zink, J. I. *Nature* **1997**, *389*, 364.
65. Ogawa, M. *Supramolecular Science* **1998**, *5*, 247.
66. Li, X. S. F., G. E.; Birnbaum, J. C.; Wang, C. *Langmuir* **2004**, *20*, 9095.
67. Hogarth, W. d. C., J.; Drennan, J.; Lu, G. *Journal of Materials Chemistry* **2005**, *15*, 754.
68. Tolbert, S. H. S., T. E.; Feng, J.; Hansma, P. K.; Stucky, G. D. *Chemistry of Materials* **1997**, *9*, 1962.
69. Blin, J. L. H., G.; Otjacques, C.; Su, B. *Studies in Surface Science and Catalysis* **2000**, *129*, 57.
70. Kaneda, M. T., T.; Carlsson, A.;Sakamoto, Y.; Ohsuna, T.; Terasaki, O. *Journal of Physical Chemistry B* **2002**, *106*, 1256.
71. Dai, S. S., Y.; Ju, Y.; Burleigh, M. C.; Lin, J. S.; Barnes, C. E.; Xue. Z. *Advanced Materials* **1999**, *11*, 1226.
72. Petkov, N. M., S.; Jean, B.; Metzger, T.; Bein, T.;. *Materials Science and Engineering* **2003**, *23*, 827.
73. Smarsly, B. G., G.; Assink, R.; Brinker, C. J. *Progress in Organic Coatings* **2003**, *47*, 393.
74. Grosso, D. B., F.; Albouy, P.; Amenitsch, H.; Balkenende, A. R.; Brunet-Bruneau, A.; Rivory, J. *Chemistry of Metrials* **2002**, *14*, 931.
75. Grosso, D. B., A. R.; Albouy, P. A.; Ayral, A.; Amentisch, H.; Babonneau, F. *Chemistry of Metrials* **2001**, *13*, 1848.
76. Cagnol, F. G., D.; Soler-Illia, G. J.; Crepaldi, E. L.; Babonneau, F.; Amenitsch, H.; Sanchez, C. *Journal of Materials Chemistry* **2003**, *13*, 61.
77. Tiemann, M. G., V.; Blum, R.; Babonneau, F.; Amenitsch, H.; Linden, M. *Langmuir*, *16*, 10053.
78. Alonso, B. B., R.; Albouy, P.; Durand, D.; Babonneau, F. *New J. Chem.* **2002**, *26*, 1270.
79. Grosso, D. B., F.; Sanchez, C.; Soler-Illia, G. J.; Crepaldi, E. L.; Albouy, P.; Amenitsch, H.; Balkenende, A. R.; Brunet-Bruneau A. *Journal of Sol-Gel Science and Technology* **2003**, *26*, 561.
80. Doshi, D. A. G., A.; Goletto, V.; Lu, M.; Gerung, H.; Ocko, B.; Han, S. M.; Brinker, C. J. *Journal of American Chemical Society* **2003**, *125*, 11646.
81. Koltz, M. A., P. A.; Ayral, A.; Menager, C.; Grosso, D.; Van der Lee, A.; Cabuil, V.; Babonneau, F.; Guizard, C. *Chemistry of Metrials* **2000**, *12*, 1721.
82. Brinker, C. J. *J. Non-Cryst. Solids* **1988**, *100*, 31.
83. West, J. K. Z., B. F.; CHENG, Y. C.; Larry L. Hench, L. L. *Jouunal of Non-Crystalline SOlids* **1990**, *121*, 51.
84. Wood, D. L. R., E. M. *Applied Spectroscopy* **1989**, *43*.
85. Matos, M. C. I., L. M.; Almeida, R. M. *Journal of Non-Crystalline Solids* **1992**, *147&148*, 232.
86. Yoshino, H., ; Kamiya, K.; Nasu, H. *Journal of Non-Crystalline Solids* **1990**, *126*, 68.

87. van Beek, J. J. S., D.; Jansen, J. B. H.; Schuiling, R. D. *Journal of Non-Crystalline Solids* **1991**, *134*, 14.

88. Assink, R. A.Kay, B. D. *Polymer Preprints (American Chemical Society, Division of Polymer Chemistry)* **1991**, *32*, 506.

89. Assink, R. A.Kay, B. D. *Annual Review of Materials Science* **1991**, *21*, 491.

90. Doughty, D. H.;Assink, R. A.Kay, B. D. *Advances in Chemistry Series* **1990**, *224*, 241.

91. Assink, R. A.Kay, B. D. *Materials Research Society Symposium Proceedings* **1988**, *121*, 25.

92. Kay, B. D.Assink, R. A. *Materials Research Society Symposium Proceedings* **1986**, *73*, 157.

93. Assink, R. A.Kay, B. D. *Materials Research Society Symposium Proceedings* **1984**, *32*, 301.

94. Pouxviel, J. C.Boilot, J. P. *Materials Research Society Symposium Proceedings* **1988**, *121*, 37.

95. Pouxviel, J. C.;Boilot, J. P.;Beloeil, J. C.Lallemand, J. Y. *Journal of Non-Crystalline Solids* **1987**, *89*, 345.

96. Rankin, S. E.McCormick, A. V. *Magnetic Resonance in Chemistry* **1999**, *37*, S27.

97. Sanchez, J.;Rankin, S. E.McCormick, A. V. *Industrial & Engineering Chemistry Research* **1996**, *35*, 117.

98. Sanchez, J.;Rankin, S. E.McCormick, A. V. *Industrial & Engineering Chemistry Research* **1995**, *34*, 4351.

99. Calabro, D. C. V., E. W.; Ryan, F. X. *Microporous Materials* **1996**, *7*, 243.

100. Holmes, S. M. Z., V. L.; Thursfield, A.; Plaisted, R. J.; Cundy, C. S.; Dwyer, J. *Journal of Chemical Scoiety., Faraday Transactions* **1998**, *94*, 2025.

101. Tejedor-Tejedor, M. I. P., L.; Anderson, M. A. *Chemistry of Metrials* **1998**, *10*, 3410.

102. Innocenzi, P. *Journal of Non-Crystalline Solids* **2003**, *316*, 309.

103. Primeau, N. V., C.; Langlet, M. *Thin Solid FIlms* **1997**, *310*, 47.

104. Parrill, T. M. *Journal of Materials Research* **1992**, *7*, 2230.

105. Muroya, M. *Colloids and Surfaces* **1999**, *157*, 147.

106. Innocenzi, P. F., P.; Grosso, D.; Babonneau, F.;. *Journal of Physical Chemistry B* **2003**, *107*, 4711.

107. Innocenzi, P. K., T. *J. Phys. Chem. B* **2006**, *110*, 10837.

108. Brinker, C. J.;Lu, Y.;Sellinger, A.Fan, H. *Advanced Materials (Weinheim, Germany)* **1999**, *11*, 579.

109. Fidalgo, A. I., L. M. . *Journal of Non-Crystalline Solids* **2004**, *347*, 128.

110. van der Vis, M. K., R.; Oskam.; Snoeck, T. *J. Mol. Struct.* **1992**, *274*, 47.

111. Mondragon, M. A. C., V. M.; Garcia, J. M.; Tellez, S. C. . *Vibrational Spectroscopy* **1995**, *9*, 293.

112. Allinger, N. L. R., M.; Lii,J. *J. Am. Chem. Soc.* **1900**, *112*, 8293.

113. Te´llez, L. R., J.; Rubio, F.; Morales, E.; Oteo, J. L. *Spectroscopy Letters* **2004**, *37*, 11.

114. Ryoo, R. K., C. H.; Kruk, M.; Antochshuk, V.; Jaroniec, M. . *J. Phys. Chem. B* **2000**, *104*, 11464.

115. Li, D. G., X.; Song, J.; Di, Y.; Zhang, D.; Ge, X.; Zhao, L.; Xiao, F. *Colloids Surf., A* **2006**, *272* 194–202.

116. Van Der Voort, P. B., M.; Vansant, E. F.; . *J. Phys. Chem. B* **2002** *106*, 9027.

117. Koganti, V. R. R., S. E. *J. Phys. Chem. B* **2005**, *109*, 3279.

118. Llenado, R. A.Jamieson, R. A. *Analytical Chemistry* **1981**, *53*, 174R.

119. Rosen, M. J. a. G., H. A. , *Systematic Analysis of Surface Active Agents*. 1972, New York: Wiley-Interscience.

120. Mittal, K. L., Ed., , *Solution Chemistry of Surfactants*. Vol. I and 11 1979, New York: Plenum Press,.

121. Jungerman, E., *Cationic Surfactants*. Surfactant Science Series. Vol. Vol. 4. 1970., New York: Marcel Dekker, Inc.
122. Kresge, C. T.;Leonowicz, M. E.;Roth, W. J.;Vartuli, J. C.Beck, J. S. *Nature (London, United Kingdom)* **1992**, *359*, 710.
123. Palmqvist, A. E. C. *Current Opinion in Colloid & Interface Science* **2003**, *8*, 145.
124. Zhao, X. S.;Lu, G. Q.Millar, G. J. *Industrial & Engineering Chemistry Research* **1996**, *35*, 2075.
125. Ciesla, U.Schuth, F. *Microporous and Mesoporous Materials* **1999**, *27*, 131.
126. Alberius, P. C. A.;Frindell, K. L.;Hayward, R. C.;Kramer, E. J.;Stucky, G. D.Chmelka, B. F. *Chem. Mater.* **2002**, *14*, 3284.
127. Attard, G. S.;Glyde, J. C.Goltner, C. G. *Nature* **1995**, *378*, 366.
128. Templin, M.;Franck, A.;DuChesne, A.;Leist, H.;Zhang, Y. M.;Ulrich, R.;Schadler, V.Wiesner, U. *Science* **1997**, *278*, 1795.
129. Lu, Y. F.;Fan, H. Y.;Stump, A.;Ward, T. L.;Rieker, T.Brinker, C. J. *Nature* **1999**, *398*, 223.
130. Ku, A. Y.;Taylor, S. T.Loureiro, S. M. *Journal of the American Chemical Society* **2005**, *127*, 6934.
131. Rajagopalan, R. *Current Opinion in Colloid & Interface Science* **2001**, *6*, 357.
132. Karaborni, S.Smit, B. *Current Opinion in Colloid & Interface Science* **1996**, *1*, 411.
133. Larson, R. G. *Journal of Chemical Physics* **1988**, *89*, 1642.
134. Larson, R. G. *Journal of Chemical Physics* **1989**, *91*, 2479.
135. Larson, R. G. *Journal of Chemical Physics* **1992**, *96*, 7904.
136. Larson, R. G. *Chemical Engineering Science* **1994**, *49*, 2833.
137. Larson, R. G. *Macromolecules* **1994**, *27*, 4198.
138. Larson, R. G. *Journal de Physique II* **1996**, *6*, 1441.
139. Larson, R. G. *Current Opinion in Colloid & Interface Science* **1997**, *2*, 361.
140. Larson, R. G. S., L. E. Davis, H. T. *Journal of Chemical Physics* **1985**, *83*, 2411.
141. Zaldivar, M.Larson, R. G. *Langmuir* **2003**, *19*, 10434.
142. Mackie, A. D.;O'Toole, E. M.;Hammer, D. A.Panagiotopoulos, A. Z. *Fluid Phase Equilibria* **1993**, *82*, 251.
143. Kim, S.-Y.;Panagiotopoulos, A. Z.Floriano, M. A. *Molecular Physics* **2002**, *100*, 2213.
144. Lisal, M.;Hall, C. K.;Gubbins, K. E.Panagiotopoulos, A. Z. *Journal of Chemical Physics* **2002**, *116*, 1171.
145. Arya, G.Panagiotopoulos, A. Z. *Physical Review E: Statistical, Nonlinear, and Soft Matter Physics* **2004**, *70*, 031501/1.
146. Firetto, V.;Floriano, M. A.Panagiotopoulos, A. Z. *Langmuir* **2006**, *22*, 6514.
147. Cheong, D. W.Panagiotopoulos, A. Z. *Langmuir* **2006**, *22*, 4076.
148. Rodriguez-Guadarrama, L. A.;Talsania, S. K.;Mohanty, K. K.Rajagopalan, R. *Langmuir* **1999**, *15*, 437.
149. Gharibi, H.;Behjatmanesh-Ardakani, R.;Hashemianzadeh, S. M.;Mousavi-Khoshdel, S. M.;Javadian, S.Sohrabi, B. *Theoretical Chemistry Accounts* **2006**, *115*, 1.
150. Siperstein, F. R.Gubbins, K. E. *Molecular Simulation* **2001**, *27*, 339.
151. Siperstein, F. R.Gubbins, K. E. *Langmuir* **2003**, *19*, 2049.
152. Al-Anber, Z. A.;Bonet i Avalos, J.;Floriano, M. A.Mackie, A. D. *Journal of Chemical Physics* **2003**, *118*, 3816.
153. Zapata, C. P.;Casanova, H.Restrepo, J. *Progress in Colloid & Polymer Science* **2004**, *128*, 146.
154. Wijmans, C. M.Linse, P. *Journal of Physical Chemistry* **1996**, *100*, 12583.
155. Desplat, J. C.Care, C. M. *Molecular Physics* **1996**, *87*, 441.
156. Zehl, T.;Wahab, M.;Moegel, H. J.Schiller, P. *Langmuir* **2006**, *22*, 2523.
157. Shida, C. S.Henriques, V. B. *Journal of Chemical Physics* **2001**, *115*, 8655.

158. Turesson, M.;Forsman, J.;Akesson, T.Jonsson, B. *Langmuir* **2004**, *20*, 5123.
159. Kikuchi, M.Binder, K. *Journal of Chemical Physics* **1994**, *101*, 3367.
160. Brown, G.Chakrabarti, A. *Journal of Chemical Physics* **1994**, *101*, 3310.
161. Pickett, G. T.Balazs, A. C. *Macromolecules* **1997**, *30*, 3097.
162. Matsen, M. W. *Journal of Chemical Physics* **1997**, *106*, 7781.
163. Huinink, H. P.;Brokken-Zijp, J. C. M.;van Dijk, M. A.Sevink, G. J. A. *Journal of Chemical Physics* **2000**, *112*, 2452.
164. Rankin, S. E.;Malanoski, A. P.Van Swol, F. *Materials Research Society Symposium Proceedings* **2001**, *636*, D1.2/1.
165. Metropolis, N.;Rosenbluth, A. W.;Rosenbluth, M. N.;Teller, A. H.Teller, E. *Journal of Chemical Physics* **1953**, *21*, 1087.
166. Rosenbluth, M. N.Rosenbluth, A. W. *Journal of Chemical Physics* **1955**, *23*, 356.
167. Kellogg, G. J.;Walton, D. G.;Mayes, A. M.;Lambooy, P.;Russell, T. P.;Gallagher, P. D.Satija, S. K. *Physical Review Letters* **1996**, *76*, 2503.
168. Pauwels, B.;Van Tendeloo, G.;Thoelen, C.;Van Rhijn, W.Jacobs, P. A. *Advanced Materials (Weinheim, Germany)* **2001**, *13*, 1317.
169. Nooney, R. I.;Thirunavukkarasu, D.;Chen, Y.;Josephs, R.Ostafin, A. E. *Chemistry of Materials* **2002**, *14*, 4721.
170. Lebedev, O. I.;Van Tendeloo, G.;Collart, O.;Cool, P.Vansant, E. F. *Solid State Sciences* **2004**, *6*, 489.
171. Tan, B.Rankin, S. E. *Journal of Physical Chemistry B* **2004**, *108*, 20122.
172. Ogawa, M. *Supramol. Sci.* **1998**, *5*, 247.
173. Pevzner, S. R., O.; Rozen, R. Y. *Current Opinion Colloid Interface Sci.* **2000**, *4*, 420.
174. Edler, K. J. R., S. J. *Int. Rev. Phys. Chem.* **2001**, *20*, 387.
175. Ryan, K. M. E., D.; Olin, H.; Morris, M. A.; Holmes, J. D. *J. Am. Chem. Soc.* **2003**, *125*, 6248.
176. Chik, H. X., J. M. *Mater. Sci. Eng. R* **2004**, *43*, 103.
177. Konno, M. S., M.; Sugawara, S.; Saito, S. *J. Membrane Sci.* **1987**, *37*, 193.
178. Masuda, H. F., K. *Science* **1995**, *268*, 1466.
179. Diggle, J. W. D., T. C., Goulding, C. W. *Chem. Rev.* **1969**, *69*, 365.
180. Xu, T. Z., G.; Metzger, R. M. *Nanolett.* **2002**, *2*, 37.
181. Brinker, C. J. L., Y. F.; Sellinger, A.; Fan, H. Y. *Adv. Mater.* **1999**, *11*., 579.
182. Xomeritakis, G. B., C. M.; Smarsly, B.; Liu, N.; Kohn, R.; Klipowicz, Z.; Brinker, C. J. *Micropor. Mesopor. Mater.* **2003**, *66*, 91.
183. Nishiyama, N. P., D. H.; Koide, A.; Egashira, Y.; Ueyama, K. *J. Membrane Sci.* **2001**, *182*, 235.
184. Hillhouse, H. W. O., T.; van Egmond, J. W.; Tsapatsis, M. *Chem. Mater.* **1997**, *9*, 1505.
185. Hillhouse, H. W. v. E., J. W.; Tsapatsis, M. *Langmuir* **1999**, *15*, 4544.
186. Miyata, H. K., K. *Chem. Mater.* **2000**, *12*, 49.
187. Hillhouse, H. W. v. E., J. W.; Tsapatsis, M.; Hanson, J. C.; Larese, J. Z. *Chem. Mater.* **2000**, *12*, 2888.
188. Klotz, M. A., P.-A.; Ayral, A.; Menager, C.; Grosso, D.; Van der Lee, A.; Cabuil, V.; Babonneau, F.; Guizard, C. *Chem. Mater.* **2000**, *12*, 1721.
189. Lu, Q. G., F.; Komarneni, S.; Mallouk, T. E. *J. Am. Chem. Soc.* **2004**, *126*, 8650.
190. Thurn-Albrecht, T. D., J.; Russell, T. P.; Jaeger, H. M. *Macromolecules* **2000**, *33*, 3250.
191. Elhadj, S. W., J. W.; Niu, V. S.; Saraf, R. F. *Appl. Phy. Lett.* **2003**, *82*, 871.
192. T. L. Morkved, T. L., ; M. Lu, M.; A. M. Urbas, A. M.; E. E. Ehrichs, E. E.; H. M. Jaeger, H. M.; P. Mansky, P.; T. P. Russell, T. P. *Science* **1996**, *273*, 931.
193. Park, C. D. R., C.; Lotz, B.; Fetters, L. J,; Thomas, E. L. Macromolec. *Chem. Phys.* **2003**, *204*, 1514.
194. Fukunaga, K. E., H.; Magerle, R.; Krausch, G. *Macromolecules* **2000**, *33*, 947.

195. Rockford, L. L., Y.; Mansky, P.; Russel, T. P.; Yoon, M. *Phys. Rev. Lett.* **1999**, *82*, 2602.
196. Rockford, L. M., S. G.; Russel, T. P. *Macromoelecules* **2000**, *34*, 1487.
197. Kim, S. O. S., H. H.; Stoykovich, H.; Ferie, N. J.; de Pablo, J. J.; Nealey, P. F. *Nature* **2003**, *424*, 411.
198. Li, Z. Q., S.; Rafailovich, M. H.; Sokolov, J.; Tolan, M.; Turner, M. S.; Wang, J.; Schwarz, S. A.; Lorenz, H.; Kotthaus, J. P. *Macromolecules* **1997**, *30*, 8410.
199. Turner, M. S. J., J. F. *Macromolecules* **1992**, *25*, 6681.
200. Fasolka, M. J. H., D. H.; Mayes, A. M.; Yoon, M.; Mochrie, S. J. *Phys. Rev. Lett.* **1997**, *79*, 3018.
201. E. Sivaniah, E. Y. h., Y.; M Iino, M.; T Hahimoto, T.; K. Fukunaga, K. *Macromolecules* **2003**, *36*, 5894.
202. Kikuchi, M. B., K. *J. Chem. Phys.* **1994**, *101*, 3367.
203. Brown, G. C., A. *J. Chem. Phys.* **1994**, *102*, 1440.
204. Pickett, G. T. B., A. C. *Macromolecules* **1997**, *30*, 3097.
205. Matsen, M. W. *J. Chem. Phys.* **1997**, *106*, 7781.
206. Huinink, H. P. B.-Z., J. C. M.; van Dijk, M. A.; Sevink, G. J. A. *J. Chem. Phys.* **2000**, *112*, 2452.
207. Rankin, S. E. M., A. P.; van Swol, F. B. *Mater. Res. Soc. Symp. Proc.* **2001**, *636*, 121.
208. Huang, E. R., L.; Russell, T. P.; Hawker, C. J. *Nature* **1998**, *395*, 757.
209. Huang, E. R., T. P.; Harrison, C.; Chaikin, P. M.; Register, R. A.; Hawker, C, J.; Mays, J. *Macromol.* **1998**, *31*, 7641.
210. Thurn-Albrecht, T. S., R.; DeRouchey, J.; Stafford, C. M.; Huang, E.; Bal, M.; Tuominen, M.; Hawker, C. J.; Russell, T. P. *Adv. Mater.* **2000**, *12*, 787.
211. Jeong, U. R., D. Y.; Kho, D. H.; Kim, J. K.; Goldbach, J. T.; Kim, D. H.; Russel, T. P. *Adv. Mater.* **2004**, *16*, 533.
212. Yang, H. C., N.; Sokolov, I.; Ozin, G. A. J. *Mater. Chem.* **1997**, *7*, 1285.
213. Pai, R. A. H., R.; Schulberg, M.T.; Sengupta, A.; Sun, J.N.; Watkins, J.J. *Science* **2004**, *303*, 507.
214. Cagnol, F. G., D.; Soler-Illia, G.J.A.A.; Crepaldi, E.L.; Babonneau, F.; Amenitsch, H.; Sanchez, C. *J. Mater. Chem.* **2003**, *13*, 61.
215. Zhao, D. Y., P.; Melosh, N.; Feng, J.; Chmelka, B. F.; Stucky, G. D. *Adv. Mater.* **1998**, *10*, 1380.
216. Hillhouse, H. W. E., J. W.; Tsapatsis, M.; Hanson, J. C.; Larese, J. Z. *Micropor. Mesopor. Mater.* **2001**, *44-45*, 639.
217. Koganti, V. R., Dunphy,D., Gowrishankar, V., McGehee,M. D., Li,X., Wang, J., Rankin,S.E. *Nano Letters* **2006** in press.
218. McCool, B. A.;Hill, N.;DiCarlo, J.DeSisto, W. J. *J. Membr. Sci.* **2003**, *218*, 55.
219. Zhang, J.-L.;Li, W.;Meng, X.-K.;Wang, L.Zhu, L. *J. Membr. Sci.* **2003**, *222*, 219.
220. Bearzotti, A. B., J. M.; Innocenzi, P.; Falcaro, P.; Traversa E. . *J. Euro. Cer. Soc.* **2004**, *24*, 1969.
221. Shioya, Y.;Ikeue, K.;Ogawa, M.Anpo, M. *Applied Catalysis a-General* **2003**, *254*, 251.
222. Guliants, V. V.;Carreon, M. A.Lin, Y. S. *J. Membr. Sci.* **2004**, *235*, 53.
223. Segalman, R. A. *Materials Science & Engineering R-Reports* **2005**, *48*, 191.
224. Chik, H. X., J. M. *Mater. Sci. Eng. R - Reports* **2004**, *43*, 103.
225. Freer, E. M.;Krupp, L. E.;Hinsberg, W. D.;Rice, P. M.;Hedrick, J. L.;Cha, J. N.;Miller, R. D.Kim, H. C. *Nano Letters* **2005**, *5*, 2014.
226. Melde, B. J.;Burkett, S. L.;Xu, T.;Goldbach, J. T.Russell, T. P. *Chemistry of Materials* **2005**, *17*, 4743.
227. Nishiyama, N.;Park, D. H.;Koide, A.;Egashira, Y.Ueyama, K. *J. Membr. Sci.* **2001**, *182*, 235.

228. Yoo, S. F., D.M.; Shantz, D.F. . *Langmuir* **2006**, *22*, 1839.
229. To a solution of 0.415 mM random copolymer in acetone was added a drop of glycerol to act as a cross-linker. An equimolar amount of 1, d. D.
230. Choi, S. Y. M., M. Coombs, N. Chopra, N. Ozin, G. A. *Advanced Functional Materials* **2004**, *14*, 335.
231. Kirsch, B. L.;Richman, E. K.;Riley, A. E.Tolbert, S. H. *J. Phys. Chem. B.* **2004**, *108*, 12698.
232. Hillhouse, H. W.;van Egmond, J. W.;Tsapatsis, M.;Hanson, J. C.Larese, J. Z. *Microporous and Mesoporous Materials* **2001**, *44-45*, 639.
233. Besson, S.;Gacoin, T.;Ricolleau, C.;Jacquiod, C.Boilot, J. P. *Journal of Materials Chemistry* **2003**, *13*, 404.
234. Smarsly, B.;Gibaud, A.;Ruland, W.;Sturmayr, D.Brinker, C. J. *Langmuir* **2005**, *21*, 3858.
235. The multilayer film was prepared by first depositing a layer of CaF2 by e-beam evaporation, f. b. S., onto this layer, the PEO-r-PPO layer was dip coated followed by the silica sol.
236. Jeong, H. K. C., R.; Chu, K.L.; Shannon, M.A.; Masel, R.I. . *Ind. Eng. Chem. Res.* **2005**, *44*, 8933.
237. Velev, O. D.;Jede, T. A.;Lobo, R. F.Lenhoff, A. M. *Nature (London)* **1997**, *389*, 447.
238. Velev, O. D.;Jede, T. A.;Lobo, R. F.Lenhoff, A. M. *Chem. Mater.* **1998**, *10*, 3597.
239. Konno, M.;Shindo, M.;Sugawara, S.Saito, S. *J. Membr. Sci.* **1988**, *37*, 193.
240. Masuda, H.Fukuda, K. *Science (Washington, D. C.)* **1995**, *268*, 1466.
241. Diggle, J. W.;Downie, T. C.Goulding, C. W. *Chem. Rev.* **1969**, *69*, 365.
242. Xu, T.;Zangari, G.Metzger, R. M. *Nano Lett.* **2002**, *2*, 37.
243. Beck, J. S.;Vartuli, J. C.;Roth, W. J.;Leonowicz, M. E.;Kresge, C. T.;Schmitt, K. D.;Chu, C. T. W.;Olson, D. H.;Sheppard, E. W.et al. *J. Am. Chem. Soc.* **1992**, *114*, 10834.
244. Edler, K. J.Roser, S. J. *International Reviews in Physical Chemistry* **2001**, *20*, 387.
245. Park, D.-H.;Nishiyama, N.;Egashira, Y.Ueyama, K. *Ind. Eng. Chem. Res* **2001**, *40*, 6105.
246. Park, D.-H.;Nishiyama, N.;Egashira, Y.Ueyama, K. *Microporous Mesoporous Mater.* **2003**, *66*, 69.
247. Chowdhury, S. R.;Schmuhl, R.;Keizer, K.;ten Elshof, J. E.Blank, D. H. A. *J. Membr. Sci.* **2003**, *225*, 177.
248. Boissiere, C.;Martines, M. A. U.;Kooyman, P. J.;de Kruijff, T. R.;Larbot, A.Prouzet, E. *Chem. Mater.* **2003**, *15*, 460.
249. Boissiere, C.;Martines, M. U.;Larbot, A.Prouzet, E. *J. Membr. Sci.* **2005**, *251*, 17.
250. Kang, T.;Oh, S.;Kim, H.Yi, J. *Langmuir* **2005**, *21*, 5859.
251. Platschek, B.;Petkov, N.Bein, T. *Angewandte Chemie, International Edition* **2006**, *45*, 1134.
252. Yang, H.;Coombs, N.;Sokolov, I.Ozin, G. A. *Nature (London)* **1996**, *381*, 589.
253. Liu, C.;Wang, J.Li, B. *J. Non-Cryst. Sol.* **2005**, *351*, 409.
254. Faget, L.;Berman, A.Regev, O. *Thin Solid Films* **2001**, *386*, 6.
255. Tolbert, S. H.;Schaeffer, T. E.;Feng, J.;Hansma, P. K.Stucky, G. D. *Chem. Mater.* **1997**, *9*, 1962.
256. Koganti, V. R. R., S. E. *Unpublished results*.
257. Oregan, B.Gratzel, M. *Nature* **1991**, *353*, 737.
258. Nazeeruddin, M. K.;Kay, A.;Rodicio, I.;Humphrybaker, R.;Muller, E.;Liska, P.;Vlachopoulos, N.Gratzel, M. *J. Am. Chem. Soc.* **1993**, *115*, 6382.
259. Hagfeldt, A.Graetzel, M. *Chemical Reviews (Washington, D. C.)* **1995**, *95*, 49.
260. Choi, H.;Stathatos, E.Dionysiou, D. D. *Applied Catalysis, B: Environmental* **2006**, *63*, 60.

261.	Coakley, K. M.;Liu, Y.;McGehee, M. D.;Frindell, K. L.Stucky, G. D. *Advanced Functional Materials* **2003**, *13*, 301.
262.	Cadby, A. J.Tolbert, S. H. *J. Phys. Chem. B.* **2005**, *109*, 17879.
263.	Zhao, L.;Yu, Y.;Song, L.;Hu, X.Larbot, A. *Appl. Surf. Sci.* **2005**, *239*, 285.
264.	Coakley, K. M.McGehee, M. D. *Appl. Phys. Lett.* **2003**, *83*, 3380.
265.	Kallala, M.;Sanchez, C.Cabane, B. *Physical Review E* **1993**, *48*, 3692.
266.	Courtecuisse, V. G.;Chhor, K.;Bocquet, J. F.Pommier, C. *Industrial & Engineering Chemistry Research* **1996**, *35*, 2539.
267.	Cristoni, S.;Armelao, L.;Gross, S.;Tondello, E.Traldi, P. *Rapid Commun. Mass Spectrom.* **2000**, *14*, 662.
268.	Kallala, M.;Jullien, R.Cabane, B. *Journal De Physique Ii* **1992**, *2*, 7.
269.	Choi, S. Y.;Mamak, M.;Coombs, N.;Chopra, N.Ozin, G. A. *Advanced Functional Materials* **2004**, *14*, 335.
270.	Haseloh, S.;Choi, S. Y.;Mamak, M.;Coombs, N.;Petrov, S.;Chopra, N.Ozin, G. A. *Chemical Communications (Cambridge, United Kingdom)* **2004**1460.
271.	Lee, U. H.;Lee, H.;Wen, S.;Mho, S.-i.Kwon, Y.-U. *Microporous and Mesoporous Materials* **2006**, *88*, 48.
272.	Liu, K.;Fu, H.;Shi, K.;Xiao, F.;Jing, L.Xin, B. *J. Phys. Chem. B.* **2005**, *109*, 18719.
273.	Li, X. S.;Fryxell, G. E.;Birnbaum, J. C.Wang, C. *Langmuir* **2004**, *20*, 9095.
274.	Crepaldi, E. L.;de Soler-Illia, G. J.;Grosso, D.;Cagnol, F.;Ribot, F.Sanchez, C. *J. Am. Chem. Soc.* **2003**, *125*, 9770.
275.	Jang, K.-S.;Song, M.-G.;Cho, S.-H.Kim, J.-D. *Chemical Communications (Cambridge, United Kingdom)* **2004**1514.
276.	Choi, S. Y.;Mamak, M.;Speakman, S.;Chopra, N.Ozin, G. A. *Small* **2005**, *1*, 226.
277.	Yu, J. C.;Wang, X.Fu, X. *Chem. Mater.* **2004**, *16*, 1523.
278.	Grosso, D.;Soler-Illia, G. J. d. A. A.;Crepaldi, E. L.;Cagnol, F.;Sinturel, C.;Bourgeois, A.;Brunet-Bruneau, A.;Amenitsch, H.;Albouy, P. A.Sanchez, C. *Chem. Mater.* **2003**, *15*, 4562.
279.	Coakley, K. M.;Liu, Y.;Goh, C.McGehee, M. D. *MRS Bulletin* **2005**, *30*, 37.
280.	Coakley, K. M.McGehee, M. D. *Chem. Mater.* **2004**, *16*, 4533.
281.	Attard, G. S.;Glyde, J. C.Goltner, C. G. *Nature (London)* **1995**, *378*, 366.
282.	Polarz, S.Antonietti, M. *Chemical communications (Cambridge, England) FIELD Publication Date:2002* 2593.
283.	Ciesla, U.Schuth, F. *Microporous and Mesoporous Materials* **1999**, *27*, 131.
284.	Lu, Y. G., R.; Drewien, C. A.; Anderson, M. T.; Brinker, C. J.; Gong, W.; Guo, Y.; Soyez, H.; Dunn, B.; Huang, M. H.; Zink, J. I. *Nature* **1997**, *389*, 364.
285.	Loy, D. A.Shea, K. J. *Chemical Reviews (Washington, D. C.)* **1995**, *95*, 1431.
286.	Freemantle, M. *Chem. Eng. News* **2000**, *24*, 33.
287.	Yokoi, T.;Yoshitake, H.Tatsumi, T. *Journal of Materials Chemistry* **2004**, *14*, 951.
288.	Inagaki, S.;Guan, S.;Fukushima, Y.;Ohsuna, T.Terasaki, O. *Journal of the American Chemical Society* **1999**, *121*, 9611.
289.	Sayari, A.;Hamoudi, S.;Yang, Y.;Moudrakovski, I. L.Ripmeester, J. R. *Chemistry of Materials* **2000**, *12*, 3857.
290.	Asefa, T.;MacLachlan, M. J.;Coombs, N.Ozin, G. A. *Nature (London)* **1999**, *402*, 867.
291.	Alberius, P. C. A.;Frindell, K. L.;Hayward, R. C.;Kramer, E. J.;Stucky, G. D.Chmelka, B. F. *Chemistry of Materials* **2002**, *14*, 3284.

Vita

Date of birth
12/30/1980

Place of birth
Hyderabad, India

Education
B.S.: Birla Institute of technology & Science, Pilani, India

Professional Positions
Project intern: January 2002 – July 2002, Indian Institute of Chemical Technology, Hyderabad, India

Professional Publications

Koganti, V. R., Dunphy, D., Gowrishankar, V., McGehee, M.D., Li, X., Wang, J., Rankin, S. E.,*"Generalized Coating Route to Silica and Titania Films with Orthogonally Tilted Cylindrical Nanopore Arrays"*, Nano Lett., in press

V. R. Koganti and S. E. Rankin, *"Synthesis of surfactant-templated silica films with orthogonally aligned hexagonal mesophase"*, *J. Phys. Chem B*, **2005**, 109, 3279-3283

Ch. Venkateswarlu and K. Venkat Rao, *"Dynamic recurrent radial basis function network model predictive control of unstable nonlinear processes", Chem. Eng. Sci.* **2005**, 60, 6718-6732

Sandhya M Vyas, Jaroslav Turánek, Pavlína Knötigová, Andrea Kašná, Veronika Kvardová, Venkat Koganti, Stephen E Rankin, Barbara L Knutson and Hans-Joachim Lehmler *"Synthesis and Biocompatibility Evaluation of Partially Fluorinated Pyridinium Bromides" New J. Chem.* **2006,** 30, 944 - 951

Venkat Rao Koganti
10/25/2006